공학박사학위논문

고분자 소재의 소성 변형 모사를 위한 데이터 기반 멀티스케일 해석

Data–driven Multiscale Framework for Elasto–Plastic Deformation Behavior of Glassy Polymers

2020 년 2 월

서울대학교 대학원

기계항공공학부

박 형 범

Abstract

In this dissertation, a data-driven multiscale framework has been established based on molecular dynamics (MD) simulations, finite element (FE) analysis, and a machine learning (ML) technique; this framework was aimed at elucidating the multi-axial elasto-plastic deformations of polymer materials. The proposed data-driven multiscale approach enables the construction of a macroscopic continuum model that has been customized for achieving unique deformation characteristics of the considered material, which are attributed to distinct microscopic structural features. In particular, the macroscopic continuum model is established based on the data-driven yield function, which is formulated by numerous multi-axial stress-strain behaviors that are systematically derived from MD simulations. Furthermore, to conduct multiscale analysis without any experimental support, certain methods have been developed to derive quasi-static stress-strains that overcome the timescale limitations of classical MD simulations. The main focus of this thesis is divided into three parts: qualitative analysis of microscopic deformation mechanisms of polymer materials, development of methods to overcome timescale limitations of MD simulations, and ML-based constitutive modeling through symbolic data mining.

With regard to the characterizations of microscopic deformation mechanisms, the nature of the inelastic-deformation characteristics of highly crosslinked epoxy polymers is examined at the microscopic level with respect to the differences in the structural network

topologies. It is examined by microscopic deformation simulations that the structural differences that arise from different types of curing agents (aliphatic and aromatic) cause the different irreversible folding behaviors of a local epoxy network.

Following the qualitative analysis on the deformation mechanisms, a calibration of the timescale difference between MD simulations and experiments is necessitated for achieving the quantitative analysis on plastic deformations; this is because the stress evaluated by MD simulations is not comparable to that of the experiments due to its extremely high strain rate. Two kinds of methods are developed to derive the quasi-static stress-strain profiles. The first approach is to use a 0 K solution of Argon theory to estimate internal stress and adopt the cooperative model to represent the nonlinear nature of yield stress on strain rate and temperature. The second approach is to predict the quasi-static yields by temperature accelerations by using time and temperature equivalence. A method to derive a hardening law under different strain rates is also established and demonstrated based on the yield stress-strain rate relation.

Based on deformation mechanisms and strain rate calibration methods, a multiscale framework is completed by developing a 3–dimensional constitutive model of the epoxy polymer from the data-driven yield function, which is formulated by a number of multi-axial yield data adopting a machine learning technique. The primary focus here is to confirm that the customized yield functions of various materials can be derived only from the yield data set without any prior knowledge on the primary stress invariants and functional structures; herein, the yield data set represents the unique multi-axial hardening

behavior. To validate the proposed method for yield function mining, the development history of the classical yield functions, such as von-Mises, Drucker-Prager, Tresca, Mohr-Coulomb, and paraboloidal yield functions are reproduced from the proposed approach simultaneously; this successfully characterizes the influence of the dispersion of the yield data set.

The proposed framework facilitates the understanding of intrinsic deformation features of polymer materials; further, it enables the construction of the data-driven plasticity model that is distinct from the conventional yield models. The proposed methodologies can be extended to a broad class of polymer materials by considering a variety of factors associated with nanoscale physics; in particular, the methods can address the problems that cannot be solved with the existing models or governing equations.

Keywords: Data–driven mechanics, Machine learning, Plastic deformations, Multiscale simulations, Nonlinear finite element analysis, Amorphous polymers.

Student Number: 2014-21563

Table of Contents

Table of Contents ..... **iv**

List of Figures ..... **viii**

List of Tables ..... **xv**

1. Introduction **1**

1.1. Necessity of a data–driven multiscale framework for the plasticity of polymers 1

1.2. Microscopic deformation mechanisms of amorphous polymers 3

1.3. Full–atomic molecular dynamics and timescale limitations 6

1.4. Classical yielding theories for polymer plasticity 9

1.5. Development of yield criterion for multi–axial deformations 11

1.6. Outline of the thesis 15

2. Atomistic model constructions and deformation simulations **18**

2.1. All-atom MD modeling and derivation of physical properties 18

2.2. Deformation simulations 24

2.2.1. Uniaxial deformation simulations 24

2.2.2. Uniaxial loading–unloading simulations 26

2.2.3. Cyclic deformation simulations 28

2.2.4. Multi–axial deformation simulations 30

3. Qualitative analysis on the elasto–plastic deformations of epoxy polymers 41

3.1. Influence of the molecular structure of curing agent on plastic deformations 41

3.1.1. Microscopic deformation mechanisms 41

3.1.2. Dihedral energy analysis 55

3.1.3. Strain-rate dependency of plastic dihedral-angle behaviors 59

3.2. Influence of the molecular structure of curing agent on ratcheting behaviors 61

3.2.1. Ratcheting behaviors and stiffness evolutions 61

3.2.2. Microscopic structural analysis 66

3.2.3. Relationship between epoxy structure and ratcheting behavior 70

3.3. Summary 74

4. Methods to overcome timescale limitations of classical molecular dynamics 98

4.1. Prediction of quasi–static constitutive laws by temperature–accelerated method .. 98

4.1.1. Theoretical background 98

4.1.2. Investigation on deformation characteristics and physical properties 100

4.1.3. Scheme for prediction of quasi–static solutions 104

4.2. Prediction of quasi–static constitutive laws by classical yielding theory 116

4.2.1. Prediction of quasi–static yields and construction of master curve 116

4.2.2. Effects of temperature, pressure, and crosslinking density 122

4.2.3. Construction of quasi–static constitutive laws 125

4.3. Summary 127

5. Classical yield function based constitutive modeling for multi-axial plastic deformations 143

5.1. Constitutive modeling based on paraboloidal yield function 143

5.2. Finite element analysis: one–element mesh validations 147

5.3. Finite element analysis: open–hole deformation tests 150

5.4. Summary 151

6. Machine learning based data–driven constitutive modeling for multi-axial plastic deformations 155

6.1. Reproduction of classical yield functions by symbolic regression 155

6.1.1. Symbolic regression 155

6.1.2. Symbolic data mining of classical yield functions 157

6.2. Development of data–driven yield function 163

6.2.1. MD characterizations on evolution of yield surface 163

6.2.2. Construction of data–driven yield function 166

6.2.3. Validation of the mined yield function 169

6.3. Constitutive modeling based on data–driven yield function 170

6.4. Finite element analysis: one–element mesh validations 173

6.5. Characteristics of data–driven yield function 174

6.6. Summary 179

7. Conclusions and recommendations..... 192

References 195

Abstract..... 207

List of Figures

Fig. 2.1. Molecular structures of the: (a) epoxy resin, (b) curing agent, and (c) constructed epoxy models. Upper and lower unit cells denote the diglycidyl ether of bisphenol A (DGEBA)/triethylenetetramine (TETA) and the DGEBA/diethyltoluenediamine (DETDA), respectively. 32

Fig. 2.2. Molecular structures of the (a) epoxy resin and curing agent. (b) A constructed atomistic model. 33

Fig. 2.3. A flowchart describing the simulation procedure of the dynamic crosslinking method. 33

Fig. 2.4. Illustration for the molecular structure of (a) the epoxy resin, (b) curing agent, and (c) constructed unit cell. 34

Fig. 2.5. A schematic of the uniaxial tensile simulation. Internal polymer chains are iteratively strained and relaxed using a multistep procedure. 34

Fig. 2.6. Illustration of (a) scheme for the deformation simulations with atomistic unit cells and (b) 2.5 % yield criterion. 35

Fig. 2.7. Scheme for deformation simulations in the molecular dynamics (MD) environment with illustrations of: (a) the uniaxial compressive loading–unloading simulations and (b) the crosslinked monomers of the epoxy resin and the curing agents. 36

Fig. 2.8. Illustration for (a) deformation tests with constructed atomistic model and (b) obtained representative stress–strain profiles. The 2.5% offset criterion for yield point from the multiaxial stress–strains is used for the yield point selection. The red solid line is

effective stress–strain and dotted lines are their components. The yield point is represented by triangle symbols. 37

Fig. 2.9. Illustration for (a) deformation tests with constructed atomistic model and (b) obtained representative stress–strain profiles. The 2.5% offset criterion for yield point from the multiaxial stress–strains is used for the yield point selection. The red solid line is effective stress–strain and dotted lines are their components. The yield point is represented by triangle symbols. 38

Fig. 3.1. Comparison of the radial distribution function (RDF) of groups of: (a) curing agents and (b) an epoxy resin. The RDF values were derived between all of the atomic pairs in the curing agents and the epoxy resin. 76

Fig. 3.2. Evolution of the internal-potential-energy components of two epoxy systems: (a) the diglycidyl ether of bisphenol A (DGEBA)/triethylenetetramine (TETA) and the DGEBA/diethyltoluenediamine (DETDA). The deformation energy is accommodated by nonbonded (red), bond (gray), angle (magenta), and dihedral (green) energies, and the blue lines denote their sum. The solid lines and the transparent dotted lines denote the responses to the loading and the unloading, respectively. The improper energy is omitted in the profiles owing to its small contribution. 77

Fig. 3.3. Comparison of the stress–strain responses of the triethylenetetramine (TETA) and diethyltoluenediamine (DETDA)-cured epoxy systems and the contributions of each internal parameter: (a), (b) nonbonded, (c) bond, (d) angle, and (e) dihedral-angle interactions. The red and blue solid lines denote the responses of the TETA- and DETDA-

cured epoxy systems, respectively. The solid lines and the short-dash lines denote the responses to the loading and the unloading, respectively. The stress-free state in (a) denotes the moment when the unit cell displayed a stress of zero during the unloading. All of the profiles are the averaged results over three different configurations, five different initial-velocity distributions, and three loading directions. 78

Fig. 3.4. (a) Constructed configurations of the curing-agent monomers of the considered crosslinked epoxy systems, (b) predicted dihedral-angle stress of the curing-agent monomers only, and (c) angle stress of the epoxy-resin monomers only. The error bars were obtained from the standard deviations (SDs) of the profiles of the different initial configurations. The dotted lines in (b) and (c) denote the unloading responses. The dihedral-angle and angle stresses of the curing-agent monomers were calculated by the division of each stress by the total unit-cell volume. 80

Fig. 3.5. Derived relative atomic mobility (RAM) evolutions with the applied strain in loading–unloading simulations: (a) the diglycidyl ether of bisphenol A (DGEBA)/triethylenetetramine (TETA) and (b) the DGEBA/diethyltoluenediamine (DETDA) systems. The RAM profiles for the atoms of the curing agents, the epoxy resin, and the inherent benzenes were calculated. In (a) and (b), *Cp* denotes the benzene atoms. (c) An illustration of the mobility characteristics of the considered curing agents. 82

Fig. 3.6. (a) Selected dihedral-angle types, which consist of the atoms of benzene, as well as the flexible chain segments that are linked to the benzene atoms, and their derived dihedral-energy profiles under (b) the diglycidyl ether of bisphenol A

(DGEBA)/triethylenetetramine (TETA) and (c) DGEBA/diethyltoluenediamine (DETDA) epoxy systems. *Type A* denotes the dihedral-angle type that is composed of two benzene atoms (represented as the force-field-type *cp*) and their linked oxygen (O) and carbon (C) atoms. *Type B* denotes the dihedral-angle type that is composed of two benzene atoms and their linked nitrogen (N) and C atoms. *Type A* belongs to the epoxy-resin monomers of both systems, and *Type B* belongs to the aromatic curing agent, DETDA. 83

Fig. 3.7. Predicted dihedral-energy evolutions of the diglycidyl ether of the bisphenol A (DGEBA)/triethylenetetramine (TETA) and (c) DGEBA/diethyltoluenediamine (DETDA) systems. The energy evolutions of the total dihedral angles and *Type A* in the DGEBA/TETA system are represented in (a) and (b), respectively. The energy evolutions of the total dihedral angles, *Type A*, and *Type B* are represented in (c), (d), and (e), respectively. In all of the profiles, the solid lines and the dotted lines denote the loading and unloading responses, respectively. 85

Fig. 3.8 (a) Illustration for the dihedral-angle energy states that correspond to the dihedral-angle variations of *Type A* and *Type B*. The representative dihedral-angle changes for *Type A* and *Type B* are shown in (b) and (c), which is just one case study of the dihedral-angle transitions of *Type A* and *Type B*. The variations of the numerical ratios of the plastic dihedral-angle transitions are shown in (d) and (e). The total of the dihedral angles of *Type A* is 600 and that of *Type B* is 484. 87

Fig. 3.9. Predicted total stress–strain profiles and contributions of the dihedral-angle stresses of only the curing agents at two different strain-rate conditions: (a) 10^9/s, (b) 10^8/s,

(c) 10^9/s, and (d) 10^8/s. The dotted lines in all of the profiles denote the unloading responses. All of the profiles have been averaged over different initial-velocity distributions (five times) and loading directions (x, y, and z axes). 89

Fig. 3.10. Comparison of the ratcheting behaviors of DGEBA/DETDA and DGEBA/TETA systems under compressive cyclic loading–unloading. Stress–strain profiles under loading direction with increasing cycles: (a) DGEBA/DETDA, (b) DGEBA/TETA. Corresponding evolutions of the ratcheting strain: (c) DGEBA/DETDA, (d) DGEBA/TETA. Visual illustration for the ratcheting strains of those two epoxies at 8.33 ns^{-1} is presented in (e), (f). Influence of the frequency condition was considered. The profiles at the high frequency (8.33 ns^{-1}) are represented by deep blue and green lines in (a), (b) and by solid line in (c), (d), while those at the low frequency (4.17 ns^{-1}) represented by light blue and green lines in (a), (b) and by dotted line in (c), (d). 91

Fig. 3.11. Comparisons of the stiffness components with the number of the cycles. Stiffness evolutions toward the loading direction: (a) DGEBA/DETDA, (b) DGEBA/TETA; stiffness evolutions perpendicular to the loading direction: (c) DGEBA/DETDA, (d) DGEBA/TETA; transverse shear stiffness evolutions: (e) DGEBA/DETDA, (f) DGEBA/TETA. The results at high frequency and low frequency are represented in all figures by red and blue symbols, respectively. 93

Fig. 3.12. Stress evolutions correlated by the dihedral angle behaviors. (a) Dihedral angle stress of whole epoxy system DGEBA/DETDA with the number of cycles, (b) dihedral angle stress of whole epoxy system DGEBA/TETA with the number of cycles, (c) partial

dihedral angle stress of curing agent monomers in DGEBA/DETDA with the number of cycles, and (d) partial dihedral angle stress of curing agent monomers in DGEBA/TETA with the number of cycles. 94

Fig. 3.13. Change of the orientation order parameters of considered epoxy systems at different frequency conditions: (a) DGEBA/DETDA (8.33 ns^{-1}), (b) DGEBA/TETA (8.33 ns^{-1}), (c) DGEBA/DETDA (4.17 ns^{-1}), and (d) DGEBA/TETA (4.17 ns^{-1}). (e) Illustration for representative conformation change of resin monomer in DGEBA/DETDA system. 95

Fig. 3.14. Change of radius of gyrations during the cyclic deformation simulations at (a) high frequency 8.33 ns^{-1} and (b) low frequency 4.17 ns^{-1}. Profiles of DGEBA/DETDA and DGEBA/TETA are denoted by hollow and filled symbols, respectively. 96

Fig. 3.15. Free volume evolutions of (a) DGEBA/DETDA and (b) DGEBA/TETA at different frequency conditions (8.33 ns^{-1}, 4.17 ns^{-1}). The free volumes measured by fully loaded and unloaded states are simultaneously represented at the evolutions of both epoxies. 97

Fig. 4.1. Eyring plots constructed at three different temperatures ($T_1 < T_2 < T_3$) and effects of the shift factors (reproduced from ref. [14]). 129

Fig. 4.2. Density-temperature relationship for the target epoxy system, which is used to obtain the glass transition temperature (intersection point)..... 129

Fig. 4.3. Stress-strain responses obtained at various temperatures (below the glass transition temperature) and strain rates. The temperature/strain rate relationship is observed. 130

Fig. 4.4. A criterion for the yield point obtained from the stress-strain response. The yield point is determined by fitting the scattered MD data. The linear elastoplastic model is composed of four degrees of freedom: Young's modulus, yield stress, yield strain and hardening exponent. 130

Fig. 4.5. Predicted (a) yield stress and (b) reduced yield stress at various strain rates and temperatures. The slopes of three points set in (b) are determined as 0.128 (300 K), 0.111 (350 K), 0.095 (400 K), and 0.064 (450 K)..... 131

Fig. 4.6. Variation of yield stress depending on the strain rate under 450 K. The yield stresses can be divided into three groups according to the slope change. 131

Fig. 4.7. Illustration of construction process of Eyring plot for the reference temperature (300 K). Reduced yield stresses under elevated temperatures ((a) 350 K, (b) 400 K, and (c), (d) 450 K) are shifted to a lower strain rate range based on the derived shifting factor ratio. At each shifting step, the prediction profile is updated iteratively to achieve the appropriate modification of prediction curve. The fitted equation for the final updated curve for each step are given in the figures..... 132

Fig. 4.8. Predicted yield stress (a) and corresponding ultimate stress (b) changes with variation of the strain rate. The obtained curves show good agreements with the magnitudes of the experimental yield stress (50.19 MPa) and ultimate stress (60 MPa), which are obtained from the quasi-static response (experimental test) of epoxy by applying the suggested yield criterion..... 133

Fig. 4.9. Comparison of prediction profiles between models of using full data points

(identical curve in Fig. 4.8(a)) and limited data points. 133

Fig. 4.10. A comparison of the predicted quasi-static (experimental low strain rate) stress-strain solution (blue solid line) with the experimental results. The inset depicts the exponentially fitted Young's modulus as a function of strain rate..... 134

Fig. 4.11. Determination of glass transition temperatures by the density–temperature profiles under three different crosslinking densities (75%, 80%, and 85%). 134

Fig. 4.12. Derived yield stress versus logarithm of the strain rate profiles under (a) compression and (b) tension considering different temperature (0 K, 100 K, 200 K, and 300 K). The yield data at each temperature is fitted by the cooperative model considering the quasi–static yield stress. 135

Fig. 4.13. Derived yield stress versus logarithm of the strain rate profiles under (a) compression and (b) tension considering different hydrostatic pressures (1 atm, 1000 atm, 3000 atm, and 5000 atm). The yield data under each pressure is fitted with the quasi–static yield stresses which were predicted by the internal stresses depending on the pressure coefficients. 136

Fig. 4.14. Derived yield stress versus logarithm of the strain rate profiles under (a) compression and (b) tension considering different crosslinking densities (75%, 80%, and 85%). The quasi–static yields were predicted respectively by the Argon theory and used for the constructions of the master curves (dashed lines). 136

Fig. 4.15. Illustration for (a) the scheme for the construction of the quasi−static post−yielding responses and applications to the (b) compression and (c) tension at 300 K, 1 atm.

The MD data was obtained from the 1–dimensional deformation tests of 80% crosslinked model and validated with experimental results[74,75]..... 137

Fig. 5.1. Comparison of the quasi–static constitutive equations and stress–strain profiles obtained from the 1–element simulations considering different temperature ((a) compression, (b) tension), hydrostatic pressure ((c) compression, (d) tension), and crosslinking density ((e) compression, (f) tension). The experimental results in (e) and (f) are taken from the works of Guest et al.[74] and Tsai et al.[75]..... 153

Fig. 5.2. Evolution of the yield surface in $\sigma_3 = 0$ plane which corresponds to the uniaxial hardening laws considering the influence of (a) temperature, (b) hydrostatic pressure, and (c) crosslinking ratio. The definition of the effective strain in work of Rottler et al.[67] is used for specification..... 154

Fig. 5.3. Applied displacement fields and corresponding equivalent plastic strain fields depending on the crosslinking ratios. (a) displacement field when the 85 % crosslinked model starts to deform plastically; (b) the equivalent plastic strain field (corresponding to the displacement field (a)); (c) displacement field when the 75 % crosslinked model reaches plateau state; (d) the equivalent plastic strain field (corresponding to the displacement field (c)). 154

Fig. 6.1. Reproduced classical yield functions by symbolic data mining under various artificial errors: (a) 0% arbitrary dispersion, von–Mises function, (b) 10% arbitrary dispersion, von–Mises function, (c) 0% arbitrary dispersion, Drucker–Prager function, (d) 20% arbitrary dispersion, Drucker–Prager function, (e) 0% arbitrary dispersion, Tresca

function, (f) 3% arbitrary dispersion, Tresca function, (g) 0% arbitrary dispersion, Mohr–Coulomb function, (h) 3% arbitrary dispersion, Mohr–Coulomb function, (i) 0% arbitrary dispersion, paraboloidal function, and (j) 30% arbitrary dispersion, paraboloidal function. The hollow data points in each figure denote the subject training data set and the black dots denote the response of the exact yield functions. The red solid line exhibits the responses of the mined models. 181

Fig. 6.2. Mined yield surfaces under severe error: (a) Drucker–Prager, 30% arbitrary dispersion, (b) Mohr–Coulomb, 20% arbitrary dispersion, and (c) paraboloidal, 40% arbitrary dispersion. 182

Fig. 6.3. Illustration for the construction of quasi-static yield surface from the MD yield surface: (a) yield surface evolution with increment of equivalent plastic strain under MD strain rate condition ($10^{8.5}$/s); (b) proposed scheme to construct a quasi-static yield surface from MD simulations; (c) normalized yield surfaces' evolution with different equivalent plastic strains; and (d) constructed quasi-static yield surfaces with increasing equivalent plastic strains. Note that the quasi-static stress–strain profiles of a previous study (Park et al.[104]) were used to reconstruct the surfaces. Comparison of (e) the yield surfaces under different strain rates ($10^{9.5}$/s and $10^{8.5}$/s), and (f) quasi-static yield surfaces obtained by proposed mapping method. 183

Fig. 6.4. Resulting candidate functions from symbolic regression. Each candidate yield function is shown in the complexity-fitness profile: (a) total and (b) filtered populations. For symbolic data mining, a total of 12,000 populations were randomly produced with

multiple runs for model diversity. The mathematical nodes considered in the present study are basic arithmetic symbols, including power..... 184

Fig. 6.5. Comparison of the data-driven yield function with the classical yield functions (Drucker–Prager and paraboloidal yield functions) and experimental result. The evaluated equivalent plastic strains are (a) 0, (b) 0.005, (c) 0.01, (d) 0.015, and (e) 0.03. The data-driven, Drucker–Prager, and paraboloidal yield functions are represented by solid, dotted, and dashed lines, respectively (a–g). Validation of the data-driven yield surface with experimental result of Haba et al.[100] with correlated equivalent plastic strain condition: (f) 0, (g) 0.01. 185

Fig. 6.6. Results of one-element deformation tests under various loading paths: (a) compression, tension, and shear, and (b) bi-compression. The one-dimensional hardening profiles extracted by Park et al.[104] were used for inputs including all other physical properties. The studied Young's modulus, Poisson's ratio, and plastic Poisson's ratio were 2930 MPa, 0.35, and 0.35, respectively..... 186

List of Tables

Table 2.1. Detailed Information of Epoxy-polymer Unit Cells at Room Temperature (RT). 39

Table 2.2. Comparison of mechanical properties of TGAP/DDS epoxy system with those given in experimental literature. 39

Table 2.3. Physical conditions for the considered epoxy unit cells. 40

Table 2.4. Comparison of the Mechanical Properties of the Epoxy Systems of the Diglycidyl Ether of Bisphenol A (DGEBA)/Triethylenetetramine (TETA) and the DGEBA/Diethyltoluenediamine (DETDA) Systems. 40

Table 4.1. Yield data under different temperature and strain rate conditions for deriving quasi-static yield stress. For the accurate prediction of quasi-static yield, more detailed strain rate conditions of 300 K and 450 K are examined. 138

Table 4.2. Derived yield data and quasi–static yield for the construction of the master yield profile considering the influence of temperature. Note that the Young's modulus is derived by the linear regression up to the strain of 1 %. 139

Table 4.3. Derived yield data and quasi–static yield for the construction of the master yield profile considering the influence of hydrostatic pressure. Note that the Young's modulus is derived by the linear regression up to the strain of 1 %. 141

Table 4.4. Derived yield data and quasi–static yields for the construction of the master yield profile considering different crosslinking densities. Note that the Young's modulus is

derived by the linear regression up to the strain of 1 %. 142

Table 6.1. Details of the symbolic data mining for the classical yield functions and the data-driven yield function. 187

Table 6.2. Mined models for von–Mises, Drucker–Prager, Tresca, Mohr–Coulomb, and paraboloidal yield functions by the symbolic regressions. 188

Table 6.3. Mined yield functions for the subject epoxy polymer and the classical yield functions. Model 1 was finally selected as the data-driven yield function. 189

Table 6.4. Algorithm for the implementation of the constitutive model with the data–driven yield function 190

1. Introduction

1.1. Necessity of a data–driven multiscale framework for the plasticity of polymers

For a thorough description of plastic behaviors of polymer-based materials, an understanding of the microscopic mechanisms involved in elasto-plastic deformation regimes is of primary importance. This is because various nanophenomena and microscopic conditions, which determine the deformation characteristics of a material, significantly influence those mechanisms. In particular, post–yielding behaviors such as strain softening and hardening within the constitutive responses of the polymers need to be understood, with the consideration of chain dynamics that are associated with the topology of the microstructure.

In this context, MD simulations play a critical role in evaluating the effects of such diverse microscopic conditions and physical environments with direct observations of the molecular deformation behaviors. However, derivations of the plastic responses by full–atomic MD simulations are exceptionally challenging, which are quantitatively matched to an experimental scale. This is because the timescale discrepancy between the full–atomic MD simulations and experiments is enormous, which inevitably leads to a considerable stress gap between the stress-strain profiles of MD and experiments; this hinders the direct transfer of the constitutive equations of a material to macroscopic continuum models.

Accordingly, a reliable methodology to evaluate the quasi-static constitutive equations is a key issue in the multiscale modeling for the polymer plasticity, which can simultaneously overcome the timescale limitations of MD simulations. Further, the methodology aimed at calibrating the influence of the timescale limitations of MD enables the generation of a sufficient data set for multi-axial plastic deformations by characterizing the evolution of the yield surface in a 3–dimensional stress space. This implies a possibility for the development of the plasticity model using a machine learning (ML) technique.

From the perspective of mechanics, the development of a data-driven constitutive model is paramount; this can be achieved using the yield data derived from the discussed timescale calibration method. However, it cannot be guaranteed that a few classical yield functions perfectly describe the actual multi-axial yield behavior of the considered materials; these functions are based on one-dimensional yield stress functions derived by uniaxial deformation tests. Multi-axial yield behaviors are inevitably influenced by complicated circumstances such as types of materials, the deformation-testing environments, and microstructures determined by preprocesses.

Furthermore, additional estimations of the subsequent yield surfaces are also critical for the exact characterization of the yield surface evolution; this is because it is not guaranteed that the classical yield function in consideration will adequately describe the entire post-yielding behavior, even if the initial yield surface is matched well. Accordingly, the general yield functions could be inappropriate for the subject materials; this depends on their unique hardening behaviors or physical conditions, even if the yield function has

already been verified under other conditions within the same class of materials. Therefore, the ideal method of constitutive modeling constitutes two functions, namely: 1) to examine the overall evolution of multi-axial stress states of the subject material under the given physical conditions, and 2) to formulate a customized yield function from the derived data set by the one-to-one correlation between the yield function and the deformation properties of the material.

Accordingly, in this dissertation, the focus is placed on three subjects, namely: the characterization of the microscopic deformation mechanisms of epoxy, the development of a timescale calibration method, and data–driven constitutive modeling through data learning by symbolic regressions. This multiscale framework aims to encompass the qualitative characterizations of microscopic mechanisms and quantitative estimations of multi-axial plastic deformations of polymers through timescale calibration and an ML technique, without the need of any experimental characterizations of the deformation properties.

1.2. Microscopic deformation mechanisms of amorphous polymers

Amorphous polymer materials have been widely used for engineering purposes owing to their excellent multifunctional properties. Physical properties of amorphous

polymers are mainly determined by the types of constituents and their microstructure, which can be artificially controlled depending on the purpose. Generally, the critical factors of polymer architecture that primarily govern the physical properties are the monomer arrangement, chain length, and the corresponding morphology of polymer chains. Accordingly, numerous efforts to understand the structure-property relationship have been conducted by identifying the characteristics of the microscopic chain structure and evaluating the corresponding performances[1–12].

In particular, epoxy polymers, a class of thermoset polymers, have been used in various industrial fields such as aerospace, aircraft, automotive, energy, and electronics owing to their excellent thermomechanical properties and tunability of performance. Their excellent physical properties are attributed to the three-dimensional (3D) crosslinked internal networks that are constructed by the chemical reactions between the epoxy resin and the curing agent. The highly-crosslinked epoxy polymers exhibit more rigid molecular responses compared with the thermoplastic polymers, as the crosslinked sites in the epoxy polymers hinder any slippage occurrences between the internal polymer chains[1]. This inherent stiffness of the internal networks contributes to the high thermomechanical properties of epoxy polymers. The performances of epoxy polymers can be tailored using several degrees of freedom that influence the network morphology, such as the chemical compositions of the epoxy resin and the curing agent, the curing kinetics, and the branching.

Understanding on the elasto–plastic behaviors of the amorphous polymer materials demands thorough characterization on the structure–property relationships under various

physical circumstances featured by temperature, strain rate, and hydrostatic pressure. The influence of these physical variables on the constitutive responses of polymers has been an important issues in the experiments[13–19] and simulations[20–23], since the yield and post–yield stresses are nonlinearly changed in general due to the relaxation nature of the polymer segments. It means that the dissipation of the applied stress during the deformation is determined by the intrinsic chain relaxations which are largely dependent on the time, temperature, and pressure. Focusing on the relaxation nature of the glassy polymers, the quantification of the structure–property relations ranging from the elastic to plastic regime has been conducted considering the influence of crosslinking ratio[2,6], molecular structure of the resins and curing agents[24,25], molecular weight[26], extent of chain interactions[27], and reinforcements[12,28,29].

Recently, systematic estimations of the yielding have been conducted by directly observing the atomic behaviors during the deformation with the aid of the atomistic simulations[20,21,23]. The direct observations of the polymer molecules also help better understanding on the deformation mechanisms especially for characterizing the origins of plastic deformations. Generally, the atomistic studies on the deformation mechanisms of amorphous polymer reveal that the interchain non–bonded interaction mainly accommodates the applied deformation by occupying the most of the deformation energy[24,26,27], leading to vigorous local molecular movements as the plastic deformation proceeds. As far as thermoplastic polymers are concerned, the deformations in elastic regime are accommodated by the non–bonded interactions are dominant increasing the

portion of free volume. Afterward, the torsional angle transitions are dominant factor for plastic deformations; the transition population of the dihedral angle from trans to gauche state is maximized in the vicinity of the yield point based on the increased space between the polymer segments[26,27]. Concerning thermosetting polymers, the MD simulations regarding the epoxy polymers[21] reproduced the molecular kinks under compression, characterizing the correlation between the sharp stress drop and irreversible folding of the epoxy network.

Although the nature of the plasticity of amorphous glassy polymers has been identified, a detailed understanding of thermoset systems and the contributions of their specific structures is limited. Therefore, one of the objective of this thesis is the attainment of a qualitative understanding of the elastoplastic-deformation mechanisms of thermoset epoxy polymers in consideration of the effects of different curing agents (aliphatic and aromatic) and with the aid of MD simulations. In particular, the irreversible deformation behaviors that are attributed to the different chemical structures of curing agents are thoroughly investigated, and the variations in the energy, stress, and geometric characteristics are provided.

1.3. Full–atomic molecular dynamics (MD) and timescale limitations

It is generally agreed that it is difficult to investigate the effects of individual design

variables related to nanoscale physics and the segmental motion of thermosetting polymers solely by using experiments that demand a tremendous amount of trials and errors. Moreover, limitations in the precise control of the conversion ratio, visualization of the network structure, measurement of free volume related to the aging and degradation, and inevitable measurement noise make it difficult to fully understand the designed epoxy. Therefore, computer simulation techniques have also aimed at designing high-performance epoxies. In particular, MD simulations are considered to be the most effective and efficient way of probing the internal molecular structure and predicting the physical properties of thermoset polymers. Several groups have proposed specific modeling procedures to describe the real structural characteristics of bulk thermosetting polymers and have estimated their thermo-mechanical properties[6,10,30,31]. For instance, Kim et al. observed the effect of the crosslink density on thermo-mechanical properties such as the density, elastic modulus, and coefficient of thermal expansion with respect to different crosslinking methods from the point of view of modeling[6]. Li et al. observed the evolution of the molecular structures of two thermosetting epoxy systems with different degrees of cure; they then derived various thermo-mechanical properties, including the yield and glass transition temperature[31]. Moreover, MD simulation studies on epoxy have been a part of the constitutive modeling of composites, especially for the modeling of nanocomposites, which requires the elucidation of important nanoscale characteristics related to their interface or interphase features[11,32–38]. In this regard, various thermo-mechanical properties of epoxy have been predicted and used to establish constitutive models that are essential in

composite micromechanics theories.

Although MD simulations have been effectively used in establishing the fundamental background of the elasto-plastic deformation behavior of amorphous polymer materials, the temporal scale problem arising from extremely short time step, which stems from the computational limitations in the time integration of the equations of motions to obtain quasi-static mechanical response of polymers, remains a challenging issue. It has been generally agreed that in both experimental[13–15,17–19,39] and simulation studies[21,22,40,41], the yielding of an amorphous polymer is a rate-dependent phenomenon because of its viscoelastic nature; thus yield stress increases with the increasing strain rate. Therefore, owing to the huge time scale gap between the experimental and computational contexts, it is inevitable that notable differences will be observed in the evolution of deformation, which results in quantitative discrepancies of the stress-strain response.

In an efforts to overcome this timescale limitations, there is previous research to derive the quasi–static yield stress of the amorphous polymers using the atomistic simulations. The approach is to use the 0 K solution of the Argon theory considering that the Argon's solution is composed of the elastic properties of the materials[21,23]. Although the method has been successfully applied to the several polymer materials, it needs to be noted that the assumptions to derive the yield solution with respect to temperature deviates from the experimental observations. The previous studies used linear dependence to represent the yield stress–temperature relation, which remains unchanged with considered strain rate, while the experimental observations and classical yield models[13–19] reveal that the yield

stress nonlinearly varies with a changing temperature especially under low temperature.

To overcome the timescale limitations without violating the strain rate and temperature dependent physics of polymer yielding, two kinds of schemes have been developed in this thesis. The first approach is to use 0 K Argon solution as the previous study[21,23] proposed considering proper nonlinear dependence of yield stress on strain rate and temperature without any physically incorrect assumption; the second approach is temperature–accelerated scheme that uses time and temperature equivalence in predicting quasi–static yield stress as the experimental master curve is made. Based on the characterized quasi–static yields, the systematic predictions of quasi–static constitutive laws have been conducted considering strain rate dependence of hardening laws for the development of macroscopic constitutive model.

1.4. Classical yielding theories for polymer plasticity

In order to describe the nature of the polymer plasticity, the classical theories for the yielding of amorphous polymers have been developed with experimental validations[13–19,42–45]. As a first attempt, Eyring H. developed theory for the yielding of the glassy polymers by modeling an amount of energy required for the initiation of plastic flow based on the transition state theory[42]. The Eyring's theory describes the yielding of polymer as a single activation process, expressing linear dependence of the yield stress on the logarithm

of the strain rate. Afterward, Robertson[43] also established the correlation among the yield stress, strain rate, and temperature by assuming cis–trans molecular conformation transition mechanisms. Robertson's theory describe the yield stress with the glass transition temperature of the material by employing the Williams–Landel–Ferry (WLF) equation[46]. Another widely known model that represents the polymer plasticity is Argon's theory, which focuses on derivation of an activation free enthalpy of the thermally–activated production of molecular kinks[44,45]. The Argon's theory postulated the irreversible conformational change of the polymer chain with the doubly–kinked elastic cylinder by the introduction of the wedge disclination loop, which is adopted from the plastic deformation mechanism of the crystalline materials. The Argon theory describe the kinking activation energy for the yielding with the mechanical properties of the materials such as elastic modulus and Poisson's ratio. The subsequent yielding models such as Ree–Eyring model[47] and cooperative model[13–16,48,49] for the polymer plasticity have been developed by focusing on the accurate prediction of the yield stress under broad range of the strain rate and temperature. These models were developed based on the Eyring's equation assuming the involvement of the multiple relaxations in the plastic deformation of the glassy polymers to describe the nonlinear nature of the yielding under extremely high strain rate or low temperature where the local molecular movement is severely frozen. The additional activation processes contribute to the accurate estimation of the abrupt change of the yield stress under high strain rate range in the vicinity of the strain rate of about 10^3/s or temperature of about -50℃[13–19].

1.5. Development of yield criterion for multi–axial deformations

Yield functions of materials have been developed usually based on the experimental observations to represent the stress states in 3–dimensional principal stress space at which the materials start to plastically deform. The various yield functions have been developed to consider own complicated yielding behaviors for broad class of materials including ductile metal, concrete, soil, ceramic, polymers, and etc[50–55]. The basic plasticity theory generally assumes several aspects; only the deviatoric component of the stress is involved in the plastic deformations of materials while the hydrostatic component of the stress is ignored; the compressive and tensile yield stresses are considered equal each other; the volume of the materials is preserved during the plastic deformations. The von–Mises yield criterion that represents these aspects well was defined follows:

$$\sqrt{3J_2} = \sigma_y, \tag{1.1}$$

where σ_y is yield stress of material, and $J_2 = \frac{1}{2}\boldsymbol{S}:\boldsymbol{S}$ is the second invariant of deviatoric stress tensor, $\boldsymbol{S}$. The plastic deformation of the material start after the distortion strain energy reaches critical value that is described by the square root of the second invariant of deviatoric stress tensor.

The von–Mises yield criterion fails to predict the yielding of pressure–dependent materials and consider the discrepancy between the compressive and tensile yield stresses. In order to consider these aspects, the pressure–modified von–Mises criterion[51], which is

also called as Drucker–Prager yield function, characterized by a conically shaped surface was developed by introducing the first stress invariant as:

$$\alpha I_1 + \sqrt{J_2} - k = 0, \tag{1.2}$$

where α is a material parameter, k is a constant related to the yield stress, and I_1 is first stress invariant which is the sum of the diagonal components of the stress tensor. Eq. (1.2) can be rewritten by the compressive and tensile yield stresses that characterized by 1–dimensional deformation tests as follows:

$$\sqrt{3J_2}\,(\sigma_c + \sigma_t) + I_1(\sigma_c - \sigma_t) - 2\sigma_c\sigma_t = 0, \tag{1.3}$$

where σ_c and σ_t are 1–dimensional compressive and tensile yield stresses of materials. Similarly, the pressure–modification is also carried out by introducing I_1 based on the maximum shear stress, which is called Mohr–Coulomb yield function, as follows:

$$|\tau| = \mathrm{c} - \sigma_n \tan\phi, \tag{4}$$

where c, ϕ are material constants that can be expressed by the compressive and tensile yield stresses and τ and σ_n are shear and normal stresses. Another yield criterion that can consider the pressure dependency of yielding is paraboloidal yield function developed by Tschoegl[52] using the linear combination of the hydrostatic stress and square of von–Mises stress as follows:

$$6J_2 + 2(\sigma_c - \sigma_t)I_1 - 2\sigma_c\sigma_t = 0. \tag{5}$$

Since the yield function is composed of the stress invariants J_2 and I_1, the magnitude of the deviatoric stress vector nonlinearly changes according to the variation of I_1. Thus, the paraboloidal yield function not only represents the pressure–dependency of the yielding

but also exhibits a smooth apex of the surface in stress space unlike to the Drucker–Prager yield function.

Although the constitutive modeling using these classical yield functions have been widely performed for the analysis on the macroscopic inelastic deformation of various engineering materials[56–60], it cannot be guaranteed that the multi–axial yielding of the considered material is perfectly described by a few yield functions that generally defined by uniaxial deformation tests. In fact, it is difficult to make a definite judgement on the suitability of the typical yield functions on universal use even within the identical material class. Considering the comparison of yield surfaces previously performed by Ghorbel[58], it seems that the classical yield functions may fail or succeed to predict the initial yield surface depending on the type of materials or considered physical conditions. It means that the general yield functions could be inappropriate for the considered materials depending on their unique hardening behaviors or physical conditions even if the yield function has already been verified within the same class of materials. This fundamental problem of distrust in the performance of the yield function could be resolved if the functional structure of yield function could be reformed or optimized case by case under the given condition.

It is significantly difficult, however, to formulate the customized yield function corresponding to the specific kinds of materials, which is owing to the absence of the sufficient yield data set. The sufficient yield data set under broad range of loading paths, hydrostatic pressure, or other physical variables is necessary for the development of suitable yield function, but it is extremely challenging by experiments, which stems from

the inefficient time consumptions and the failure of accurate measures of the multi–axial stress states during the plastic deformations. Furthermore, the additional estimations on the subsequent yield surfaces are also of primary importance for the exact characterization of yield surface since it is not guaranteed that the considered classical yield function properly describe the entire post–yielding behavior even if the initial yield surface is matched with the yield function well. In this situations, the simulational approaches[20,23,24,29,33,61–67] can play an important role making use of improved computing power not only for the derivation of sufficient constitutive responses of broad class of materials but also for the accurate characterizations of yielding features such as pressure–dependency. In particular, their ability to generate a number of intrinsic constitutive laws leads to the data–driven constitutive modeling only by using the unique features of the accumulated data[68–70].

In this thesis, the data–driven multiscale framework is proposed to model the constitutive law from the data–driven yield function by using MD simulations and symbolic regression, which is one of the ML technique. The main objective is to confirm that the constitutive model can be developed by the data–driven yield function that is formulated just from the intrinsic yield data set considering the unique yielding characteristics of target material. To identify the intrinsic yielding behaviors, a number of quasi–static yielding responses of multi–axial deformations are derived from MD simulations with the suggested strain rate calibration method. Then, a new yield function is automatically formulated from the calibrated yield data set by extracting primary elements with the aid of constrained symbolic regressions and implemented in finite

element analysis.

1.6. Outline of the thesis

The overall objective of this thesis is three-fold: the elucidation of elasto-plastic deformation mechanisms at the microscopic scale, development of a method to derive quasi-static constitutive responses under the MD environment, and construction of a multiscale framework for multi-axial plastic deformations of epoxy polymers with the aid of MD simulations, finite element (FE) analysis, and an ML technique. The proposed multiscale framework enables macroscopic FE simulations by considering unique plastic behaviors of polymer materials without conducting any experiments; this is particularly true for beyond a uniform yield criterion that might be inappropriate to describe the multi-axial deformation behaviors depending on considered material. From the viewpoint of data-driven mechanics, the macroscopic continuum model customized for the given polymer materials is established by generating numerous multi-axial constitutive responses from the timescale calibration method and by implementing an ML technique to formulate data-driven yield functions. The suggested framework demonstrates that the macroscopic simulations on multi-axial plastic deformations can be conducted by focusing on unique deformation characteristics of materials that thoroughly reveal the related diverse physics, solely by simulation approaches.

In **Chapter 2**, all the modeling techniques, schemes for deformation simulations,

and preliminaries are presented along with the considered physical environments. In **Chapter 3**, qualitative analysis of the microscopic deformation of polymer materials is carried out to completely understand the deformation characteristics of epoxies. The deformation mechanisms of highly crosslinked epoxy polymers are investigated using MD simulations with regard to curing agents with different structures. In particular, the correlation between characterized irreversible folding mechanisms occurring in proximity to the benzene ring and accumulations of the plastic strain is identified by cyclic loading-unloading simulations. Although the direct observations of plastic deformation mechanisms of epoxy polymers are performed in **Chapter 3**, these studies are just limited to qualitative analyses due to the timescale limitations of classical MD simulations. Accordingly, to avoid quantitative stress deviation arising from ultrahigh timestep of classical MD simulations, **Chapter 4** presents methodologies to provide reliable yield of the stress-strain master curve that ranges from MD strain rate to quasi-static rate. Further, the methodologies also allow the consideration of various thermos–mechanical state variables and chemical variables such as temperature, hydrostatic pressure, and crosslinking ratio. Subsequently after complete characterizations of their influences have been achieved, the mapping method for the constitutive law toward a low strain rate is established for achieving a suitable multiscale analysis quantitatively. Based on the quasi-static stress-strain profiles derived from **Chapter 4**, the constitutive model using the paraboloidal yield surface is implemented in order to evaluate multi-axial deformation behaviors of the epoxy polymer in **Chapter 5**. One–element mesh tests under various temperature, hydrostatic pressure, and crosslinking ratio are performed and compared with

the original quasi-static constitutive laws. Focusing on the influence of the epoxy network, the plastic deformation behaviors of the open-hole structure are estimated by examining the effect of crosslinking densities. Importantly, combined loading behaviors represented by the constitutive model implemented in **Chapter 4** are featured using the failure envelope, which is described by the classical yield function. The classical yield functions are generally determined by the one–dimensional hardening laws obtained from experiments or simulations; this implies that critical stress states in a principal stress space entirely depend on only the one–dimensional constitutive responses. However, this might be inappropriate for the deformation characteristics of the intrinsic material due to the unique description of the multi-axial hardening of the material by classical yield functions. Therefore, in **Chapter 6**, the data-driven constitutive model that can properly consider the intrinsic multi–axial deformation behaviors is developed; this is achieved with the aid of the timescale extension in **Chapter 4**, the constrained symbolic data mining, and an ML technique. In this chapter, the possibility of the use of symbolic data mining for the characterization of the yield function is examined by reproducing the history of the development of classical yield functions, even under severe noise of the stress state. Subsequently, the established constrained symbolic data mining is applied to the description of plastic deformation of epoxy polymer to formulate the optimized or even undisclosed phenomenological yield functions; this is achieved by using the yield data derived from the MD simulations. Further, the mined data-driven yield function is validated with one–element tests and compared with the classical yield functions.

2. Atomistic model constructions and deformation simulations

In this chapter, all of atomistic modeling process, methods for deformation simulations as well as relevant physical environments considered in this dissertation are presented in detail. Considering different modeling conditions according to the chapters, all of simulational details are provided sequentially corresponding to the individual chapter.

2.1. All-atom MD modeling and derivation of physical properties

To describe the molecular behaviors in an MD environment, a polymer-consistent force field (PCFF) was used in all of the modeling processes and simulations of this research. The PCFF has been successfully used in polymer-based material simulations[71,72], and the PCFF is composed of valence and nonbonded terms as can be seen in Eq. (2.1):

$$
\begin{aligned}
E_{total} = & \sum_{b}[k_2(b-b_0)^2 + k_3(b-b_0)^3 + k_4(b-b_0)^4] \\
& + \sum_{\theta}[H_2(\theta-\theta_0)^2 + H_3(\theta-\theta_0)^3 + H_4(\theta-\theta_0)^4] \\
& + \sum_{\phi}[V_1(1-\cos\phi) + V_2(1-\cos 2\phi) + V_3(1-\cos 3\phi)] \\
& + \sum_{\chi} K_{\chi}\chi^2 + \sum_{b,b'} F_{bb'}(b-b_0)(b'-b'_0) \\
& + \sum_{b,\theta} F_{b\theta}(b-b_0)(\theta-\theta_0) + \sum_{\theta,\theta'} F_{\theta,\theta'}(\theta-\theta_0)(\theta'-\theta'_0) \\
& + \sum_{b,\phi}(b-b_0)(V\cos\phi + V_2\cos 2\phi + V_3\cos 3\phi) \\
& + \sum_{\theta,\phi}(\theta-\theta_0)(V\cos\phi + V_2\cos 2\phi + V_3\cos 3\phi) \\
& + \sum_{b,\theta,\phi} F_{b\theta\phi}(b-b_0)(\theta-\theta_0)\cos\phi + \sum_{i,j}\frac{q_i q_j}{r_{ij}} \\
& + \sum_{i,j}\varepsilon_{i,j}\left[\frac{A_{ij}}{r_{ij}^9} - \frac{B_{ij}}{r_{ij}^6}\right] \qquad . \qquad (2.1)
\end{aligned}
$$

The valence term consists of the bond stretch, angle, dihedral angle, and improper changes with their coupled effects, while the nonbonded term is composed of van der Waals and coulomb interactions. In all chapters, the cutoff distance of the van der Waals interaction is 9.5 Å, while the electrostatic interaction was calculated using the Ewald summation. Concerning the software packages used in this thesis, the commercial software package Materials Studio vers. 5.5 and the parallel molecular-dynamics code the *Large Atomic Molecular Massively Parallel Simulation (LAMMPS)* were used in all modeling and simulations.

Concerning the atomistic modeling in **Chapter 3**, the considered epoxy systems are composed of the *diglycidyl ether of bisphenol A (DGEBA)* that served as an epoxy resin and the two different curing agents *triethylenetetramine (TETA)* and *diethyltoluenediamine (DETDA)*. The chemical structures of the epoxy resin and the curing agents are represented

in Figs. 2.1 (a) and 2.1 (b), respectively.

As the first step in the preparation of an epoxy unit cell, the monomers of the epoxy resin and the curing agents were randomly dispersed in a periodic boundary condition using an amorphous cell module that satisfies the stoichiometric ratio of 1:1 between the reactive atoms in the resin and the curing agents; that is, the monomer-number ratios of the epoxy resin and the curing agents are 3:1 and 2:1 for the DGEBA/TETA and the DGEBA/DETDA, respectively. The monomer-unit number in the epoxy resin is set to be equal for the two systems. The energy of each unit cell was minimized through the conjugate-gradient method. Then, prior to the crosslinking simulations, the unit cells were fully equilibrated using the canonical (*NVT*) isothermal-ensemble simulation at 500 K for 200 ps.

Then, crosslinking simulations were performed using the dynamic-crosslinking method[10]. In this method, the distance between the uncrosslinked reactant pairs is constantly monitored, and new covalent bonds are formed when the distances between the reactive-atom pairs are smaller than the predefined cutoff distance. Then, the unit cells were equilibrated using the NVT isothermal-ensemble simulations to minimize the excessive stresses that are owing to the formation of new covalent bonds. This procedure was iteratively performed up to the target crosslinking ratio. In this chapter, the crosslinking ratio of the epoxy unit cells was set to approximately 80 % for both systems. After the crosslinked structures were obtained, a high kinetic energy was applied on the crosslinked

epoxy unit cell to obtain more-optimized structures with the NVT-ensemble dynamics simulation that was performed at 500 K for 2.5 ns. Then, the crosslinked epoxy unit cells were fully relaxed using the NVT ensemble at 300 K, followed by the application of the isothermal isobaric (*NPT*)-ensemble dynamics simulation at 300 K and 1 atm for 3 ns.

Following the previously described modeling procedure, the preparation of three different initial configurations of each epoxy composition was completed. Further, the deformation simulations were respectively performed on the different initial configurations for the reproducibility of the results. Significantly, the effects of the initial structures on the deformation behaviors were examined to guarantee the generosity of the characterized inelastic-deformation nature. Herein, the monomer number and the crosslinking ratio are set to similar levels to eliminate any other effects. The final constructed DGEBA/TETA and DGEBA/DETDA models comprise the totals of 8750 and 9675 atoms, respectively. The detailed information of the epoxy unit cells is shown in Table 2.1.

In **Chapter 4.1**, an amorphous unit cell consisting of triglycidyl-amino-phenol (TGAP) as an epoxy resin and diamino-diphenylsulfone (DDS) as a curing agent was prepared using the Amorphous Cell module with a target density of 1.2 g/cm^3; periodic boundary conditions were imposed on the prepared unit cell in all three directions. The size of the unit cell was 44.68 Å, the epoxy model consisted of a total of 8,505 atoms. The details of the molecular structures and the constructed unit cell are presented in Fig. 2.2. Prior to the crosslinking procedure, epoxy resin and curing agent were dispersed

amorphously in a unit cell with a ratio of 4:3 in order to match the stoichiometric conditions determined by having an equal number of reactive sites in epoxy resin and curing agent. After the amorphous cell construction, the model was minimized through the conjugate gradient method and equilibrated through an *NVT* isothermal ensemble simulation at 500 K for 1 ns to guarantee sufficient chain relaxation and dispersion before the crosslinking procedure. Herein, the crosslinking procedure between the reactive atoms of the resin and the hardener was also conducted using a dynamic crosslinking method, which was originally introduced and applied by Heine et al.[73] and Varshney et al.[10] (see Fig. 2.3).

After the crosslinking simulation is complete, the unit cell is equilibrated for a prolonged time through the *NVT* and *NPT* ensemble dynamics routines of LAMMPS. In order to achieve a more locally relaxed structure via supplying high thermal energy, an *NVT* ensemble simulation is performed for 1 ns at 500 K prior to the relaxation at the target temperatures. Afterwards, the same simulation was conducted at each target temperature (300 K, 350 K, 400 K, and 450 K) for 7.5 ns followed by the *NPT* dynamics simulations at 1atm for 7.5 ns each. The detailed properties of chosen atomistic model is shown in Table. 2.2.

In **Chapter 4.2, 5,** and **6**, the atomistic models for the epoxy polymer consisting of *diglycidyl ether of bisphenol A (DGEBA)* as an epoxy resin and *Jeffamine D230* as a curing agent were constructed. The model construction of epoxy polymers was conducted in an efforts to describe the actual chemical reactions between the crosslinking sites of the resin and curing agent. The considered molecular structures of the monomers and the

constructed unit cell is shown in Fig. 2.4. For the construction of realistic epoxy network, two lengths of the monomers of the curing agent are considered to properly describe the given length condition of monomers as in the experiments[74,75]. The considered molecular structure is shown in Fig. 2.4(b).

The crosslinked epoxy network is gradually built from the randomly dispersed monomers of resin and curing agent in such a way that the close contacts between reactive atoms are connected by priority following the dynamical crosslinking concept[10]. Before the crosslinking, the energy of the dispersed monomers of the resin and curing agent were minimized by the conjugate gradient method and fully relaxed by the 500 K canonical *(NVT)* isothermal ensemble simulations during 300 ps. Then, the crosslinking simulations were performed until the model is fully crosslinked up to target ratio. The crosslinked unit cells were fully relaxed again under target temperature and pressure condition by the isothermal isobaric *(NPT)* ensemble simulations during 5 ns respectively. The physical conditions of the constructed models are shown in Table 2.3. The models, M1, M2, M3, M4 are used for the characterization of the influence of the temperature on the constitutive responses, the models, M4, M5, M6 are for the characterization of the influence of the crosslinking ratio, and the models, M4, M7, M8, M9 are for the characterization of the influence of applied hydrostatic pressure.

2.2 Deformation simulations

In this chapter, the detailed schemes for the deformation simulations are presented. Since the types of the deformations adopted in each chapter are slightly different each other, the specific deformation conditions are sequentially explained in following sections.

2.2.1 Uniaxial deformation simulations

In **Chapter 4.1**, to derive the mechanical responses of the amorphous epoxy polymer, uniaxial tensile simulations under different strain rates and temperatures were performed. The basic scheme of the uniaxial tensile simulation is presented in Fig. 2.5. Under the external pressure on the planes normal to the tensile direction, strain is imposed gradually on the unit cell structure. Then, polymer chains in the unit cell deform along the tensile direction under certain strain rate conditions. To equilibrate the internal structure during the deformation, an *NPT* ensemble simulation is performed at every strain increment to describe Poisson's ratio by allowing the polymer chains to naturally shrink along the transverse direction. In this chapter, a strain of up to 0.15 is imposed in order to observe the elasto-plastic response sufficiently over different temperatures and strain rates. The temperature was chosen below the glass transition temperature, from 300 K to 450 K with 50 K of interval; furthermore, various strain rates were examined for each temperature

range. To obtain the distinct stress-strain responses, the simulation results were averaged from 6 to 36 times of independent production runs along all directions under an isotropic assumption.

In **Chapter 4.2**, **5** and **6**, the deformation tests were conducted to derive the stress–strain profiles of the considered models that are represented in Table 2.3. The stress–strain responses are estimated with iterative strain increment and relaxation on the unit cell until the user–specified maximum strain is reached. The deformed unit cell is relaxed at given the pressure condition to consider the Poisson's effect by allowing natural shrinkage or stretching. The strain is applied up to 0.15 in each deformation test to sufficiently observe the elasto–plastic deformation response of the epoxy polymers under high strain rate. Since the deformation tests in MD environment involve severe fluctuations of the stress by the considered thermostat, the stress–strain profile from each simulation condition was derived by averaging the 30 profiles for $10^{9.5}$/s, 10^{9}/s and 15 profiles for $10^{8.5}$/s, 10^{8}/s. The scheme for the deformation test is shown in Fig. 2.6(a). In order to determine a yield point from the obtained stress–strain, the 2.5 % offset rule[76,77] was adopted to properly consider the nonlinearly changing stress trend of epoxy polymer by setting a highly relaxed stress state as yield point. The illustration for yield criterion is shown in Fig. 2.6(b). The stress slope to determine a yield point is set by the linear fitting of strain up to about 5 % to guarantee reasonable stiffness under high variability of stress which stems from the extremely high strain rate condition[78,79]. Accordingly, it needs to be noted that the identified yield point belongs to the relatively much more plastically deformed area, showing larger stress than

the initial flow stress where the material starts to plastically deform.

2.2.2 Uniaxial loading–unloading simulations

In **Chapter 3.1**, to derive the mechanical responses of the epoxy polymers, uniaxial loading (compression)–unloading tests were conducted in the LAMMPS environment. Fig. 2.7(a) shows the considered deformation trajectory with a snapshot of the epoxy model. The epoxy models were compressed up to a strain of 0.15, followed by an unloading to the initial zero strain under the considered temperature (300 K, 1 K), strain-rate (10^9/s and 10^8/s), and pressure (1 atm) conditions.

The deformation simulations were composed of iterative imposition and relaxation processes regarding the strain that are based on the NPT-ensemble simulations. In the MD simulations, the strain was artificially imposed on the unit cell along one direction, and this was followed by the deformation of the internal polymer networks toward the loading direction. The deformed networks denoted higher internal stresses upon the imposition of the strains. Thus, the NPT-ensemble simulations at 300 K and the atmospheric-pressure conditions along the transverse direction were performed for certain durations that correspond to the considered strain rate for the chain relaxation. From this iterative relaxation procedure, the natural relaxation of the deformed networks allowed for a consideration of the Poisson effect.

During the deformation simulations, the totals of the internal energy and virial stresses were obtained using the applied strain that could be divided into the contributions of the internal potential components, as follows:

$$\begin{aligned}\sigma_{virial} &= \frac{1}{V}\sum_{\alpha}\left[\frac{1}{2}\sum_{\beta=1}^{N}(R_I^{\beta}-R_I^{\alpha})\mathrm{F}_j^{\alpha\beta}-n_d k_B T^{\alpha}\right] \\ &= \sigma_{ke}+\sigma_{non-bonded}+\sigma_{bond}+\sigma_{angle}+\sigma_{dihedral}+\sigma_{improper}\end{aligned}, \quad (2.2)$$

$$E_{pe}=E_{bond}+E_{angle}+E_{dihedral}+E_{improper}+E_{non-bonded}\ , \quad (2.3)$$

where n_d, k_b, T, and V are the number of the degrees of freedom, the Boltzmann constant, the temperature, and the occupied volume, respectively. In Eqs. (2.2) and (2.3), $\sigma_{non-bonded}$ and $E_{non-bonded}$ indicate the contributions of the summation of the van der Waals and coulomb interactions on the totals of the virial stress and the potential energy, respectively. The primary internal-potential components can be identified by deriving the contribution of each internal component on the stress and energy behaviors. The focus of **Chapter 3.1** is the plastic-deformation mechanisms for which the evolutions of the energy and the stress during the loading and unloading simulations were observed. In particular, compared with the deformation mechanisms of thermoplastic polymers[26], the plastic dihedral-angle behaviors of epoxy polymers were rigorously investigated according to the previously described manner.

Simultaneously, the monomers of the epoxy resin and the curing agent were considered to understand the influences of the different curing-agent structures on the

deformation mechanisms. The monomer sets of the epoxy resin and the curing agents (the groups of the epoxy resin and the curing agents in the crosslinked epoxy system) were divided based on crosslinked nitrogen (N) atoms, as can be seen in Fig. 2.7 (b). The internal energy and stress evolutions of the monomer sets of the epoxy resin and the curing agents were derived. From the division scheme, the different deformation behaviors in the two curing-agent molecules and their effects on the epoxy-resin molecules could be independently investigated.

To validate the prepared MD models, a comparison of the density and mechanical moduli of the present study with those of the other literature references is given in Table 2.4. The obtained density showed a sound agreement with the values of the other experimental and theoretical studies. Young's modulus was obtained from the stress–strain profiles (linear fitting up to the strain of 0.05) of the MD simulations that are similar to those of the MD studies[9,25], but they are quite different from those of the experiments[80,81]. This has been attributed to the idealized MD-model structures that are without any microscopic defects or the inherent high-strain-rate conditions of MD simulations.

2.2.3 Cyclic deformation simulations

To understand the ratcheting behaviors in **Chapter 3.2**, compressive cyclic loading–unloading simulations were conducted by the stress controlled deformations.

Scheme for the deformations is presented in Fig. 2.8. For the determination of the applied stress, the uniaxial compressive deformations were performed up to the strain 0. 15 at the strain rate 10^9 /s (see Fig. 2.8(a)), and the yield stress of each epoxy was determined by fitting on linear elastic and Ludwik's hardening model which is represented by:

$$\sigma = \sigma_y + h(\varepsilon^p)^n, \tag{2.4}$$

where σ_y, h, ε_p, and n are yield stress, strength coefficient, plastic strain, and hardening exponent, respectively. Yield point was chosen as a point denoting that the deviation between the raw MD data and elasto–plastic model is minimized. Resultant yield points of DGEBA/DETDA and DGEBA/TETA are (0.068, 253.98 MPa) and (0.07, 264.26 MPa) respectively. Concerning the cyclic deformation simulations, as an initial loading, compressive loading is applied on the atomistic unit cell by maintaining 1 atm on surfaces of the unit cell, which the loading is not imposed on, to provide the Poisson's effect (see state A in Figs. 2.8(b) and 2.8(c)). Then, the model is compressed till the predefined stress condition is satisfied (see state B in Figs. 2.8(b) and 2.8(c)). After that, the atomistic unit cell is reversely loaded to eliminate the stress which corresponds to the state C in Fig. 2.8. The effect of the ratchet is involved by the strain deviation between the state A and C in Figs. 2.8(b) and 2.8(c). Note that the level of the applied stress is 90 % of the yield stresses that were determined in Fig. 2.8(a). Other than the stress level, the frequency of the cyclic deformations was also considered as main variable since the amorphous polymer displays viscoelastic nature in deformations. In particular, considering the timescale difference of the MD simulations compared to the experiments[20,21], the study on the effect of the

frequency is also of primary importance. In this study, the studied frequency level is 8.33 ns^{-1} and 4.17 ns^{-1}. Based on the abovementioned stress and frequency conditions, a total of 500 cycles was simulated by considered epoxy polymers (Note that the number of cycles of DGEBA/DETDA by the frequency of 4.17 ns^{-1} is 480).

To calculate the change of the stiffness according to the cyclic deformations, Parrinello–Rahman strain fluctuation method was adopted, which have been widely used for the calculation of the elastic properties of amorphous polymer systems. This method measures the stiffness tensor based on the strain fluctuation determined from the inherent resistance to shaking of the unit cell, which is represented by:

$$C_{ijkl} = \frac{k_b T}{\langle V \rangle} \left\langle \delta\varepsilon_{ij} \delta\varepsilon_{kl} \right\rangle^{-1}, \tag{2.5}$$

where $\delta\varepsilon$ denotes the strain variation and the bracket means ensemble average. To apply the strain variation, $N\sigma T$ ensemble simulation for 100 ps was conducted on target unit cell. For the characterization of the elastic modulus from the stiffness tensor, we assumed that the atomistic unit cell deformed by cyclic loading is orthotropic allowing the stiffness difference according to the principal axis. To reduce the inherent statistical uncertainty in determining the elastic modulus, the 5 different modulus results were evaluated for deriving mean values and standard deviations.

2.2.4 Multi–axial deformation simulations

In **Chapter 6**, the deformation simulations were conducted to estimate yielding behavior in multiaxial stress states. The illustration for the deformation simulations and their resultant stress–strain profile are shown in Fig. 2.9. The deformation simulations are performed by sequential iterative strain application and relaxation, simultaneously considering external pressure conditions by *NPT* ensemble dynamics to consider the Poisson's effect. Since the deformation is applied by multiaxial manner, the determination of general stress state at yielding demands adequate yield criterion. In **Chapter 6**, the yield point is obtained from the effective stress–strain by applying 2.5% offset rule which has been generally employed in the experimental field[76,77]. The effective stress and strain are defined as:

$$\sigma_{eff} = \frac{1}{3}\left((\sigma_1 - \sigma_2)^2 + (\sigma_2 - \sigma_3)^2 + (\sigma_3 - \sigma_1)^2\right)^{1/2},$$

$$\varepsilon_{eff} = \frac{1}{\sqrt{2}(1+\nu)}\left((\varepsilon_1 - \varepsilon_2)^2 + (\varepsilon_2 - \varepsilon_3)^2 + (\varepsilon_3 - \varepsilon_1)^2\right)^{1/2}, \quad (2.6)$$

where ν is Poisson's ratio. As an example, an effective stress–strain profile and each components are shown in Fig. 2.9(b). The initial stiffness of effective stress–strain determined by linear fitting up to a strain of about 5% is used to estimate a yield point. Based on the chosen yield point, the each component of yield stress is uniquely determined to build a yield surface as denoted by blue triangles in Fig. 2.9(b). The yield surfaces were constructed by trying to evaluate all of biaxial loading paths in $\sigma_3 = 0$ plane with the effective strain rates of $10^{9.5}$/s and $10^{8.5}$/s.

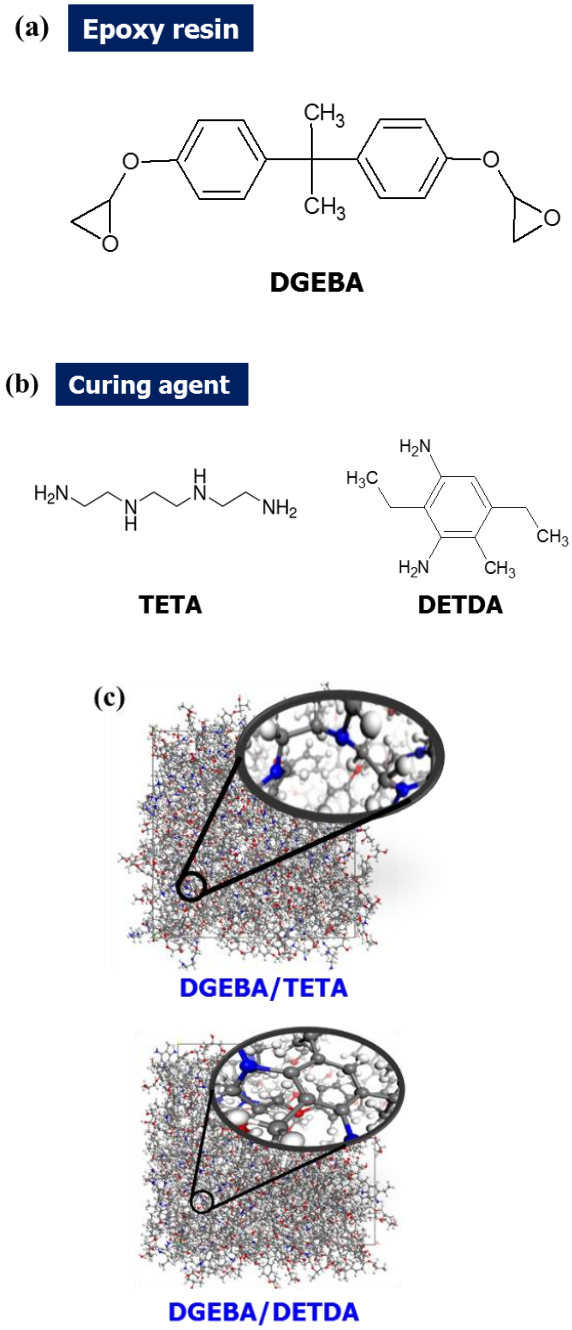

Fig. 2.1. Molecular structures of the: (a) epoxy resin, (b) curing agent, and (c) co nstructed epoxy models. Upper and lower unit cells denote the diglycidyl ether of bisphenol A (DGEBA)/triethylenetetramine (TETA) and the DGEBA/diethyltoluenedi amine (DETDA), respectively.

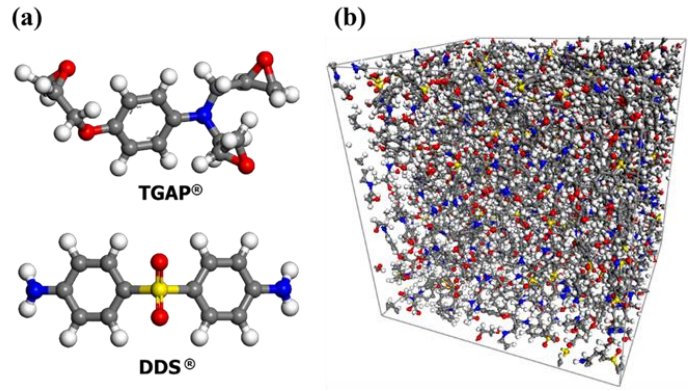

Fig. 2.2. Molecular structures of the (a) epoxy resin and curing agent. (b) A constructed atomistic model.

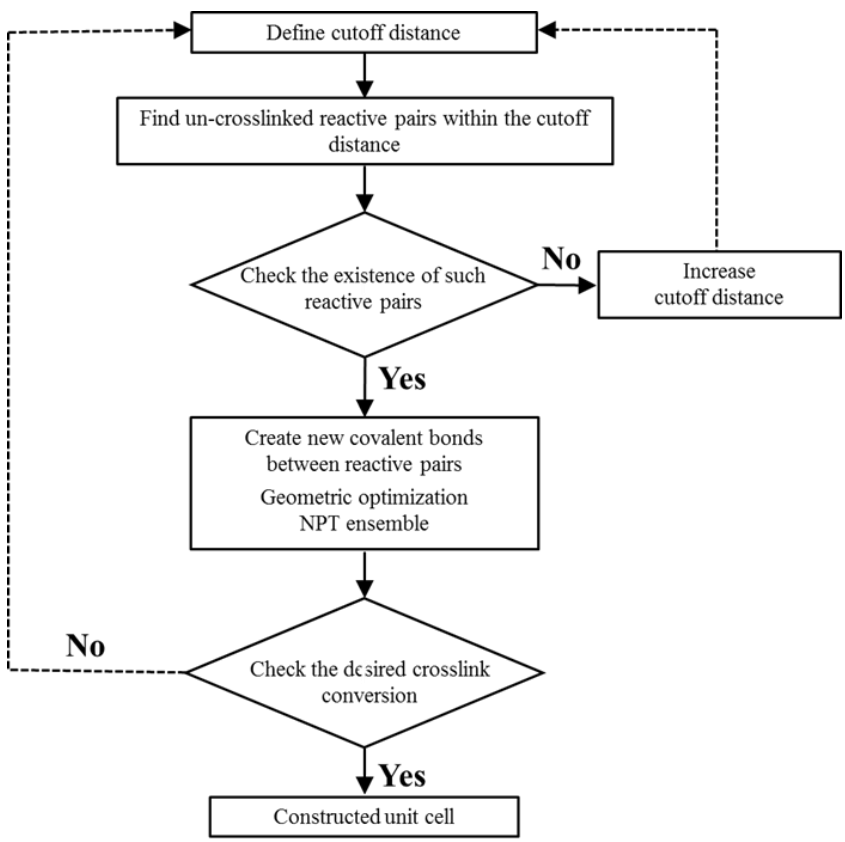

Fig. 2.3. A flowchart describing the simulation procedure of the dynamic crosslinking method.

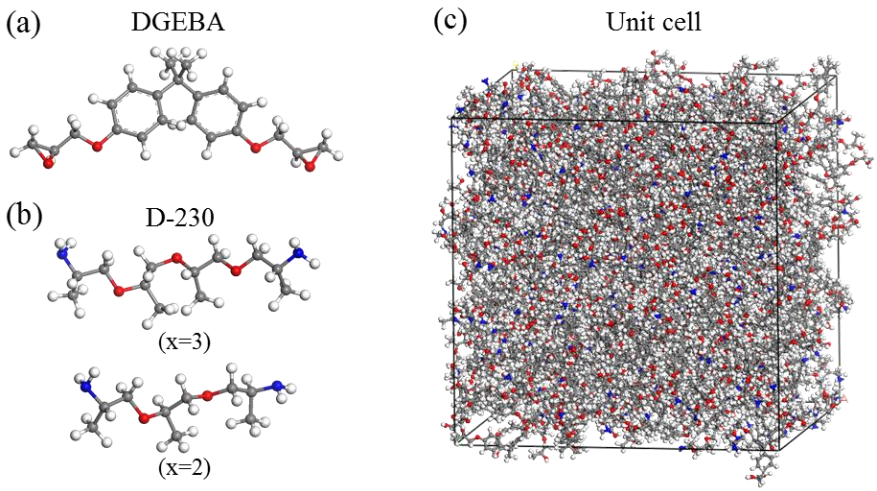

Fig. 2.4. Illustration for the molecular structure of (a) the epoxy resin, (b) curing agent, and (c) constructed unit cell.

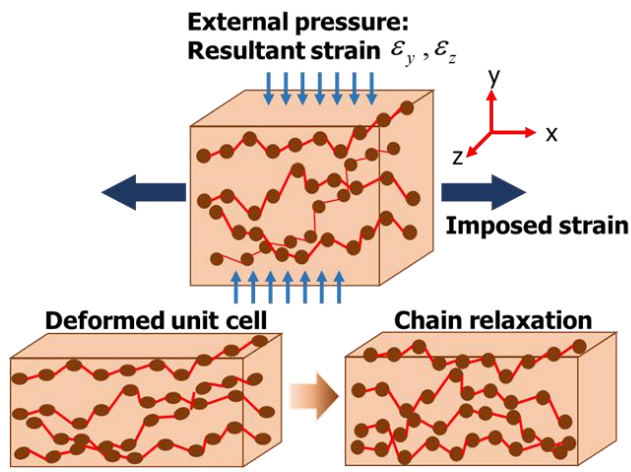

Fig. 2.5. A schematic of the uniaxial tensile simulation. Internal polymer chains are iteratively strained and relaxed using a multistep procedure.

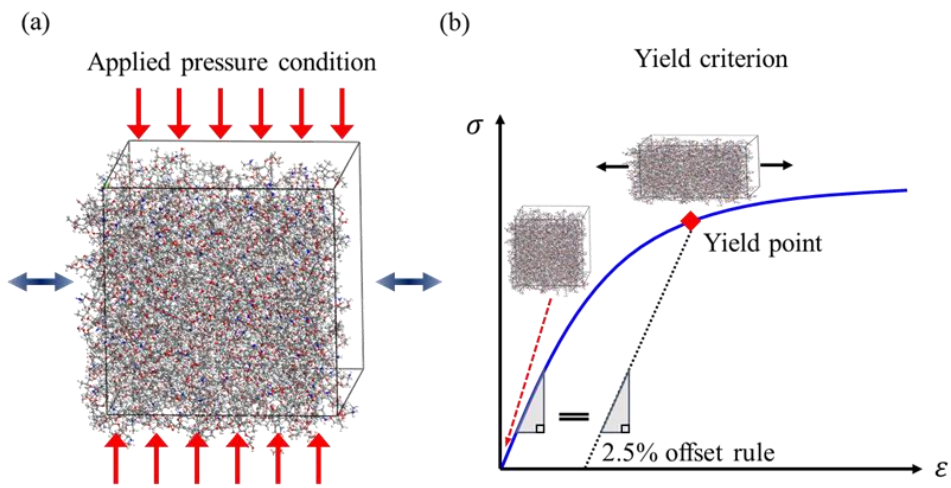

Fig. 2.6. Illustration of (a) scheme for the deformation simulations with atomistic unit cells and (b) 2.5 % yield criterion.

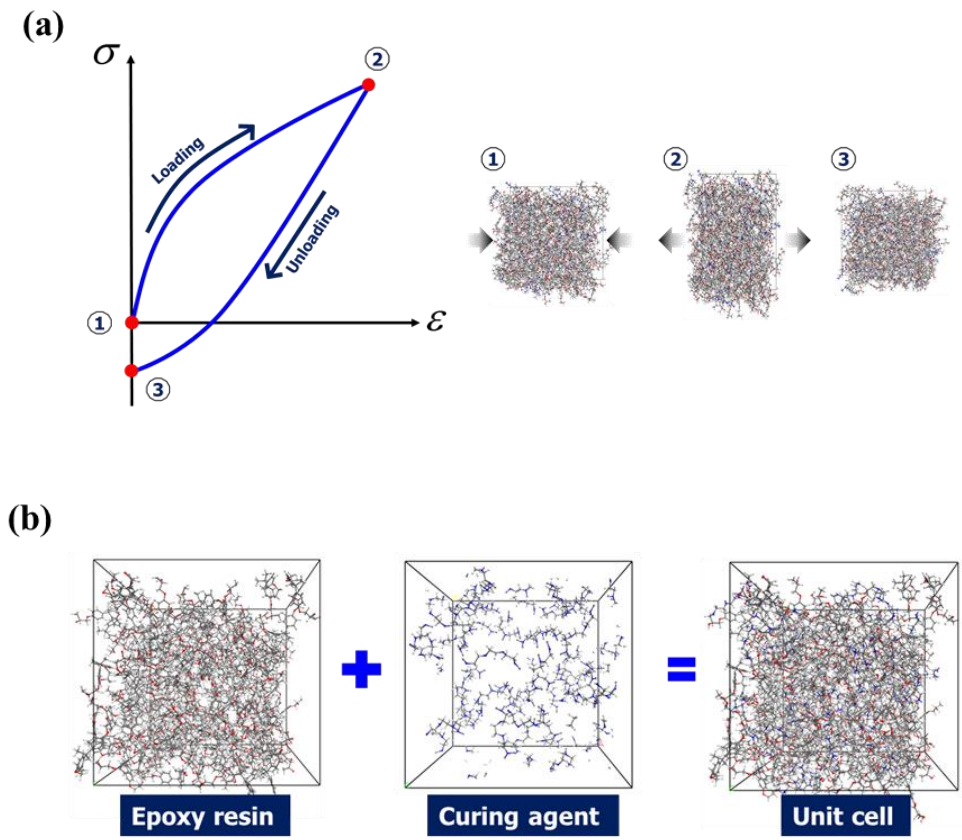

Fig. 2.7. Scheme for deformation simulations in the molecular dynamics (MD) environment with illustrations of: (a) the uniaxial compressive loading–unloading simulations and (b) the crosslinked monomers of the epoxy resin and the curing agents.

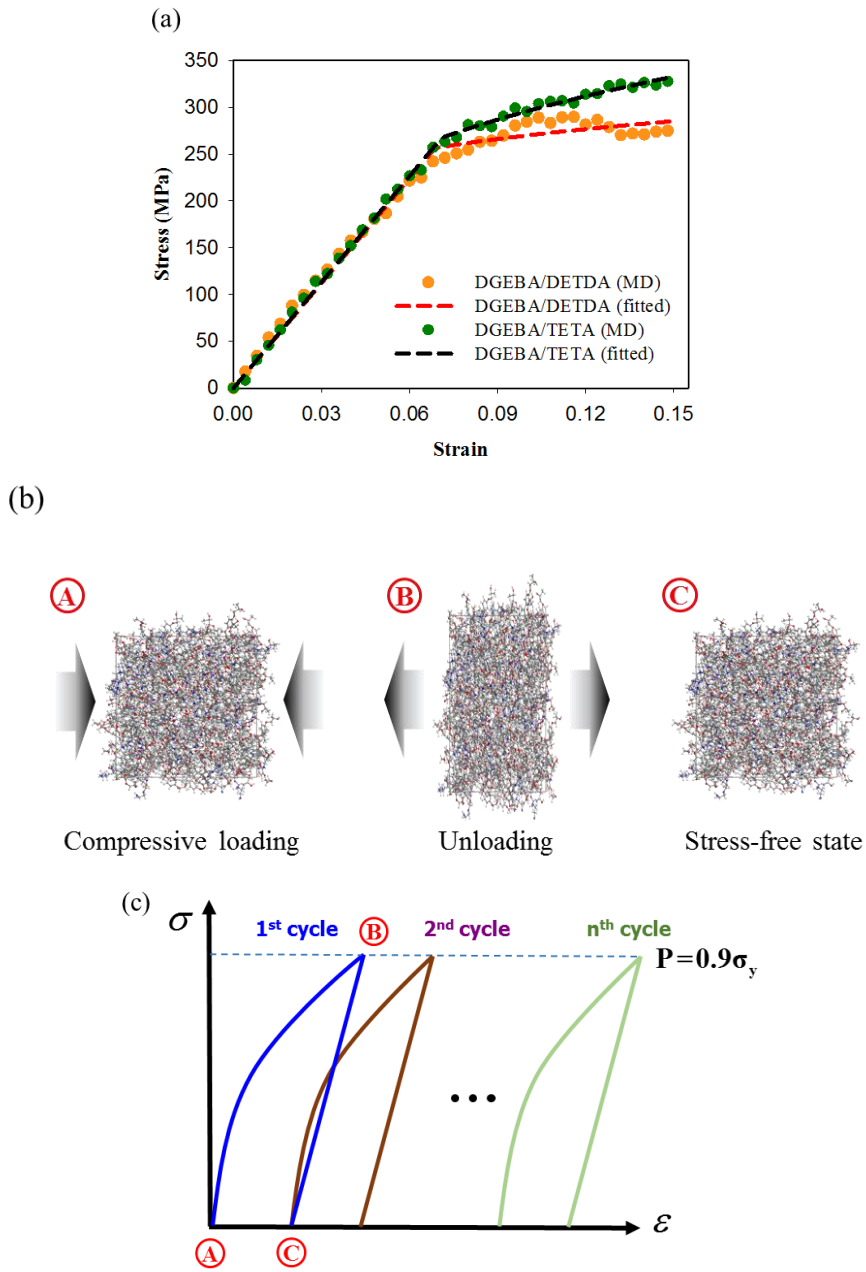

Fig. 2.8. Simulated (a) one–dimensional compressive stress–strain profiles for DGEBA/DETDA and DGEBA/TETA epoxy systems, (b) illustration for cyclic loading–unloading simulations by atomistic unit cell, and (c) scheme of the stress controlled cyclic loading–unloading simulations.

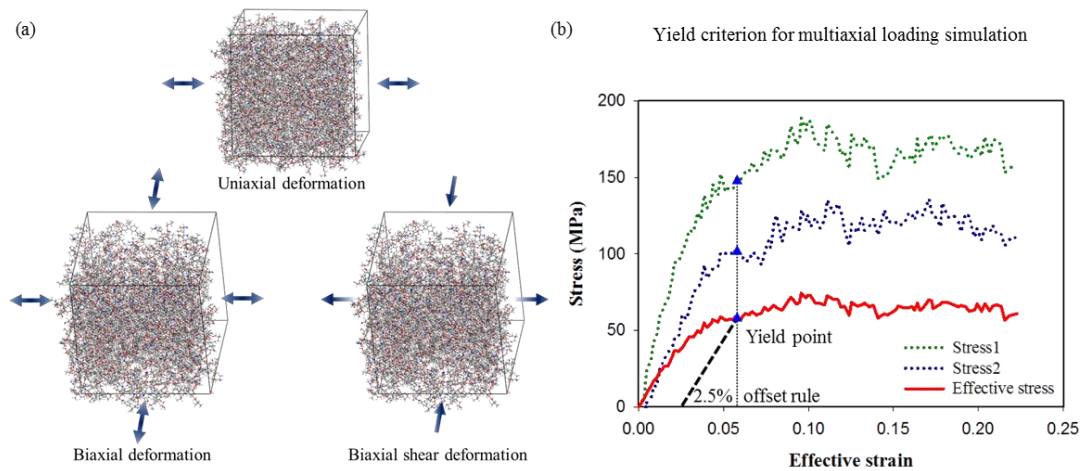

Fig. 2.9. Illustration for (a) deformation tests with constructed atomistic model and (b) obtained representative stress–strain profiles. The 2.5% offset criterion for yield point from the multiaxial stress–strains is used for the yield point selection. The red solid line is effective stress–strain and dotted lines are their components. The yield point is represented by triangle symbols.

Table 2.1.

Detailed Information of Epoxy-polymer Unit Cells at Room Temperature (RT).

Composition	Model	Number of Atoms	Crosslinking Ratio	Density (g/cc)	Number of Dihedral Angles	Cell Length (Å)
DGEBA/TETA	T1	8750	81.3 %	1.125	24282	44.16
	T2		77.3 %	1.116	24246	44.29
	T3		80.3 %	1.13	24273	44.11
DGEBA/DETDA	D1	9675	80.7 %	1.107	26226	45.89
	D2		82.3 %	1.11	26241	45.86
	D3		79.7 %	1.104	26217	45.93

Table 2.2

Comparison of mechanical properties of TGAP/DDS epoxy system with those given in experimental literature.

Present study				Experiment	
66% crosslinked TGAP/DDS				(Gonzalez-Dominguez et al., 2011)	
E (GPa)	G (GPa)	ν	ρ (g/cm3)	E (GPa)	ρ (g/cm3)
3.16	1.14	0.38	1.20	3.1 – 4.3	1.265

Table 2.3

Physical conditions for the considered epoxy unit cells.

Model	Xlink ratio (%)	Temperature (K)	Pressure (atm)
M1	80	0	1
M2	80	100	1
M3	80	200	1
M4	80	300	1
M5	75	300	1
M6	85	300	1
M7	80	300	1000
M8	80	300	3000

Table 2.4.

Comparison of the Mechanical Properties of the Epoxy Systems of the Diglycidyl Ether of Bisphenol A (DGEBA)/Triethylenetetramine (TETA) and the DGEBA/Diethyltoluenediamine (DETDA) Systems.

Mechanical Properties	DGEBA/TETA (Present Study)	DGEBA/TETA (Previous Study)		DGEBA/DETDA (Present Study)	DGEBA/DETDA (Previous Study)	
Young's modulus (GPa)	3.84	Experiment	MD	3.73	Experiment	MD
		2.42 [80]	4.98 [25]		2.71 [81]	4.00 [25], 4–8 [9]
Density (g/cm^3)	1.125	1.1240 [80]	1.14 [25]	1.107	-	1.12 [25], 1.12–1.14 [9]

3. Qualitative analysis on the elasto–plastic deformations of epoxy polymers

In this chapter, specific molecular mechanisms that induce macroscopic plastic deformations of amorphous epoxy polymers were investigated additionally considering effects of the molecular structures of curing agent. In **Chapter 3.1**, irreversible atomistic mechanisms correlated with energy and stress evolutions were characterized by monitoring local molecular structures during the deformations. In **Chapter 3.2**, it was elucidated how the different deformation characteristics influence the macroscopic plastic strain accumulations depending on the molecular structures of curing agent.

3.1. Influence of the molecular structure of curing agent on plastic deformations

3.1.1 Microscopic deformation mechanisms

- **Local structures of the epoxy polymers**

The local structures of fully equilibrated epoxy polymers were investigated using the derivation of the radial distribution function (RDF). The RDF is the probability measure for the identification of the position of a certain pair of atoms at a given distance *r* from a reference position. The RDF is defined using the following equation:

$$g_{\alpha\beta}(r)=\frac{n_{\alpha\beta}(\mathrm{r})}{4\pi r^2(N_\alpha N_\beta / V)}, \tag{3.1}$$

where $n_{\alpha\beta}(r)$ is the number of atom pairs that consist of the α- and β-atom species within a spherical shell in the distance range of $(r-\frac{\triangle r}{2}, r+\frac{\triangle r}{2})$, where N_α and N_β are the numbers of the atom species α and β, respectively, and V is the systemic volume. The RDFs of the considered epoxy polymers are given in Fig. 3.1. Herein, the atomic pairs of the monomers of the curing agents and the epoxy resin are respectively investigated to observe the influences of the structural characteristics of the curing agents on the network topology.

As can be seen in Fig. 3.1 (a), the discrepancy of the RDF values of the curing agents is noticeable between the two epoxy systems since the chemical structures of the two epoxy systems are different. The sharp first peak appears at around 1.1Å in both epoxies, which corresponds to the C–H bond. The first DGEBA/TETA peak is higher than that of the DGEBA/DETDA epoxy system. The second DGEBA/TETA peak appears at around 1.5 Å, which is attributed to the correlation of the N–H bonds. At around 1.45 and 1.53 Å, the second and third DGEBA/DETDA peaks are evident with relatively small heights, respectively, and these small peaks are associated with the bond lengths of the N–C and C–C bonds, respectively. The C–C bonds are mainly composed of a single C atom in a benzene ring and one C atom that is linked to the benzene ring. The third DGEBA/TETA peak and the fourth DGEBA/DETDA peak appear at around 1.75 Å, and these correspond to the lengths between the hydrogen (H) atoms in the H–C–H bond. The

next peaks (at around 2.2 and 2.5 Å) have been attributed to the correlation between the H and C atoms or to those between the C and C atoms in the H–C–C, C–C–C, and C–C–C–C sequences.

Unlike the RDF values of the curing agents, the RDF value of the resin represents similar structural characteristics. As can be seen in Fig. 3.1 (b), the RDF values of the two epoxy systems denote similar profiles, where a noticeable shifting of the peaks is not evident. Although the heights of the first peaks that are at around 1.1 Å, which correspond to the lengths between the H atoms, are different from each other, the effect of the distance between the H atoms on the packing of the monomers is not significant. This finding implies that the crosslinking implementations with the different curing agents that are considered in this study cannot significantly modify equilibrated epoxy-resin network structures.

- **Uniaxial loading–unloading simulations of the epoxy polymers**

To determine the primary internal-potential components from the energy perspective, the energy-accommodation profiles of both epoxy systems were derived at 300 K in the loading–unloading ranges that are shown in Fig. 3.2. In the responses of both epoxy systems, the total potential energy, which is the sum of the internal-energy components, increased in the loading range and decreased in the unloading range. Notably, a full recovery of the accommodated-energy state to the initial-energy state is lacking in either system; that is, the residual potential energies were observed at the end of the

unloading owing to the plasticity effect. These residual potential energies have been mainly attributed to the contribution of the nonbonded pairwise interactions (red lines in Fig. 3.2) of both systems, thereby implying that the interchain interactions were involved in the plastic-deformation energy accommodation that is a result of the irreversible structural rearrangement of the epoxy networks. Following the nonbonded pairwise interaction, the angle and dihedral-angle interactions noticeably accounted for the total potential-energy accommodation in both epoxy systems. Unlike the energy behavior of the nonbonded pairwise interaction, however, the irreversible residual energies are not shown in these angle-related interactions. When the two epoxy systems were compared, a quantitative difference was observed between the energy evolutions for the angle and the dihedral angle. It is noticeable that the dihedral-angle interaction accommodated a much larger deformation energy than the angle interaction in the DETDA-cured epoxy, while these two internal energy components show a similar energy-accommodation trend in the TETA-cured epoxy. Meanwhile, the influence of the bond contraction is negligible, as the bond energies in both systems show the absence of a meaningful increment in either the elastic- or plastic-strain ranges compared with the other internal-energy evolutions.

The derivation of the virial-stress and internal components of the TETA- and DETDA-cured epoxy systems are shown in Fig. 3.3. The total virial-stress values of the two epoxy systems show the typical deformation regime for thermosetting polymers, as can be seen in Fig. 3.3 (a). The two epoxy systems show a linearly increasing stress trend in the elastic-strain range, and the yielding began after a strain of approximately 0.07, when

the linearity collapsed. Then, the epoxy polymers displayed a hardening or a weak-strain softening in the plastic-strain range, as is the case in other studies[21,27]. Under the unloading-strain range, the epoxy-system stress rapidly decreased with the decreasing of the strain, eventually reaching a stress-free state, as can be seen in Fig. 3.3 (a). The stress-free state was reached at a strain of approximately 0.07, implying that the loading–unloading deformations of the epoxy polymers exhibited a distinct plastic-strain energy that can be calculated using the area of the loading–unloading stress–strain profile. During the unloading response, the stiffness decreased as the strain was decreased and it tended to converge in the elastic region.

The total virial stress can be divided into the internal-stress components, like the case of the energy components. The components are the nonbonded, bond, angle, and dihedral-angle terms that correspond to Eq. (2.2), and the stress evolutions are shown in Figs. 3.3 (b), 3.3 (c), 3.3 (d), and 3.3 (e), respectively. Among these internal-stress components, the dihedral-angle stress accounts for the largest portion of the total stress evolution in both epoxy systems. Following the dihedral-angle stress, the angle stress accounts for the second-largest part of the total stress evolution during the deformations. The dihedral-angle and angle interactions in the epoxy polymers are the primary potential parameters that mainly influence the stress–strain equation. The other parameters mainly contributed to the intrinsic deformation regime of the epoxy polymers. The nonbonded and bond stresses increased up to a strain of approximately 0.07 and then decreased, implying that the slope decrease in the total stress evolution of the plastic-strain range is

predominantly attributed to the contributions of the nonbonded and bond stresses.

Although the deformation regimes of the two epoxy systems are similar, it is possible to estimate the influences of the epoxy networks on the deformation behaviors from a quantitative comparison between the stress profiles. As the different 3D networks of the epoxy polymers in the present study are due to the structural differences in the curing agents of the epoxy system, the quantitative differences in the stress–strain behaviors results from the structural differences between the aliphatic and aromatic curing agents. As far as the total stress evolutions are concerned, the stress increments for both systems in the elastic range are nearly the same and show similar elastic-stiffness values. As the strain was applied beyond the yielding point, however, the extent of the hardening is different for each system, and the TETA-cured epoxy polymer shows a stress that is higher than that of the DETDA-cured epoxy polymer. This trend was continuously maintained under the unloading response, as follows: The TETA-cured epoxy polymer shows a higher stress and unloading stiffness. It is worth noting that this quantitative-stress difference between the two epoxies in the plastic range has been mainly attributed to the contributions of the angle and dihedral-angle stresses. From the previously described observations and the previous studies[26,27], the dihedral-angle-related behavior, which is influenced by the structure of the curing agent, is of primary importance, because the dihedral-angle stress significantly contributed to the elastoplastic stress–strain behaviors of the epoxy polymers. Therefore, the focus is the dihedral-angle stress behaviors.

The dihedral-angle stress still shows positive values even after the stress-free state was passed during the unloading, while the nonbonded, bond, and angle stresses denote negative values at the end of the unloading, as can be seen in Figs. 3.3 (b), 3.3 (c), 3.3 (d), and 3.3 (e), respectively. This result implies that the stress that is involved with the dihedral angle represents a compressive behavior, although the overall stress of the bulk system displayed a tensile behavior (negative values after the stress-free state). Owing to the irreversible stress behaviors of the dihedral angle, the dihedral-angle stresses of the two systems displayed residual stresses even at the end of the unloading, as can be seen in Fig. 3.3 (e). This result implies that plastic transitions are involved in the dihedral-angle behaviors, and these behaviors are dependent on the crosslinked networks that are determined by the structure of the curing agent. In a comparison of these two epoxy systems, the DETDA-cured epoxy system shows a higher irreversible dihedral-angle stress at the end of the unloading, revealing that the aromatic curing agents in epoxy polymers play a critical role in the plastic-stress behaviors.

It is worth noting that the irreversible stress behaviors were identically observed in the dihedral-angle stress–strain profiles of all of the prepared initial configurations (the profiles in Fig. 3.3 are averaged over different initial configurations, velocity distributions, and loading directions). These data denote that the observed residual stress that was observed at the end of the unloading is reproducible and reliable.

- **Influence of the structures of the curing agents on the stress behaviors**

To investigate the contributions of the curing agents on the obtained residual dihedral-angle stresses of Fig. 3.3 (e), the monomers of only the curing agents were independently observed during the loading–unloading simulations, as shown in Fig. 3.4 (a). The dihedral-angle stresses of only the curing-agent monomers of both epoxy systems are represented in Fig. 3.4 (b). In this profile, distinctly different dihedral-angle stress behaviors are evident. The curing agent of the DETDA-cured epoxy (blue lines) shows a large increase in the loading-strain range and a small decrease in the unloading-strain range that result in an evident residual stress at the end of the unloading. The curing agent of the TETA-cured epoxy system (red lines), however, shows a spring-like reversible stress increase and decrease in the loading and unloading ranges, respectively. The dihedral-angle stresses of the aromatic-curing-agent monomers accumulated in terms of the plasticity due to the accommodation of a large deformation energy compared to the stress response of the aliphatic-curing-agent system. Then, these plastic dihedral-angle stress behaviors eventually contributed to the irreversibility of the total dihedral-angle stress behavior. These residual dihedral-angle stresses are evident in the responses of all of the considered initial configurations, as can be confirmed by the error bars. These observations provide clear evidence of the significant influences of the structural types of curing agent on the plastic-deformation behaviors of epoxy polymers. In particular, they imply that the monomers of aromatic curing agents should represent a plasticity that is characterized by the dihedral-angle behavior.

The influences of the two types of curing agent on the epoxy-resin monomers were investigated in a manner that is similar to that of above section. Among the internal-stress components, the angle stresses that are between the two systems of only the epoxy-resin monomers, which are shown in Fig. 3.4 (c), were compared. Although both epoxy systems are composed of the same type of epoxy-resin monomer, DGEBA, the angle-stress profile denotes the quantitative discrepancy between them. The TETA-cured epoxy resin exhibited a higher-angle stress than the stress of the DETDA-cured epoxy resin; however, although the amounts of the stress increment are different, the angle stresses of the two epoxy resins converged to the same value at the end of the unloading. These observations revealed that the local angle in the epoxy-resin monomers changes to accommodate different deformation-energy amounts in the loading response depending on the structural characteristics of the curing agent, but the amounts of the plastic-energy dissipation of the two systems are approximately similar. This finding can be confirmed using a calculation of the surrounding areas for which the curves of Fig. 3.4 (c) are applied.

- **Geometric characteristics: relative atomic displacement (RAD) analysis**

For an improved understanding of the plastic stress and energy behaviors, the intrinsic geometric properties of the epoxy polymers were investigated using the relative atomic mobility (RAM) analysis. From this analysis, an estimation of the mobility discrepancy of the epoxy monomers or specific atoms, which is featured in the molecular structures of the epoxy networks, was performed during the loading–unloading simulations.

The derived RAM values of specific atom types and monomer sets are displayed in Figs. 3.5 (a) and 3.5 (b) based on the deviation of the atomic displacement along the time increment, as follows:

$$RAM(t)=\frac{1}{N}\sum_{i=1}^{N}|\,r_i(t)-r_i(0)\,|^2\,, \tag{3.2}$$

where $r_i(t)$ and $r_i(0)$ denote the current positions of the *i*th atom at the times *t* and zero, respectively, and N denotes the number of the specific group of atoms. That is, the RAM values were calculated using the averaged considered atoms in the epoxy networks to estimate the relative mobility of the considered group during the dynamic response. As the applied strain is linearly proportional to the time, Eq. (3.3) is described based on the strain increment ε, as follows:

$$RAM(\varepsilon)=\frac{1}{N}|\,r_i(\varepsilon)-r_i(0)\,|^2\,, \tag{3.3}$$

where $r_i(0)$ denotes the position of the *i*th atoms at the initial loading state. Based on Equation (3.3), the derived RAM profiles of the DGEBA/TETA and DGEBA/DETDA epoxy systems are shown in Figs. 3.5 (a) and 3.5 (b), respectively. To independently investigate the mobility of certain sets, the RAM values of the local sets were calculated through groupings of the specific atoms and monomers for the curing agents and the epoxy resin and the carbons of the benzene rings in the curing agents and the epoxy resin. In particular, the focus of this chapter is the observation of the atomic mobility of the carbons in the benzene rings, as the differences in the characteristics of the aliphatic and aromatic

curing agents mainly arise from the existence of a benzene ring[25,82]. As shown in the profiles of both systems, the RAM values increased nonlinearly in the loading range, showing an increase of the curve slope. This trend implies that the local diffusions of the polymer chains that are due to the external force occur more actively when the plastic behaviors are involved in the deformation processes; moreover, this observation suggests the possibility that, as the plastic deformations proceed, the instantaneous diffusivity of the local atoms in the polymer segments tends to increase and provides more room for polymer-chain movements. Further, the mobility discrepancy between the initial loading state and the final unloading state is evident in both epoxy systems; that is, the mobility of the final unloading state is higher than that of the initial loading state. This observation reveals that, although the strains in the loading directions are equal between the two states, the chain-segment diffusion occurred actively in the unloading range compared with the corresponding strain in the loading range; that is, the mobility discrepancy between the loading and unloading ranges could provide evidence of proceeded plastic deformations in the loading range.

The mobility characteristics of the benzene ring can be estimated from the results of Figs. 3.5 (a) and 3.5 (b). Since the monomers of the epoxy resins in the two epoxy systems are entirely equal, the same numbers of benzene rings are present in the epoxy resins of both systems. In the case of the considered curing agents, however, the aromatic curing agent, DETDA, includes only the benzene rings. As can be seen in Fig. 3.5 (a), the RAM of the C atoms of the benzene ring in the epoxy-resin monomers (solid red lines) is

much lower than those of the other atoms (solid cyan lines). Further, this mobility gap increased in the unloading range compared with the loading response, while this trend is much clearer in the response of the DGEBA/DETDA epoxy system, as can be seen in Fig. 3.5 (b). The solid red and blue lines denote the RAM values of the benzene atoms in the epoxy resin and the curing agents, respectively. Both curves display similarly increasing and decreasing trends with the benzene rings in the TETA-cured system in the loading–unloading range. The most interesting point in this figure is that the RAM of the benzene rings in the curing agent is much smaller than that of the epoxy-resin monomers in the unloading range, and this gap increased as the unloading simulation was proceeded. This result means that the deformed epoxy networks severely restricted the motions of the benzene rings in the curing agent in the unloading range, while the mobility degrees of the other linked atoms are relatively high.

The mobility analysis eventually resulted in the following important physical insight: The benzene rings, especially in the curing-agent monomers, are likely to show significantly limited movements compared to their connected atoms during the loading–unloading responses. By contrast, the aliphatic curing agent, TETA, shows a relatively high degree of mobility since it is not composed of any benzene rings. In this regard, a simple illustration of the obtained mobility results is shown in Fig. 3.5 (c). As shown in the illustration of the DETDA-cured epoxy system, a mobility gap is present between the C atoms of the benzene rings and their linked chain. This mobility discrepancy suggests the possibility of plastic dihedral-angle transitions in the vicinity of the benzene rings and their

linked atoms, thereby exerting a significant influence on the plastic behaviors of the dihedral-angle stress. Thus, in the following section, a rigorous monitoring of the dihedral-angle type, which consists of the benzene rings and their linked atoms from the energy perspective, is described.

- **Selection of the primary dihedral-angle types for plastic dihedral-angle transitions**

Based on the results of the mobility analysis in previous section, a thorough monitoring of the dihedral-angle transitions of the dihedral-angle sets, which are partially composed of benzene atoms, was conducted during the deformation simulations. The two dihedral-angle types that were selected exhibited large energy variations during the deformations. The selected dihedral-angle types are represented in Fig. 3.6 (a), as follows: *Type A* and *Type B*. Type A consists of two benzene atoms and their connected O and C atoms, while Type B consists of two benzene atoms and their connected N and C atoms. Type A is included in the monomers of the epoxy resins of both systems, but Type B is included only in the DETDA-cured epoxy system because Type B is composed of the benzene atoms that are included in the curing-agent DETDA. The dihedral-energy changes of these two selected epoxy-system types are shown in Figs. 3.6 (b) and 3.6 (c). As far as the TETA-cured epoxy system is concerned, Type A exhibited a large energy accommodation that is similar to the total energy-increase amount, but it does not display

a clear residual energy at the end of the unloading. As far as the DETDA-cured epoxy system is concerned, a large energy-increase amount is evident in the loading and is relatively well maintained during the unloading. Type B in the DETDA-cured system, however, did not display energy increases or accumulations like the global energy responses of Fig. 3.2.

This result is not desirable, but it is understandable because of the following reason: The considered thermostat for the NPT-ensemble-based deformation simulation adjusts and dissipates the energy to constantly maintain the target temperature. This reason is also suggested as the origin of the contradictory stress–energy relationships in the work of Hossain et al.[26]. In their study, the potential energy was decreased under a deformation condition that showed an inversely proportional relationship with the stress evolution. Their observation is the result of a simulation condition that is fairly similar to the profile of the dihedral energy in Fig. 3.6. Another point of view is that the present simulation only covers very-short-term dynamics in the region of several nanoseconds. An inevitable limited sampling of the energy state of the set of the local atoms during the short-term dynamics cannot avoid the inherent fluctuations that result from the initial velocity imposition that corresponds to the considered temperature condition. In this regard, tremendous efforts have been made in the current MD simulations to overcome the timescale limitations[83–85]. Thus, in the following section, the performances of deformation simulations that are less than 1 K for the avoidance of the effects of high thermal-energy

levels are presented. The plastic dihedral transitions and the related energy evolutions are also derived.

3.1.2. Dihedral energy analysis

- Plastic dihedral-energy behaviors

To observe the intrinsic dihedral-energy behaviors without the exertion of large fluctuation effects on the energy profiles, the deformation simulations were performed at 1 K with simulation conditions that are identical to those that are used at 300 K. The energy evolutions were derived for Type A and Type B in both systems, as shown in Fig. 3.7. The total dihedral energies in both systems increased in the loading range and decreased in the unloading range, as can be seen in the response at 300 K, and these outcomes are shown in Figs. 3.7 (a) and 3.7 (c), respectively. In the profiles of the total dihedral energies, however, the residual dihedral energy is not clearly evident in either system; rather, the dihedral energy decreased toward a much lower energy state, especially in the DETDA-cured epoxy.

Concerning the dihedral-energy evolutions of Type A and Type B, however, a clear plastic trend was observed. As shown in Fig. 3.7 (b), in the TETA-cured system, the response of Type A displays some residual energy at the end of the unloading. Likewise, in the DETDA-cured system, the response of Type A denotes a slight residual energy at the end of the unloading, as shown in Fig. 3.7 (d). As far as the dihedral angles of Type B are

concerned, the dihedral energy was clearly accumulated during the entire deformation process, thereby implying that the dihedral angles of Type B are more likely to exhibit an irreversibility from the energy perspective than the dihedral angles of Type A. The difference in the extent of the irreversibility of the dihedral energy between Type A and Type B can be attributed to the mobility difference between the benzene rings of the DETDA-cured epoxy, as shown in Fig. 3.5 (b). As presented in RAM analysis, a mobility difference was observed between the benzene rings in the epoxy resin and the curing agents that is owing to the effects of the different networking environments in the vicinities of these two types of benzene ring. Although the considered temperature conditions are different, the results that are shown in Fig. 3.5 (b) can be applied equivalently to the results at 1 K, because the plastic behaviors of the local dihedral-angle sets have been attributed to the geometric properties that are derived from the molecular structures of the considered system.

- Plastic dihedral-angle transitions in the DGEBA/DETDA epoxy system

To specifically observe the local plastic dihedral-angle transitions, the dihedral-angle sets of Type A and Type B in the aromatic-cured epoxy system were monitored during the deformations. The related dihedral-energy surfaces with the dihedral-angle changes of both types are represented in Fig. 3.8 (a). The local energy states can be divided into low and high ranges at the angle interval of 90º. As the deformations progress in the loading range, the local dihedral angles changed with the energy increment from the low- to the

high-energy state, as shown in Fig. 3.8 (a). If the local dihedral angles are abruptly changed owing to the external loading, the deformed dihedral angles stay in the high potential state during the unloading, or they elastically return to the low-energy state. The representative case studies of the plastic dihedral-angle changes of Type A and Type B are denoted in Figs. 3.8 (b) and 3.8 (c), respectively. In both profiles, the dihedral angles were changed during the loading response (solid lines) toward the high potential state, and they were maintained during the unloading response (dotted lines). These plastic transitions occurred abruptly during the loading, overcoming the potential energy barrier that exists between the local energy basins. The local dihedral transitions of Type A and Type B from the low- to the high-energy states are similar to the trans-gauche dihedral conformational changes of thermoplastic polymers[26,27].

These abrupt local transitions that occur near the benzene rings can be explained by the classical yielding theory of amorphous polymers that was proposed by Argon[44,45]. According to this theory, the yielding of amorphous polymers occurs via the molecular kinks of flexible polymer chains that are activated by applied deformations. According to this theory, until the occurrence of the yield point, the internal networks endure the applied deformation with a linear stress increment that corresponds to the elastic-stress evolution, which is shown in Fig. 3.3 (a). As the molecular kinks of the polymer chains are activated by the applied load, the internal stress is gradually relaxed, thereby denoting inelastic stress–strain behaviors.

The detailed relationships between the wedge angle, stress, and energy change are well described in the work of Sundararaghavan et al.[21]. When compared to the present MD results, the kinks of the local polymer chain that are represented in Argon's theory correspond to the abrupt dihedral-angle changes in Figs. 3.8 (b) and 3.8 (c). It has already been concluded in the RAM analysis that the plastic dihedral-angle transitions have been mainly attributed to the differences between the mobility and the stiffness of the local benzene rings and their linked chains. This results in the important conclusion that the differences of the curing-agent chemical structures between the aliphatic and aromatic types significantly influences the kinking behaviors of the local polymer chains, and this eventually determines the yielding phenomena of the epoxy polymers. That is, considering the large contribution of the dihedral-angle stress to the total stress–strain response, the dihedral-angle folding behaviors of Type A and Type B exerted a significant effect on the elastoplastic mechanical properties.

Thus, the numerical variations in the plastic dihedral-angle transitions of Type A and Type B have been derived for the quantitative investigation and are shown in Figs. 3.8 (d) and 3.8 (e), respectively. Both of the dihedral types show an increasing trend in the loading range. In particular, the numerical plastic-transition ratio jumps abruptly near the strain of approximately 0.06, which corresponds to the trend of the dihedral-energy evolution in Figs. 3.7 (d) and 3.7 (e). As the unit cells were unloaded, however, the number of the plastic transitions of Type A noticeably decreased, while Type B showed a considerable increase, as is the case for the energy evolutions. The dihedral angles for both

types accommodate the large deformation energies during the loading response; however, the dihedral angle of Type B is more advantageous for plastic transitions in terms of the two different benzene-linked dihedral types.

3.1.3. Strain-rate dependency of plastic dihedral-angle behaviors

It is necessary to confirm the identical maintenance of the characterized inelastic-deformation mechanisms as the strain rate was decreased. Accordingly, the relationship between the increased relaxation time for the chain segments and the plastic dihedral-angle stress behaviors, which result from the plastic dihedral-angle transitions of Fig. 3.8, was constructed. To characterize the relationship between the strain rate and the plastic dihedral-angle behaviors, the loading–unloading deformation simulations were carried out at the low strain rate of 10^8/s with the same manner of 10^9/s. In Fig. 3.9, the total stress–strain profiles and the dihedral-angle stress–strain profiles of only the curing-agent monomers are presented. As the strain rate was decreased, the total virial stress also decreased, as can be seen in the comparison data of Figs. 3.9 (a) and 3.9 (b). The overall deformation trends of both epoxy systems, however, were similarly maintained. The stress was linearly increased up to the strain of approximately 0.05, and it was nonlinearly changed with the yielding of the epoxy systems. In particular, the stress of the DGEBA/TETA system is higher than that of the DGEBA/DETDA system at 10^9/s under

the plastic-strain range, as can be seen in Fig. 3.9 (a). An identical trend is observed in the stress–strain profiles at 10^8/s.

It is also possible to compare the dihedral-angle stresses of the curing agent at two different strain rates. As can be seen in Figs. 3.9 (c) and 3.9 (d), the observed residual dihedral-angle stresses in both of the strain rates at the end of the unloading are identical. The value of the residual dihedral-angle stress of 10^8/s is much higher, even though the total virial stress was decreased by up to approximately 100 MPa with the decrement of the strain rate. This observation implies that the increased relaxation time during the deformation activated the plastic dihedral-angle transitions of the dihedral angles of Type B.

3.2. Influence of the molecular structure of curing agent on ratcheting behaviors

In this chapter, the cyclic loading behaviors of glassy epoxy polymers were investigated by MD simulations considering the influence of the molecular structure of the curing agents. This chapter aims to understand the contribution of the irreversible torsional angle transitions on the macroscopic ratcheting behaviors of epoxy polymers by taking into account the influence of strain rate. This chapter considers two different epoxy systems consisting of different structures of curing agents (aromatic and aliphatic curing agents), conduct compressive cyclic loading–unloading simulations, and monitor the macroscopic ratcheting behaviors and stiffness variations. In order to correlate macroscopic ratcheting behaviors with molecular conformation change, we separately observe the microscopic transitions of the monomers of epoxy resin and curing agent by deriving structural parameters.

3.2.1. Ratcheting behaviors and stiffness evolutions

- Ratcheting behaviors of epoxy systems considering different curing agents

The ratcheting behaviors of DGEBA/DETDA and DGEBA/TETA systems were investigated and their stress–strain profiles and ratcheting strain evolutions are presented in Fig. 3.10. As expected, the stress–strain profiles of both systems evolved as the cycles

progressed. When both systems were compared, the stress–strain curve evolved much rapidly in the case of the DGEBA/DETDA system, denoting that the plastic strain prominently accumulated during the cyclic deformations. Correspondingly, the ratcheting strain also rapidly increased in the case of the DGEBA/DETDA system (see Figs. 3.10(c) and 3.10(d)). Visualization of this ratcheting discrepancy between two epoxy samples is presented in Figs. 3.10(e) and 3.10(f); initially, those two epoxy systems did not exhibit any difference in the cell size but, as the cyclic deformation proceeded, the height and width became gradually different for the two epoxies.

The abovementioned discrepancy in the plastic strain accumulation distinctively influences the sensitivity of frequency. The amorphous polymers exhibited clear rate dependence concerning the evolution of the ratcheting strain; the high frequency results in slow ratcheting strain evolution. The result for the DGEBA/DETDA system distinctively follows previous observations, although deviation of the ratcheting strain is smaller under a high number of cycles. This suggests that the conformational change in the epoxy cured by DETDA, which induces macroscopic accumulation of the plastic strain, is severely frequency dependent. However, the DGEBA/TETA system does not exhibit a clear frequency dependence; the ratcheting strain was almost equal up to 250 cycles and the ratcheting strain of high frequency (8.33 ns^{-1}) was rather large compared to the low frequency (4.17 ns^{-1}). This means that the structural change of the epoxy network was not significantly influenced by the increased relaxation time in the case of the epoxy system cured by TETA. This implies that the selection of an aliphatic curing agent like TETA is

advantageous from the viewpoint of fatigue life of idealized epoxy.

The ratcheting regime also exhibited obvious differences for the two epoxy systems. As far as the DGEBA/DETDA system is concerned, it displayed an entirely different ratcheting regime; an abrupt transition in the slope was observed at about 80 cycles. Based on this, the range that denotes rapid increase of the ratcheting strain transitioned into the second range that exhibits a minor increase (after the 80 cycles). Under both ranges, the rate of increase of the ratcheting strain was almost consistent without any transient range. This implies that the main molecular deformation mechanisms, which dominate the evolution of ratcheting strain, might be different under each range. Further, considering that these ratcheting behaviors were not observed in high-frequency conditions, it seems that the main molecular deformation mechanism is severely rate-dependent. This kind of transition of the ratcheting regime has also been observed for other classes of materials. Within the considered range of the cycles, it seems that the DGEBA/TETA system almost reached the threshold ratcheting strain. The instance that the system does not exhibit a clear increasing trend for the ratcheting strain is sooner at low-frequency conditions than at high-frequency conditions, while the ratcheting strain of DGEBA/DETDA system increases continuously under both conditions.

- Stiffness variations

Stiffness of the considered epoxies was examined based on the molecular structures deformed by cyclic loads. The snapshot models at 0 (initial), 100, 200, 300, 400,

and 500 cycles were tested to derive the elastic modulus. The stiffness results in the loading direction (E_{xx}) are presented in Figs. 3.11(a) and 3.11(b), the averaged stiffness results in the directions perpendicular to the loading (E_{yy} or E_{zz}) are presented in Figs. 3.11(c) and 3.11(d), and the results of shear stiffness perpendicular to loading (transversal shear), G_{yz}, are presented in Figs. 3.11(e) and 3.11(f). To observe the general trend of the stiffness variation, linear regression lines are simultaneously plotted in each figure. The stiffness in the loading direction decreases sharply with the number of cycles in the case of the DGEBA/DETDA system, while those of the DGEBA/TETA system does not exhibit obvious trend. In particular, the DGEBA/DETDA system exhibited a large loss in the stiffness even up to about 2 GPa after 500 cycles of loading–unloading, which implies severe rearrangement of the internal structure and microvoid generation (free volume evolution). Concerning the stiffness perpendicular to loading and shear stiffness, the stiffness perpendicular to loading increased slightly or remained constant in both epoxy systems and the shear stiffness exhibited a slightly increasing trend in both epoxy systems.

Similar to the ratcheting strain in Fig. 3.10, the DGEBA/DETDA system exhibited strong frequency dependence regarding the stiffness degradation, while the DGEBA/TETA system did not exhibit any clear trend. The stiffness in the loading direction decreased rapidly in higher-frequency conditions compared to the that in the low-frequency condition. The regression slope at high frequency was about 1.5 times of the slope in the low-frequency condition. Similarly, the stiffness perpendicular to loading and the transverse shear stiffness at low frequency exhibited relatively high values than those at high-

frequency conditions.

- Accumulation of irreversible dihedral angle stress

The dihedral angle stress, which exhibited entirely different deformation regimes according to the structures of the curing agent, was examined within the studied range of cycles as shown in Fig. 3.12. It was confirmed that the residual dihedral angle stress in the DGEBA/DETDA system after large strain loading–unloading simulations, which was observed in our previous work[24], was accumulated continuously during the cyclic deformation simulations. This implies that the irreversible conformational change related to the dihedral angle transitions continuously occurs proportional to the increasing number of cycles even below the critical stress. As can be seen in the evolutions of the dihedral angle stress of the entire epoxy system, the extent of the accumulation of the DGEBA/DETDA system is much higher than that of the DGEBA/TETA system (see Figs. 3.12(a) and 3.12(b)). This can be attributed to the contributions of the conformational change in the connecting part between the resin and curing agent of the DGEBA/DETDA system. This could be easily confirmed by evaluating the dihedral angle stress of the curing agent monomers; as can be seen in Figs. 3.12(c) and 3.12(d), the dihedral angle stress of the curing agent monomers was only observed in the DGEBA/DETDA system while the stress of the DGEBA/TETA system was nearly zero even after 500 cycles.

As far as the influence of the frequency is concerned, discrepancy in the frequency dependence was observed in DGEBA/DETDA depending on the type of monomers. As can

be seen in the dihedral angle stress of both epoxy systems, the accumulated stress at high frequency was slightly higher than that at low frequency (see Figs. 3.12(a) and 3.12(b)). However, the accumulated dihedral angle stress of the curing agent monomers was higher at low frequency than in the high-frequency condition. It implies that the irreversible folding near the connection atoms in curing agents requires more relaxation time than the folding behaviors in resin monomers. It also suggests the importance of irreversible folding in curing agent with a prolonged timescale that classical MD simulations cannot cover. In the case of thee DGEBA/TETA system, there was no frequency-dependent behavior since the curing agent cannot possess the stress related to dihedral angle transitions.

3.2.2. Microscopic structural analysis

In this chapter, microscopic structural characteristics were investigated by means of analyses on orientation parameters, radius of gyration, and free volume to understand the ratcheting behaviors and stiffness degradations at microscopic scale.

- Orientation parameter

Orientation order parameters of the monomer sets in epoxies were monitored to identify the rearrangement of the microstructure during cyclic deformations. The concept of the orientation order parameter of the epoxy network was borrowed from the definition

of orientations of the backbone bonds of polymers. The orientation order parameter in a certain direction is determined from the vector calculated by the maximum and minimum coordinates in certain monomer employing the following expression:

$$S_x = \frac{1}{2}\left(3\cos^2\theta_x - 1\right), \tag{3.4}$$

where $\cos\theta_x$ is the directional cosine of each monomer in the epoxy network toward the loading axis of the atomistic cell. The threshold value of the orientation parameter is -0.5, 0.0, and 1.0 for perpendicular arrangement to the loading axis, random arrangement, and parallel alignment to the loading axis, respectively.

We investigated the orientation parameters of monomers of the epoxy resin, curing agent, and the entire system to individually observe the rearrangement of each monomer set. The results are presented in Fig. 3.13; Figs. 3.13(a) and 3.13(b) show the evolutions of the orientation parameters at high frequency and Figs. 3.13(c) and 3.13(d) show the evolutions of the orientation parameters at low frequency. The results revealed that the monomers of the epoxy resin were prominently aligned perpendicularly to the loading direction within both epoxies for all considered frequencies, affecting the macroscopic ratcheting strain (see the representative conformational change of resin monomer in Fig. 3.13(e)). In particular, it seemed that the change in the orientation parameter of the resin monomers account for the alignment of the entire epoxy system of DGEBA/DETDA, since the orientation order parameter of the DETDA did not exhibit

obvious reorientation. It is natural considering the small molecular structure of the curing agent, DETDA. Regarding DGEBA/TETA, similar to DGEBA/DETDA, the influence of the alignment of the resin monomers was dominant in plastic deformations at high frequency. However, it was confirmed that the contribution of the curing agent on the orientation parameter of entire system increased under low frequency due to the prolonged relaxation time, which can be confirmed in Figs. 3.13(b) and 3.13(d). It suggests that the involvement of the curing agent in the stress possession (other than dihedral angle stress) increased with increased relaxation time.

- Radius of gyration

To intensively observe the overall positions of the epoxies, radius of gyrations of the resin monomers were additionally investigated here. The radius of gyration R_g of each system was calculated by the weight of atomic mass and deviation of the position of each atom and center of mass of system as:

$$R_g^2 = \frac{1}{\sum m_i} \sum m_i \left[(x_i - x_{cm})^2 + (y_i - y_{cm})^2 + (z_i - z_{cm})^2 \right], \tag{3.5}$$

where $m_i, (x_i, y_i, z_i), (x_{cm}, y_{cm}, z_{cm})$ denote the mass of the constituent atom and its position vector and the position vector of the center of the mass of system, respectively. We monitored the transition of R_g during the whole cyclic deformations and the results are presented in Fig. 3.14. Similar to the trend for the orientation parameter, it was observed

that the chain segments were redistributed and rearranged perpendicularly to the loading direction (x–axis). The polymer segments were contracted in the loading direction and expanded along the y- and z-axis. The degree of these molecular rearrangement exhibited a discrepancy between the two epoxies, following the ratcheting strain evolution in Fig. 3.10 exactly. Under the low frequency, the difference of redistribution of epoxy network was more marked, implying that the molecular mechanism causing low ratcheting resistance was intensely activated by the increased relaxation time.

- Free volume

It is of importance to intensively observe the evolution of free volume considering their huge influence on the mechanical properties especially for the modulus. Thus, in this part of the work, the free volume of fully loaded and unloaded states in each cycle was monitored during the cyclic deformations and the results are shown in Fig. 3.15. The free volume was estimated by the volume excluded by the occupied volume of the polymer chains. The occupied volume is generally defined by the van der Waals surface and solvent surface, which is determined by the probe rolling over the van der Waals surface. To calculate the free volume, solvent probe radius of 2 $\mathring{\mathbf{A}}$ and van der Waals radius of 9.5 $\mathring{\mathbf{A}}$ were used for the description of the solvent surface and van der Waals surface. The derived evolutions of the free volume are presented in Fig .3.15.

The results exhibit quite complex frequency dependence depending on the

molecular structures of the curing agent. The free volumes of DGEBA/DETDA increased more sharply at low frequency up to about 80 cycles and then decreased and was constant. After that, the free volume evolutions of DGEBA/DETDA exhibited clear frequency dependence; the free volume at lower frequency was much lower than that at higher frequency. Regarding the free volume evolutions of DGEBA/TETA, the free volumes of two frequencies were at almost same values up to around 300 cycles. After that, the free volume at high frequency decreased abruptly in both loading and unloading states, showing a reverse trend compared to that of DGEBA/DETDA.

3.2.3. Relationship between epoxy structure and ratcheting behavior

The ratcheting behaviors of the highly crosslinked epoxy polymers were studied considering the influence of the molecular structures of the curing agents. The studied epoxy polymers exhibited significantly different ratcheting characteristics coming from the different roles of the curing agent in deformation accommodations. The ratcheting strain was highly accumulated within the epoxy cured by DETDA, exhibiting low ratcheting resistance. The distinct ratcheting regime was observed; the rate of the ratcheting accumulation was fast in early stage of the cyclic deformations and converged in both epoxies. The influence of the frequency was also estimated considering the frequencies of 8.33 ns^{-1} and 4.17 ns^{-1}, revealing that the epoxy cured by DETDA exhibited huge frequency

dependence while the epoxy cured by TETA does not exhibit clear frequency dependence in ratcheting strain evolutions. The stiffness evolutions were also studied by observing the stiffness along the principal axis of the atomistic cells and shear stiffness. The stiffness along the loading axis is highly decreased in the epoxy cured by DETDA as the cyclic deformation proceeds, while the stiffness of epoxy cured by TETA does not exhibit clear degradation of modulus. The stiffness perpendicular to loading and shear stiffness transverse to loading moderately increase during the cyclic deformation in both epoxies. The applied deformations result in the stress accumulations induced by the irreversible conformational transitions of dihedral angles in the vicinity of benzene rings. The dihedral angle stresses of both epoxies were obviously accumulated by the involvement of the epoxy resins. But, it exhibited entirely different deformation accommodation trend when only observing the curing agent that DETDA irreversibly accommodate the applied stress in epoxy network while TETA only stored the applied stress by reversible molecular behaviors.

To understand the above ratcheting behaviors and stiffness transitions, the microscopic structures of the epoxies were observed by measuring the orientation order parameters, radius of gyrations, and free volumes during the cyclic deformations. Accordingly, we concluded that;

- The curing agent TETA play a different role in the deformation accommodation compared to DETDA, leading to the possibility of high ratcheting resistance of DGEBA/TETA; DETDA easily transfer the applied stress into the epoxy resin causing alignment of resin monomers perpendicularly to the loading, while

TETA stores the applied stress by self–deformation.

- The observations on the orientation order parameters revealed that the increase of the ratcheting strain significantly originated from the alignment of the resin monomers perpendicularly to the loading direction. DETDA does not contribute to the ratcheting strain due to its small molecular size. TETA requires increased relaxation time for its contribution on ratcheting strain accumulations.
- Rapid increase of ratcheting strain in early cycles of the deformation is correlated with the alignment of the resin monomers and corresponding abrupt increase in free volumes. Subsequent slow increase of the ratcheting strain regime stems from the gradual free volume decrease by the overall chain relaxations of epoxy network.
- Stiffness degradation along the loading direction in DGEBA/DETDA is significantly influenced by the free volume evolutions. In particular, the large stiffness reduction at high frequency is arising from the slow decrease in free volume rather than chain reorientation.
- Selection of the curing agents is of significant importance in fatigue life of epoxy polymers due to their role in load transfer to resin monomers. In particular, the curing agents that can independently possess the applied stress is advantageous for the ratcheting resistance and stiffness evolutions.

It needs to be noted that the present study focused on the idealized structure of the epoxy polymers and does not consider the influences of the chain scissions and initial microvoids,

which could be critical to the fatigue lives of the amorphous polymers. These issues needs to be studied with the aid of large time and spatial scale simulations which cannot be achieved by full atomic simulations. Thus, the future investigation will concentrate on the development of the framework that can quantitatively predict the ratcheting behaviors, simultaneously considering abovementioned limitations of present study.

3.3. Summary

The deformation mechanisms of highly-crosslinked epoxy polymers have been investigated using MD simulations in consideration of curing agents with different structures. Structurally different epoxy unit cells were prepared in an MD environment wherein the following different curing agents were considered: aliphatic and aromatic. Compressive loading–unloading simulations were performed with the constructed unit cells at temperatures less than 300 K to observe the local stress, energy, and geometric properties.

During the deformations, the nonbonded interactions and dihedral-angle variations served as important internal-potential parameters that largely contributed to the energy and stress behaviors of the epoxy polymers. In particular, concerning the plastic behaviors under the large deformations, irreversible stress behaviors of the dihedral-angle parts in the monomers of the curing agents were observed in the aromatic-cured epoxy system, whereas reversible dihedral-angle stress behaviors were shown in the aliphatic-cured system. To understand these plastic dihedral-angle stress behaviors, a geometric analysis was carried out for which the RAM values of local sets of atoms were derived. This geometric analysis revealed that the benzene rings showed a rigid low mobility during the deformations, while the polymer chains, which consist of N and carbons, showed a high and flexible mobility. These results suggest that an irreversible dihedral folding must be present near the benzene rings and their linked chains.

Based on the characterized geometric properties, two dihedral-angle types that are composed of the carbons in benzene were selected from the dihedral-energy evolutions at 300 K. To observe the intrinsic dihedral-angle behaviors at the microscopic scale, identical deformation simulations were performed at 1 K with an intensive monitoring of the plastic dihedral-angle transitions of the selected types. Abrupt plastic dihedral-angle transitions were observed near the yielding point of the epoxy polymers and this is physically identical to the classical yielding theory. Consequently, the plastic dihedral-angle transitions that occur near the benzene rings, which are generally observed in aromatic-cured epoxy systems, are important in the elastoplastic-deformation mechanisms of epoxy polymers.

The cyclic loading behaviors of glassy epoxy polymers were investigated as an extended issue on influence of the curing agent on plastic deformation, by MD simulations considering equal molecular structures of the curing agents in **Chapter 3.1**. This chapter aims to understand the contribution of the irreversible torsional angle transitions on the macroscopic ratcheting behaviors of epoxy polymers by taking into account the influence of strain rate. We consider two different epoxy systems consisting of different structures of curing agents (aromatic and aliphatic curing agents), conduct compressive cyclic loading–unloading simulations, and monitor the macroscopic ratcheting behaviors and stiffness variations. In order to correlate macroscopic ratcheting behaviors with molecular conformation change, we separately observe the microscopic transitions of the monomers of epoxy resin and curing agent by deriving structural parameters.

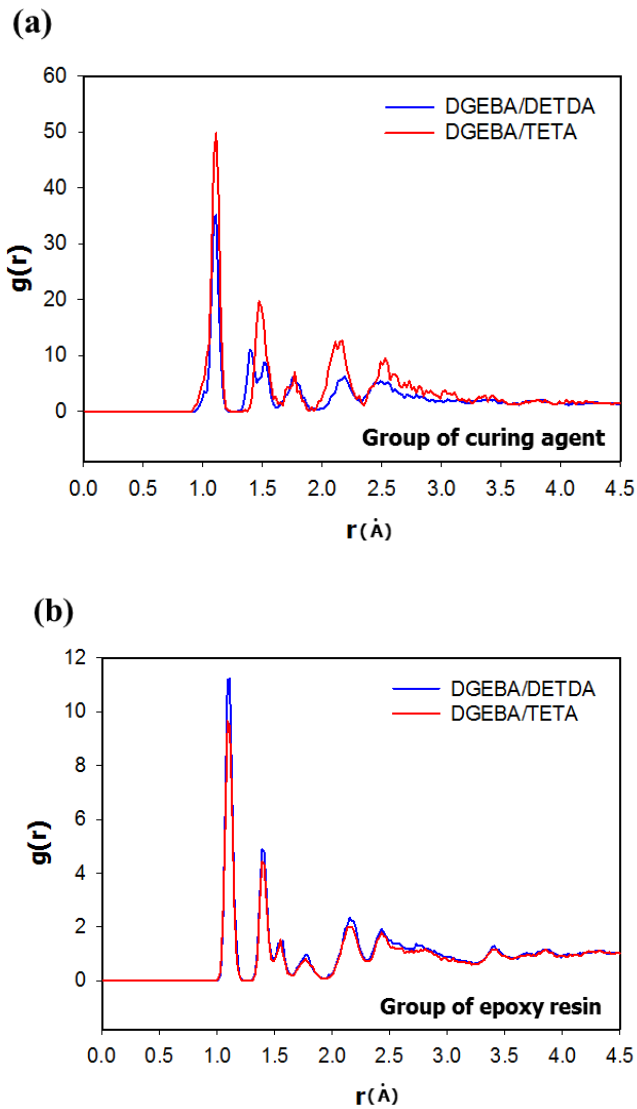

Fig. 3.1. Comparison of the radial distribution function (RDF) of groups of: (a) curing agents and (b) an epoxy resin. The RDF values were derived between all of the atomic pairs in the curing agents and the epoxy resin.

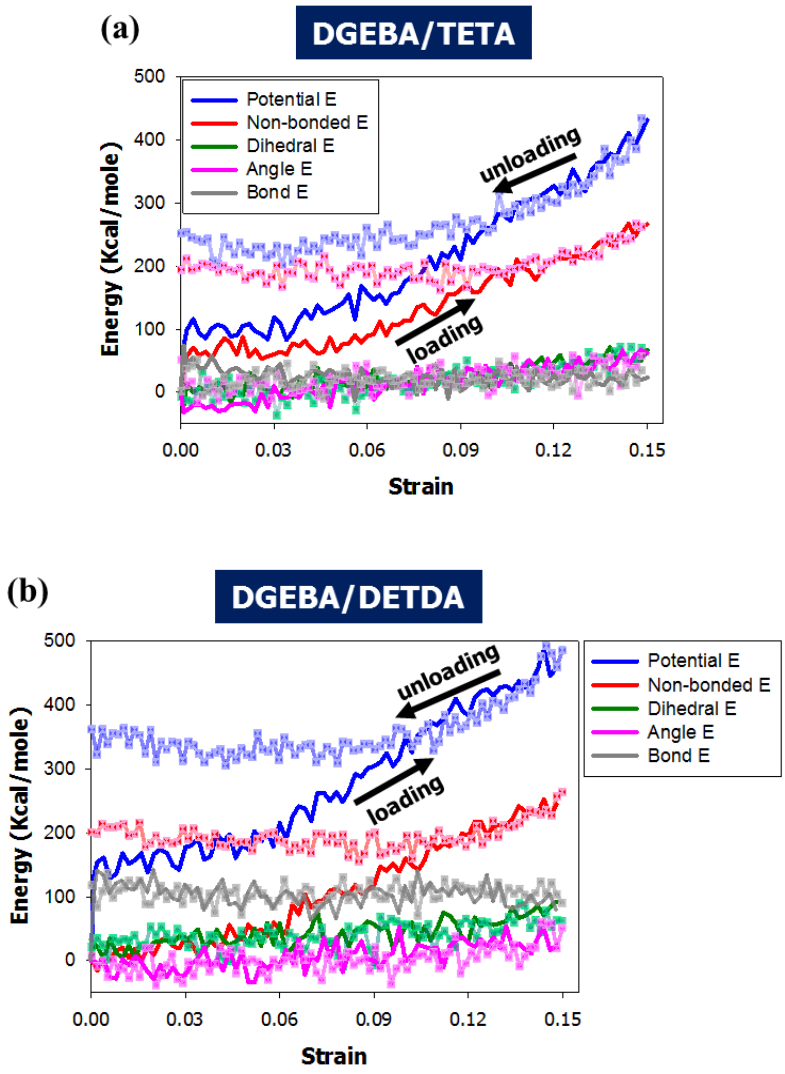

Fig. 3.2. Evolution of the internal-potential-energy components of two epoxy systems: (a) the diglycidyl ether of bisphenol A (DGEBA)/triethylenetetramine (TETA) and the DGEBA/diethyltoluenediamine (DETDA). The deformation energy is accommodated by nonbonded (red), bond (gray), angle (magenta), and dihedral (green) energies, and the blue lines denote their sum. The solid lines and the transparent dotted lines denote the responses to the loading and the unloading, respectively. The improper energy is omitted in the profiles owing to its small contribution.

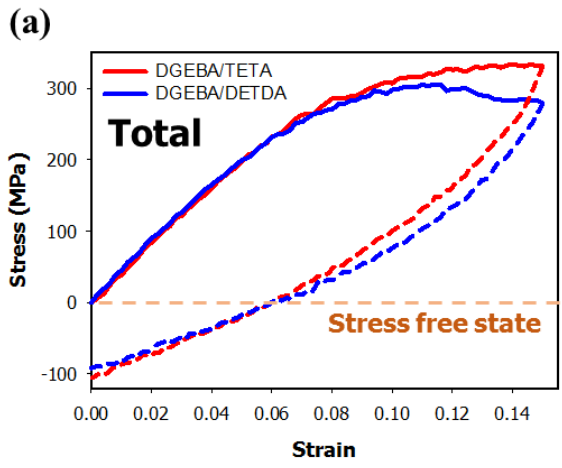
(a)
DGEBA/TETA
DGEBA/DETDA
Total
Stress free state
Stress (MPa)
300
200
100
0
-100
0.00
0.02
0.04
0.06
0.08
0.10
0.12
0.14
Strain

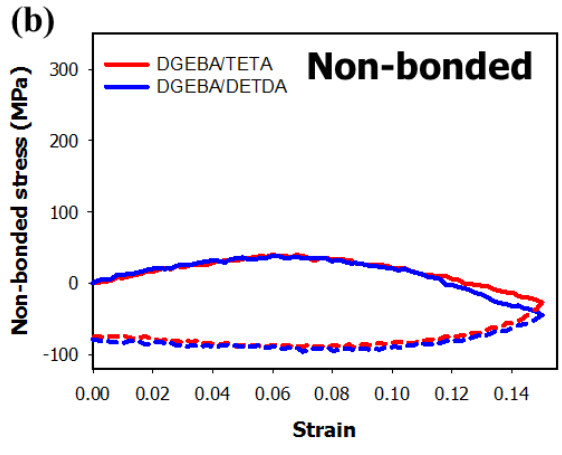
(b)
DGEBA/TETA
DGEBA/DETDA
Non-bonded
Non-bonded stress (MPa)
300
200
100
0
-100
0.00
0.02
0.04
0.06
0.08
0.10
0.12
0.14
Strain

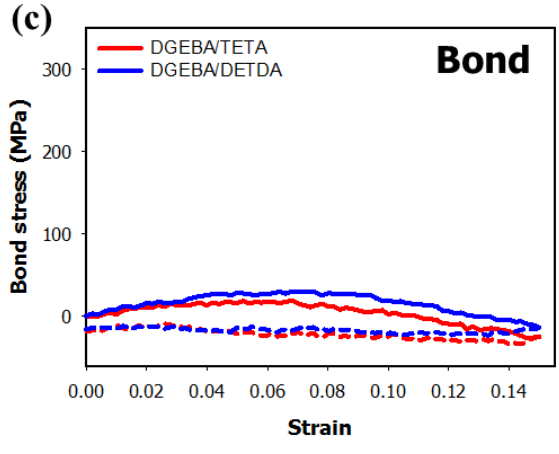
(c)
DGEBA/TETA
DGEBA/DETDA
Bond
Bond stress (MPa)
300
200
100
0
0.00
0.02
0.04
0.06
0.08
0.10
0.12
0.14
Strain

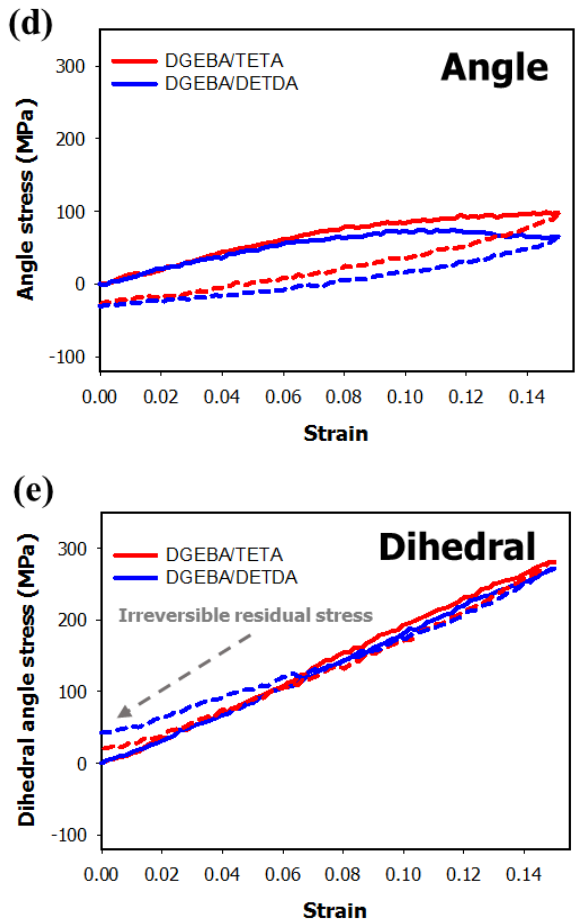

Fig. 3.3. Comparison of the stress–strain responses of the triethylenetetramine (TETA) and diethyltoluenediamine (DETDA)-cured epoxy systems and the contributions of each internal parameter: (a), (b) nonbonded, (c) bond, (d) angle, and (e) dihedral-angle interactions. The red and blue solid lines denote the responses of the TETA- and DETDA-cured epoxy systems, respectively. The solid lines and the short-dash lines denote the responses to the loading and the unloading, respectively. The stress-free state in (a) denotes the moment when the unit cell displayed a stress of zero during the unloading. All of the profiles are the averaged results over three different configurations, five different initial-velocity distributions, and three loading directions.

(a)

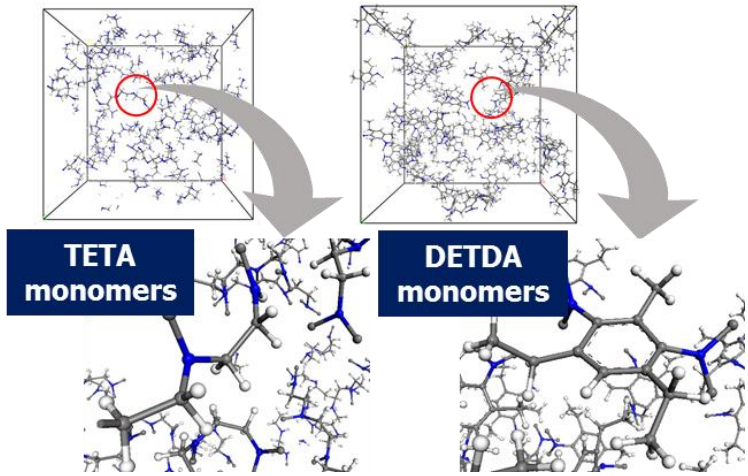
TETA
monomers
DETDA
monomers

(b)

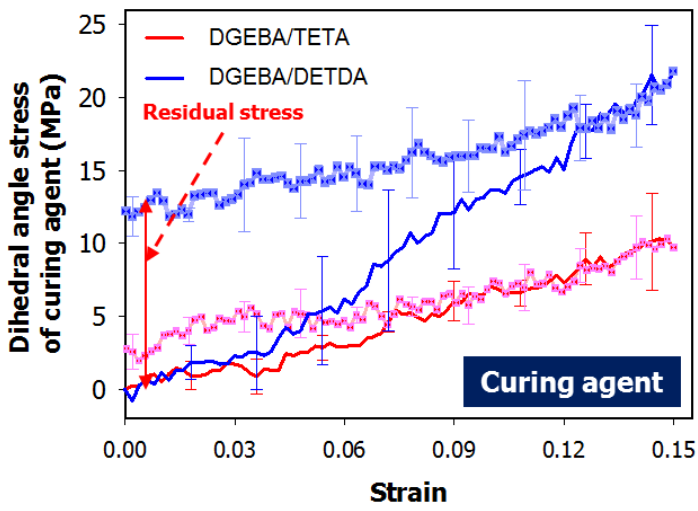
DGEBA/TETA
DGEBA/DETDA
Residual stress
Curing agent
Dihedral angle stress of curing agent (MPa)
Strain
0
5
10
15
20
25
0.00
0.03
0.06
0.09
0.12
0.15

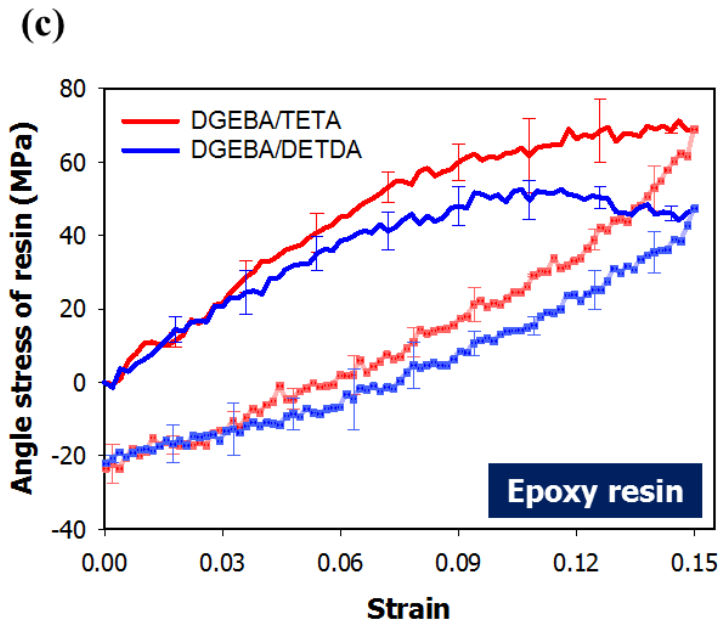

Fig. 3.4. (a) Constructed configurations of the curing-agent monomers of the considered crosslinked epoxy systems, (b) predicted dihedral-angle stress of the curing-agent monomers only, and (c) angle stress of the epoxy-resin monomers only. The error bars were obtained from the standard deviations (SDs) of the profiles of the different initial configurations. The dotted lines in (b) and (c) denote the unloading responses. The dihedral-angle and angle stresses of the curing-agent monomers were calculated by the division of each stress by the total unit-cell volume.

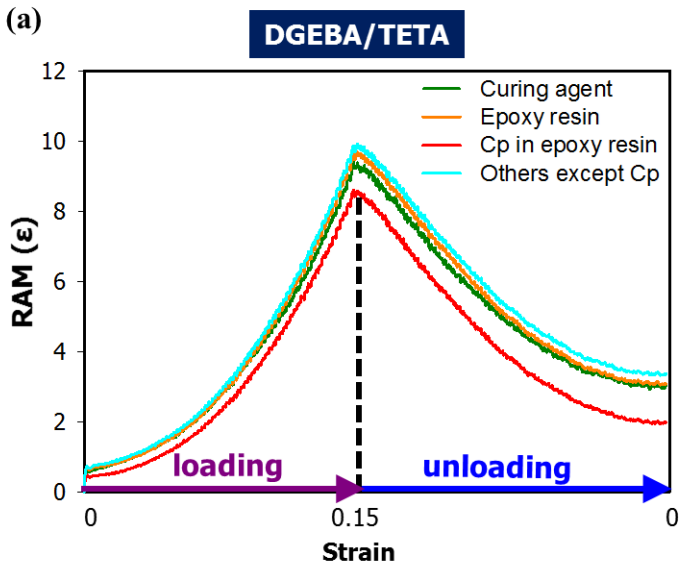
(a)
DGEBA/TETA
Curing agent
Epoxy resin
Cp in epoxy resin
Others except Cp
RAM (ε)
12
10
8
6
4
2
0
loading
unloading
0
0.15
0
Strain

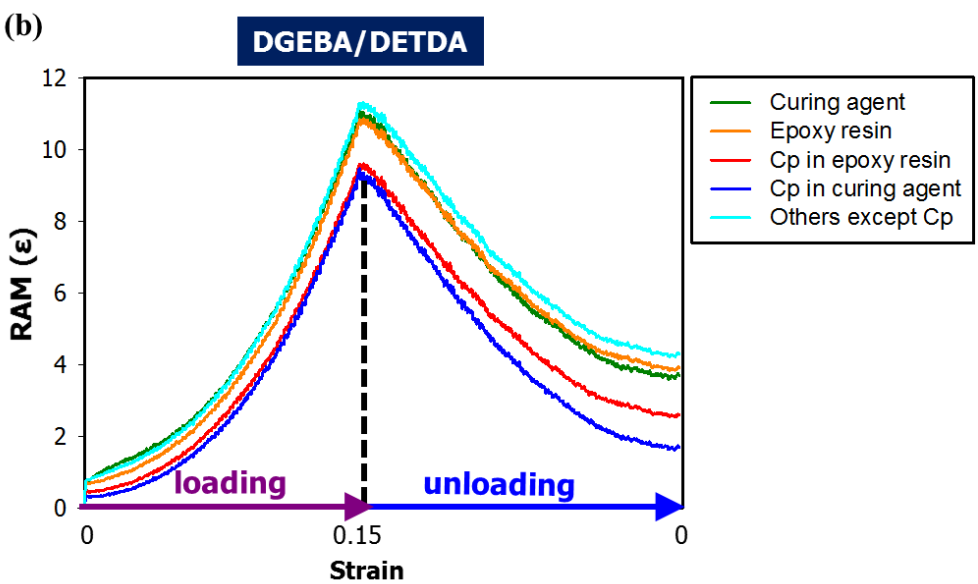
(b)
DGEBA/DETDA
Curing agent
Epoxy resin
Cp in epoxy resin
Cp in curing agent
Others except Cp
RAM (ε)
12
10
8
6
4
2
0
loading
unloading
0
0.15
0
Strain

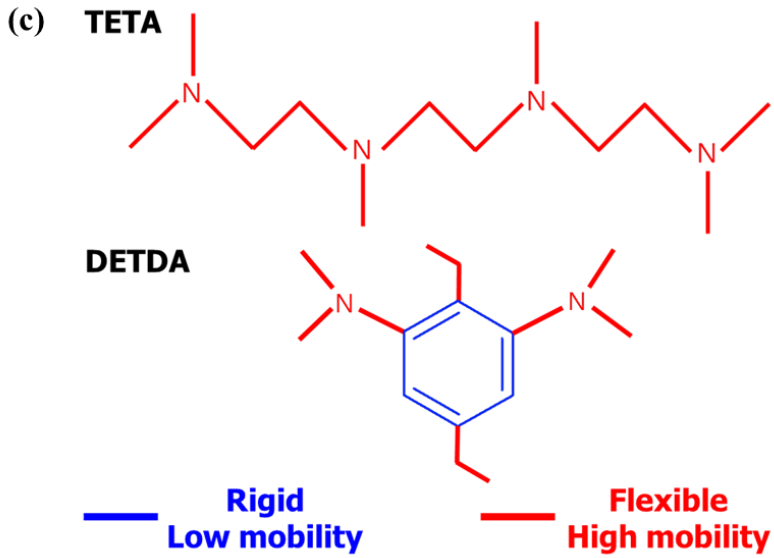

Fig. 3.5. Derived relative atomic mobility (RAM) evolutions with the applied strain in loading–unloading simulations: (a) the diglycidyl ether of bisphenol A (DGEBA)/triethylenetetramine (TETA) and (b) the DGEBA/diethyltoluenediamine (DETDA) systems. The RAM profiles for the atoms of the curing agents, the epoxy resin, and the inherent benzenes were calculated. In (a) and (b), *Cp* denotes the benzene atoms. (c) An illustration of the mobility characteristics of the considered curing agents.

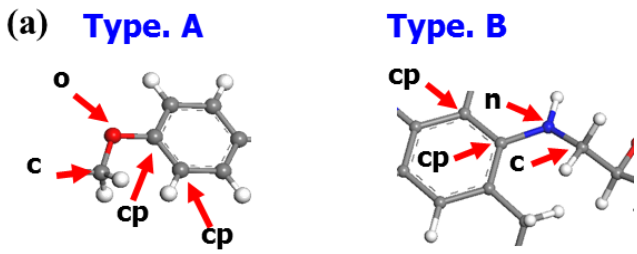

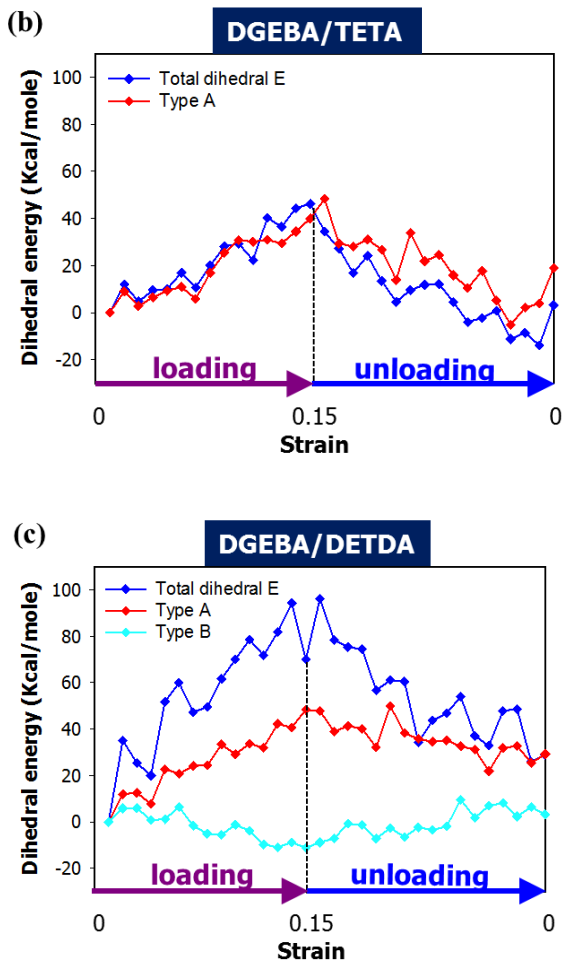

Fig. 3.6. (a) Selected dihedral-angle types, which consist of the atoms of benzene, as well as the flexible chain segments that are linked to the benzene atoms, and their derived dihedral-energy profiles under (b) the diglycidyl ether of bisphenol A (DGEBA)/triethylenetetramine (TETA) and (c) DGEBA/diethyltoluenediamine (DETDA) epoxy systems. *Type A* denotes the dihedral-angle type that is composed of two benzene atoms (represented as the force-field-type *cp*) and their linked oxygen (O) and carbon (C) atoms. *Type B* denotes the dihedral-angle type that is composed of two benzene atoms and their linked nitrogen (N) and C atoms. *Type A* belongs to the epoxy-resin monomers of both systems, and *Type B* belongs to the aromatic curing agent, DETDA.

(a)

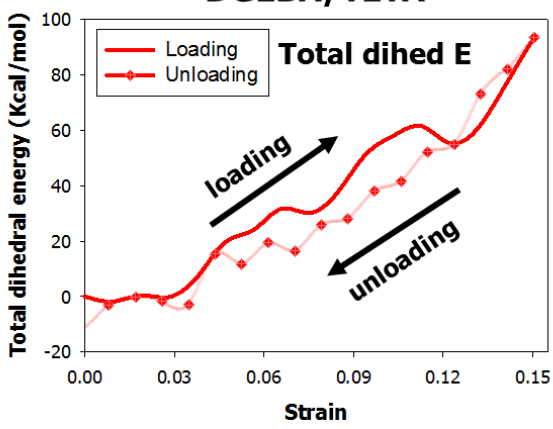
DGEBA/TETA
Loading
Unloading
Total dihed E
loading
unloading
Total dihedral energy (Kcal/mol)
100
80
60
40
20
0
-20
0.00
0.03
0.06
0.09
0.12
0.15
Strain

(b)

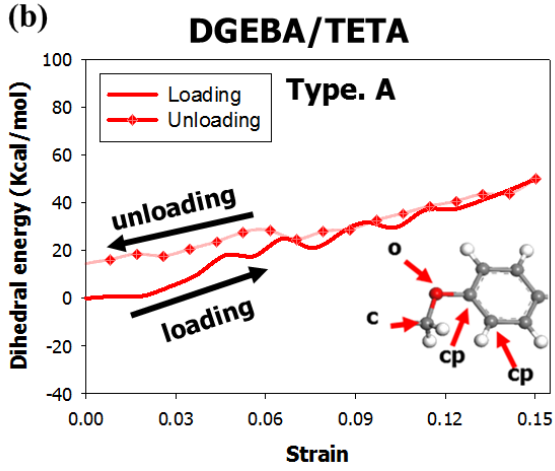
DGEBA/TETA
Loading
Unloading
Type. A
unloading
loading
o
c
cp
cp
Dihedral energy (Kcal/mol)
100
80
60
40
20
0
-20
-40
0.00
0.03
0.06
0.09
0.12
0.15
Strain

(c)

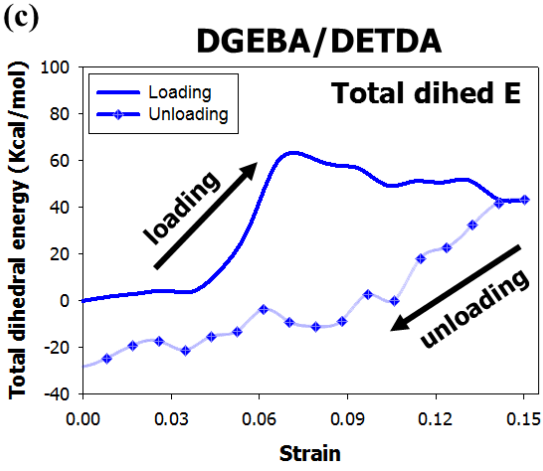
DGEBA/DETDA
Loading
Unloading
Total dihed E
loading
unloading
Total dihedral energy (Kcal/mol)
100
80
60
40
20
0
-20
-40
0.00
0.03
0.06
0.09
0.12
0.15
Strain

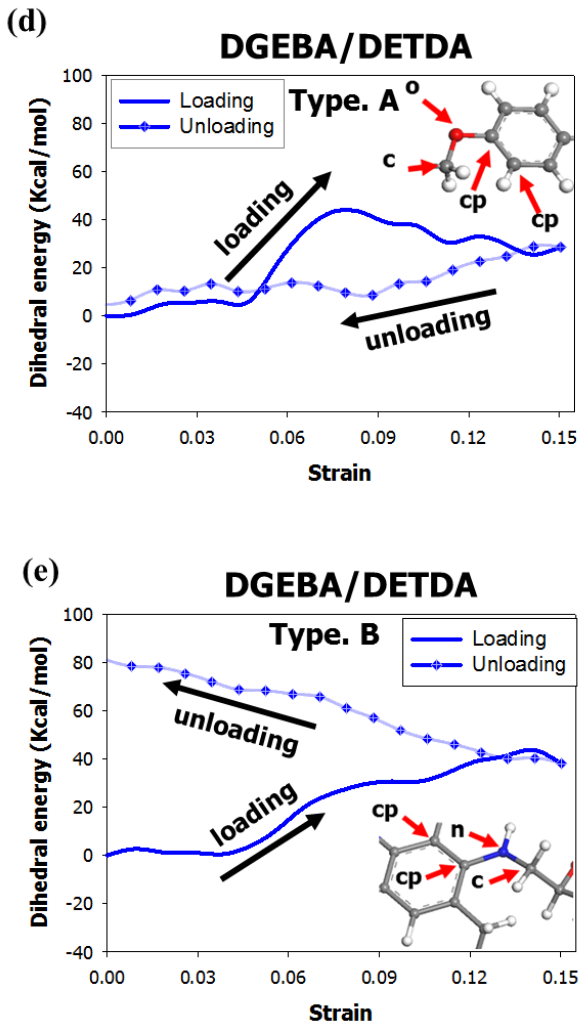

Fig. 3.7. Predicted dihedral-energy evolutions of the diglycidyl ether of the bisphenol A (DGEBA)/triethylenetetramine (TETA) and (c) DGEBA/diethyltoluenediamine (DETDA) systems. The energy evolutions of the total dihedral angles and *Type A* in the DGEBA/TETA system are represented in (a) and (b), respectively. The energy evolutions of the total dihedral angles, *Type A*, and *Type B* are represented in (c), (d), and (e), respectively. In all of the profiles, the solid lines and the dotted lines denote the loading and unloading responses, respectively.

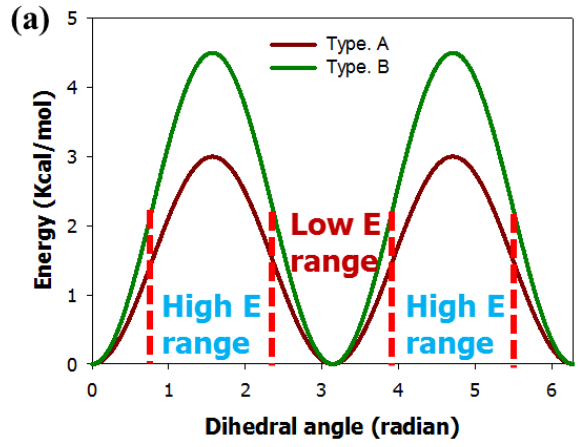
(a)
Type. A
Type. B
Energy (Kcal/mol)
Low E range
High E range
High E range
Dihedral angle (radian)

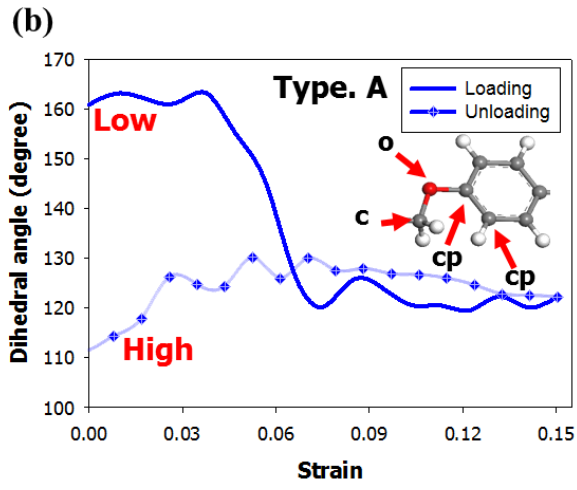
(b)
Type. A
Loading
Unloading
Low
High
o
c
cp
cp
Dihedral angle (degree)
Strain

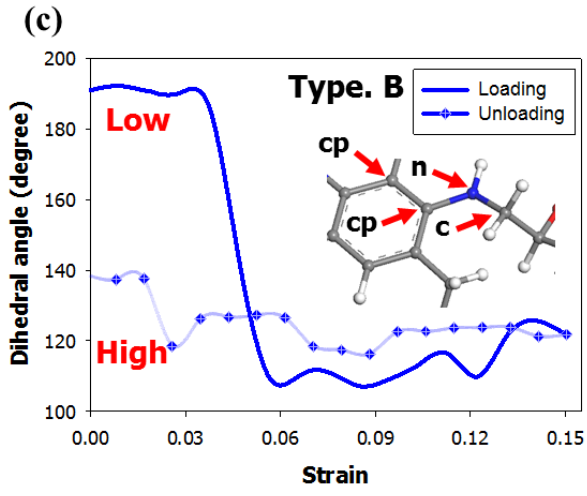
(c)
Type. B
Loading
Unloading
Low
High
cp
n
cp
c
Dihedral angle (degree)
Strain

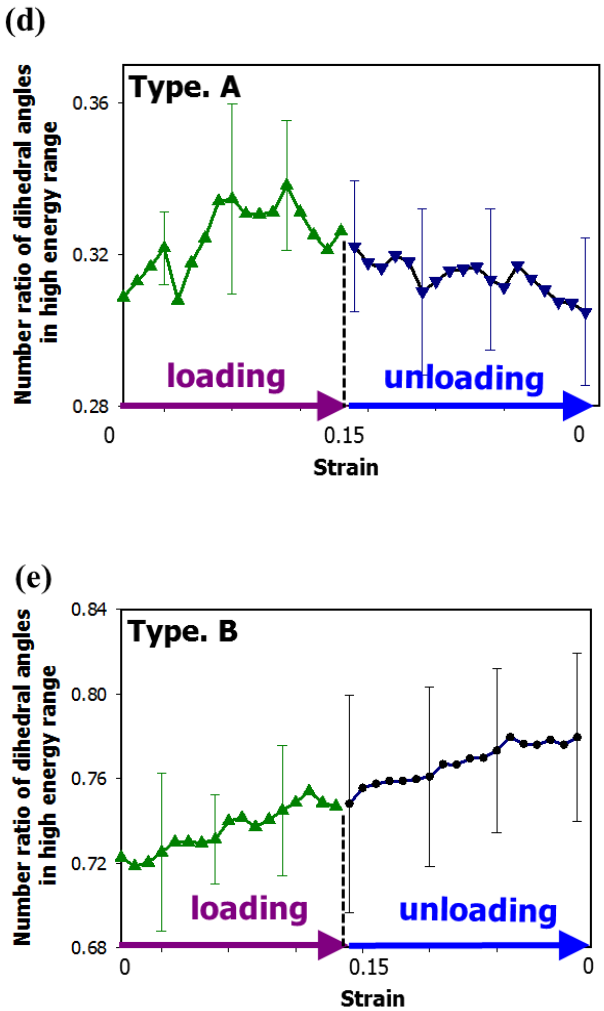

Fig. 3.8 (a) Illustration for the dihedral-angle energy states that correspond to the dihedral-angle variations of *Type A* and *Type B*. The representative dihedral-angle changes for *Type A* and *Type B* are shown in (b) and (c), which is just one case study of the dihedral-angle transitions of *Type A* and *Type B*. The variations of the numerical ratios of the plastic dihedral-angle transitions are shown in (d) and (e). The total of the dihedral angles of *Type A* is 600 and that of *Type B* is 484.

(a)

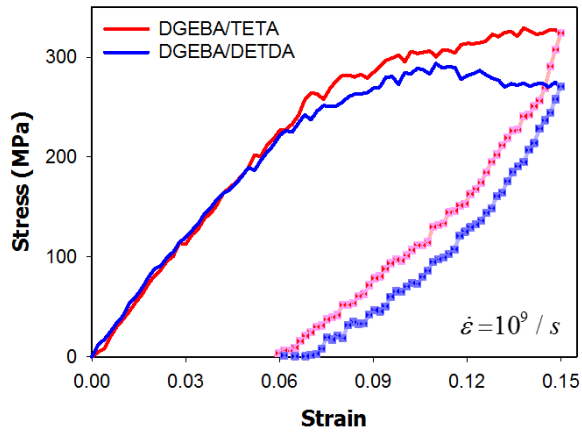
DGEBA/TETA
DGEBA/DETDA
Stress (MPa)
0
100
200
300
0.00
0.03
0.06
0.09
0.12
0.15
Strain
$\dot{\varepsilon} = 10^9 / s$

(b)

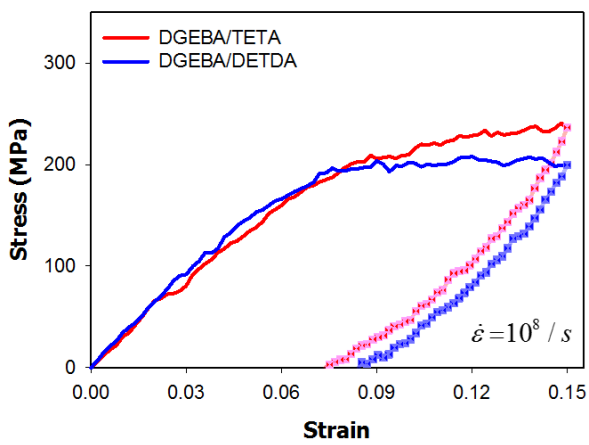
DGEBA/TETA
DGEBA/DETDA
Stress (MPa)
0
100
200
300
0.00
0.03
0.06
0.09
0.12
0.15
Strain
$\dot{\varepsilon} = 10^8 / s$

(c)

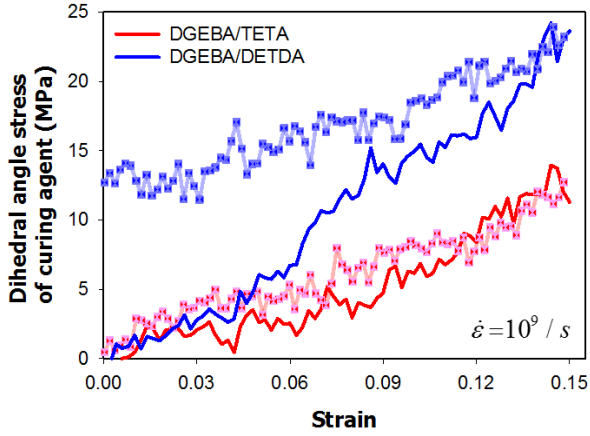
DGEBA/TETA
DGEBA/DETDA
Dihedral angle stress of curing agent (MPa)
0
5
10
15
20
25
0.00
0.03
0.06
0.09
0.12
0.15
Strain
$\dot{\varepsilon} = 10^9 / s$

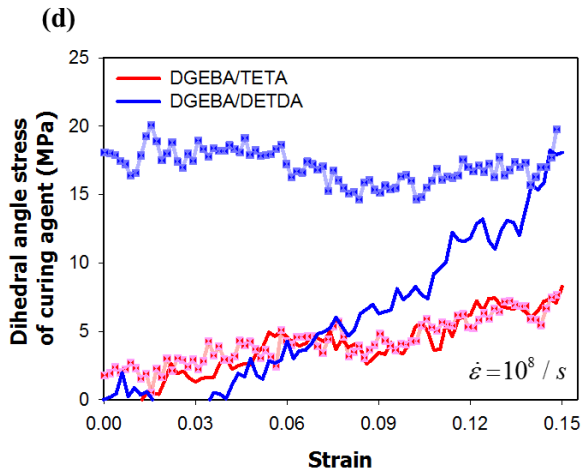

Fig. 3.9. Predicted total stress–strain profiles and contributions of the dihedral-angle stresses of only the curing agents at two different strain-rate conditions: (a) 10^9/s, (b) 10^8/s, (c) 10^9/s, and (d) 10^8/s. The dotted lines in all of the profiles denote the unloading responses. All of the profiles have been averaged over different initial-velocity distributions (five times) and loading directions (x, y, and z axes).

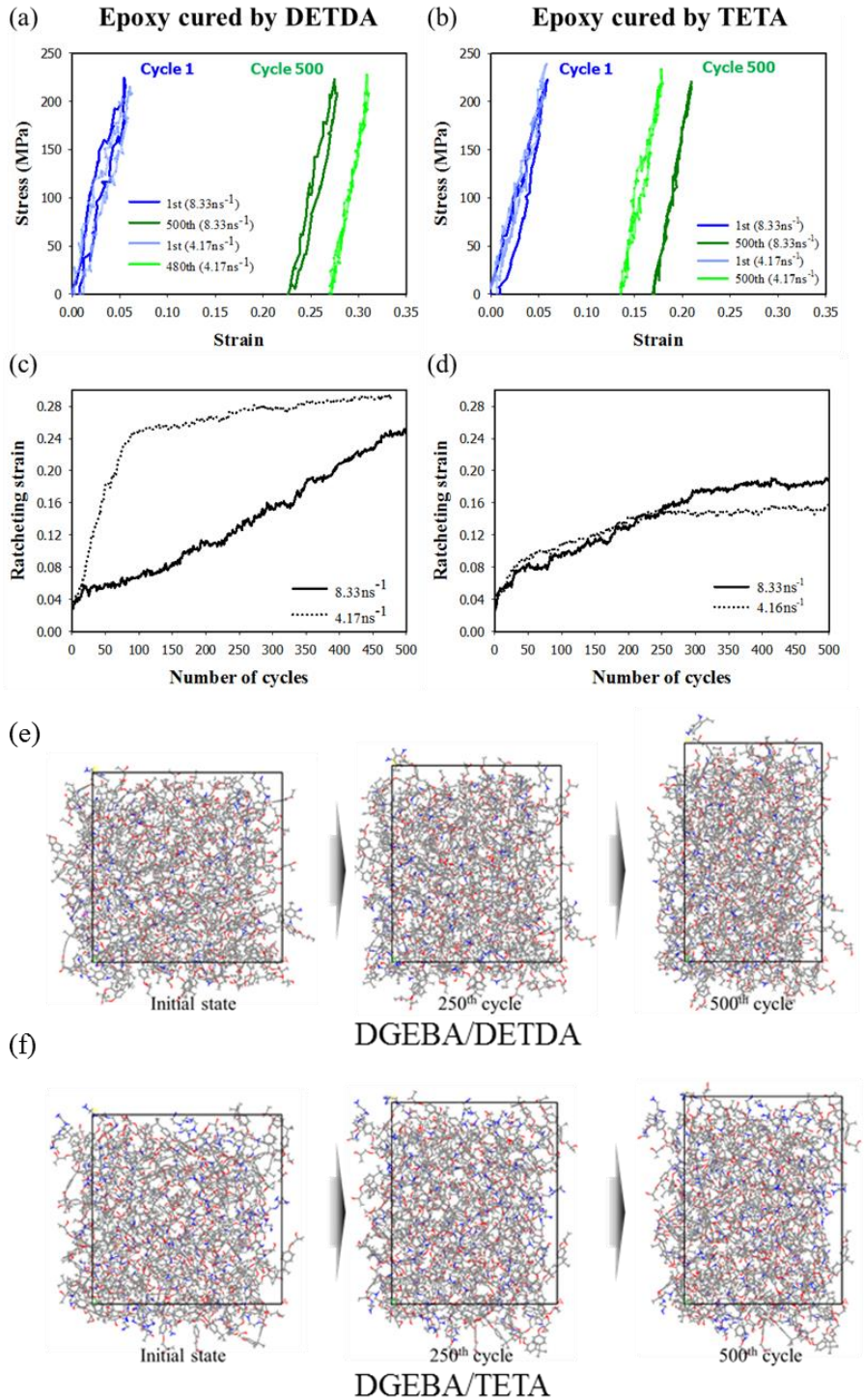

Fig. 3.10. Comparison of the ratcheting behaviors of DGEBA/DETDA and DGEBA/TETA systems under compressive cyclic loading–unloading. Stress–strain profiles under loading

direction with increasing cycles: (a) DGEBA/DETDA, (b) DGEBA/TETA. Corresponding evolutions of the ratcheting strain: (c) DGEBA/DETDA, (d) DGEBA/TETA. Visual illustration for the ratcheting strains of those two epoxies at 8.33 ns^{-1} is presented in (e), (f). Influence of the frequency condition was considered. The profiles at the high frequency (8.33 ns^{-1}) are represented by deep blue and green lines in (a), (b) and by solid line in (c), (d), while those at the low frequency (4.17 ns^{-1}) represented by light blue and green lines in (a), (b) and by dotted line in (c), (d).

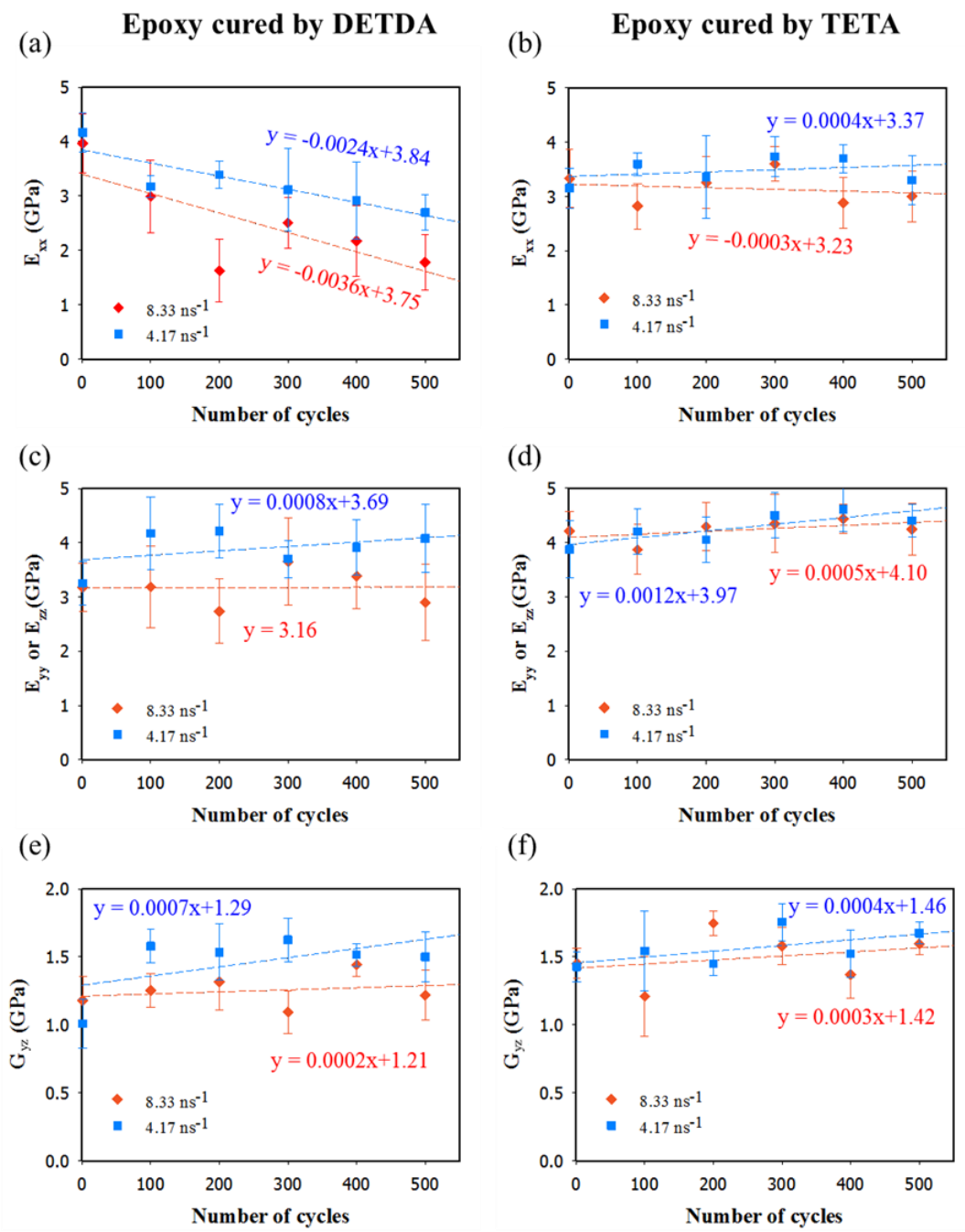

Fig. 3.11. Comparisons of the stiffness components with the number of the cycles. Stiffness evolutions toward the loading direction: (a) DGEBA/DETDA, (b) DGEBA/TETA; stiffness evolutions perpendicular to the loading direction: (c) DGEBA/DETDA, (d) DGEBA/TETA; transverse shear stiffness evolutions: (e) DGEBA/DETDA, (f)

DGEBA/TETA. The results at high frequency and low frequency are represented in all figures by red and blue symbols, respectively.

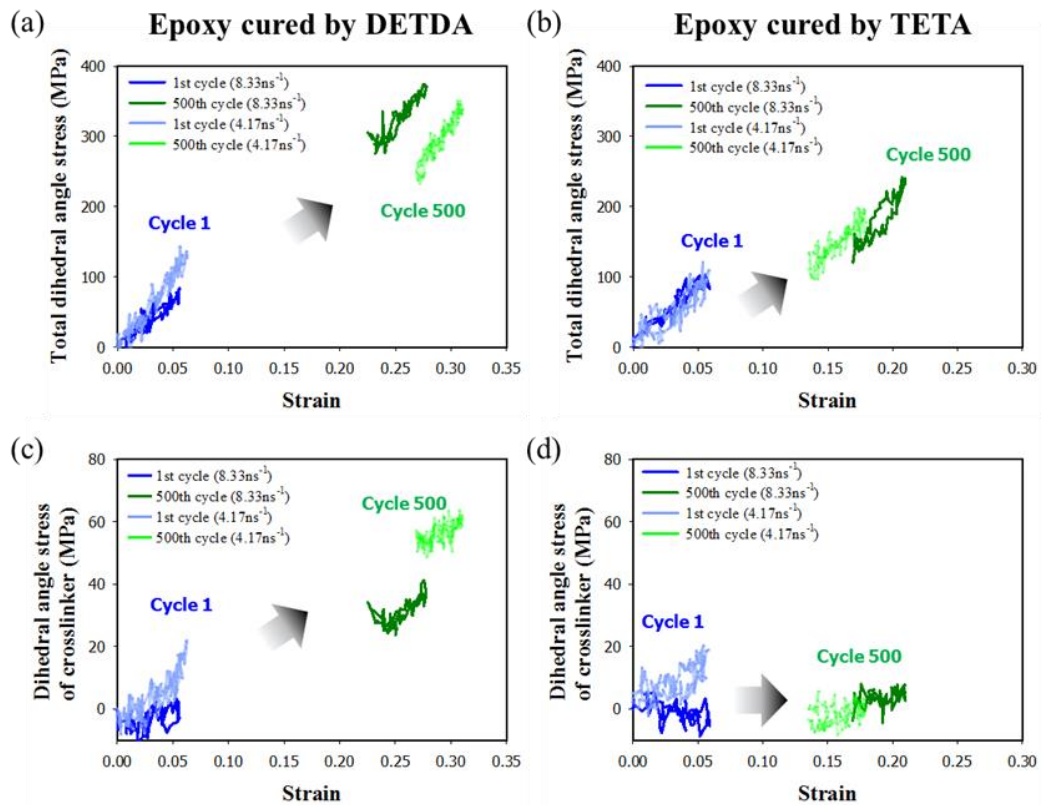

Fig. 3.12. Stress evolutions correlated by the dihedral angle behaviors. (a) Dihedral angle stress of whole epoxy system DGEBA/DETDA with the number of cycles, (b) dihedral angle stress of whole epoxy system DGEBA/TETA with the number of cycles, (c) partial dihedral angle stress of curing agent monomers in DGEBA/DETDA with the number of cycles, and (d) partial dihedral angle stress of curing agent monomers in DGEBA/TETA with the number of cycles.

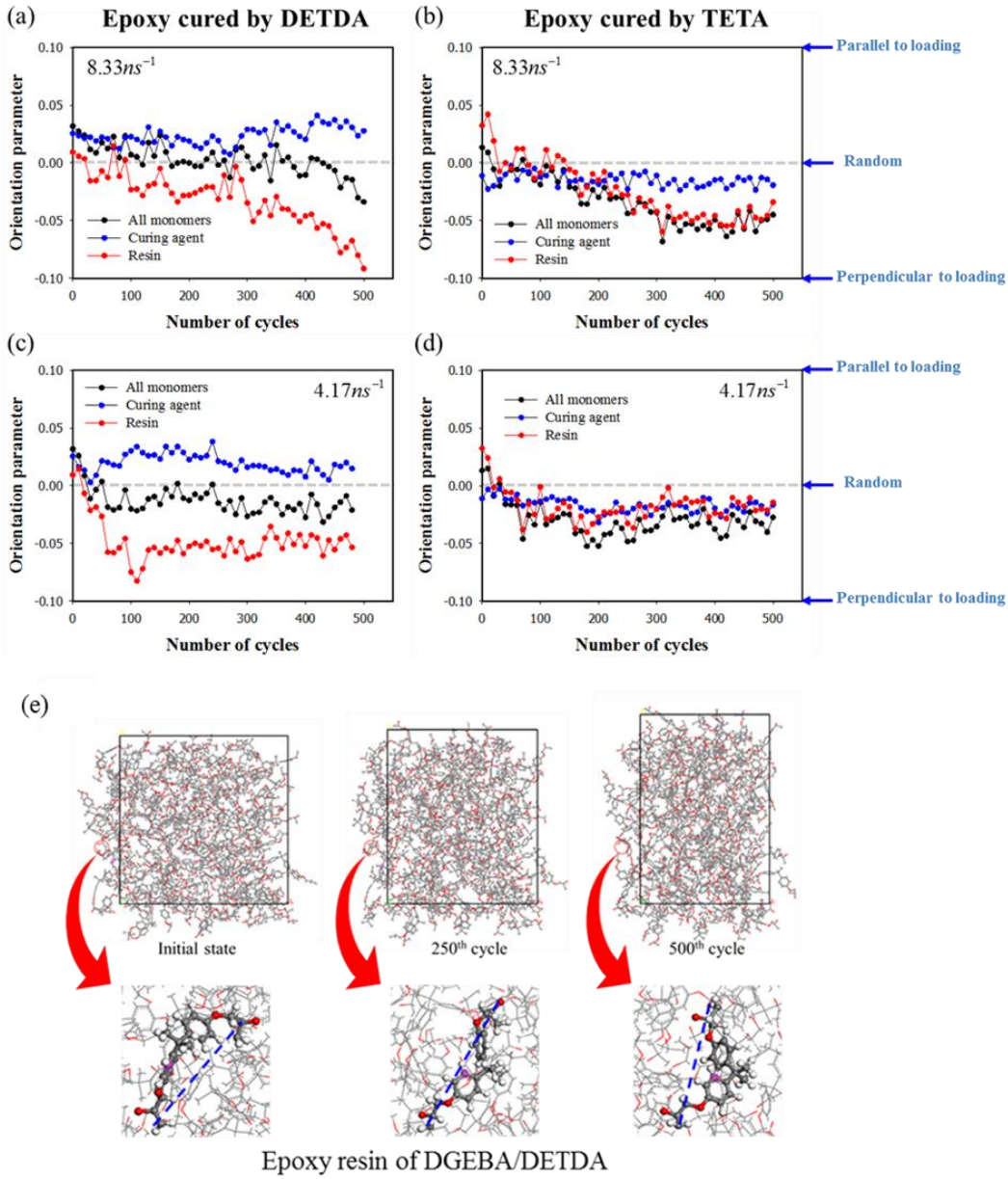

Fig. 3.13. Change of the orientation order parameters of considered epoxy systems at different frequency conditions: (a) DGEBA/DETDA (8.33 ns^{-1}), (b) DGEBA/TETA (8.33 ns^{-1}), (c) DGEBA/DETDA (4.17 ns^{-1}), and (d) DGEBA/TETA (4.17 ns^{-1}). (e) Illustration for representative conformation change of resin monomer in DGEBA/DETDA system.

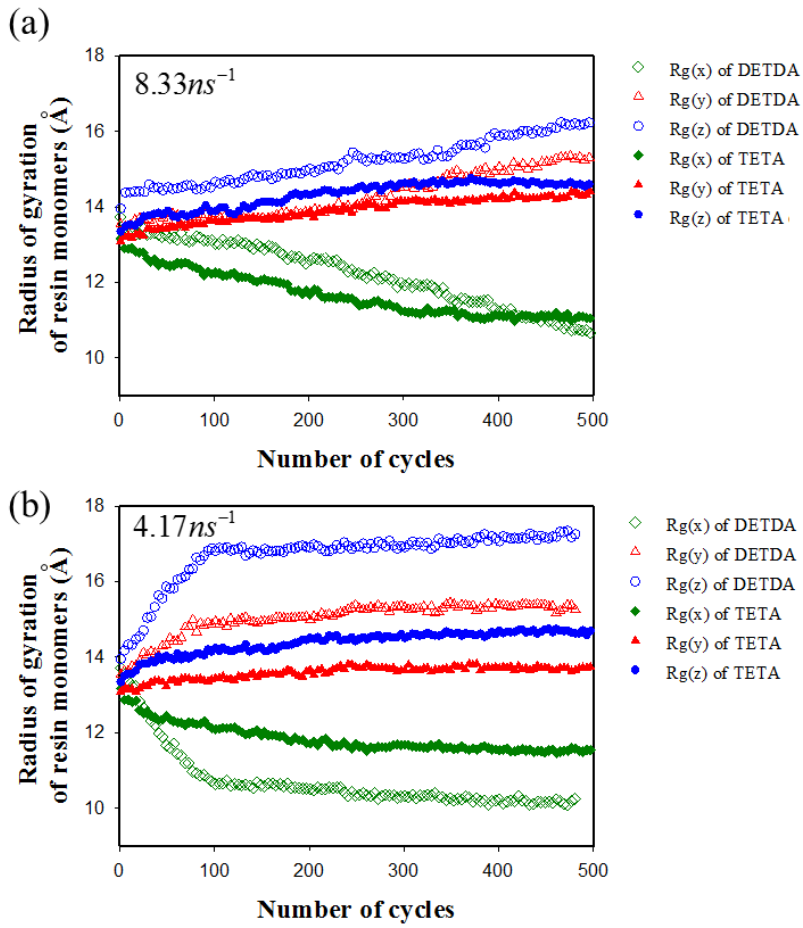

Fig. 3.14. Change of radius of gyrations during the cyclic deformation simulations at (a) high frequency 8.33 ns^{-1} and (b) low frequency 4.17 ns^{-1}. Profiles of DGEBA/DETDA and DGEBA/TETA are denoted by hollow and filled symbols, respectively.

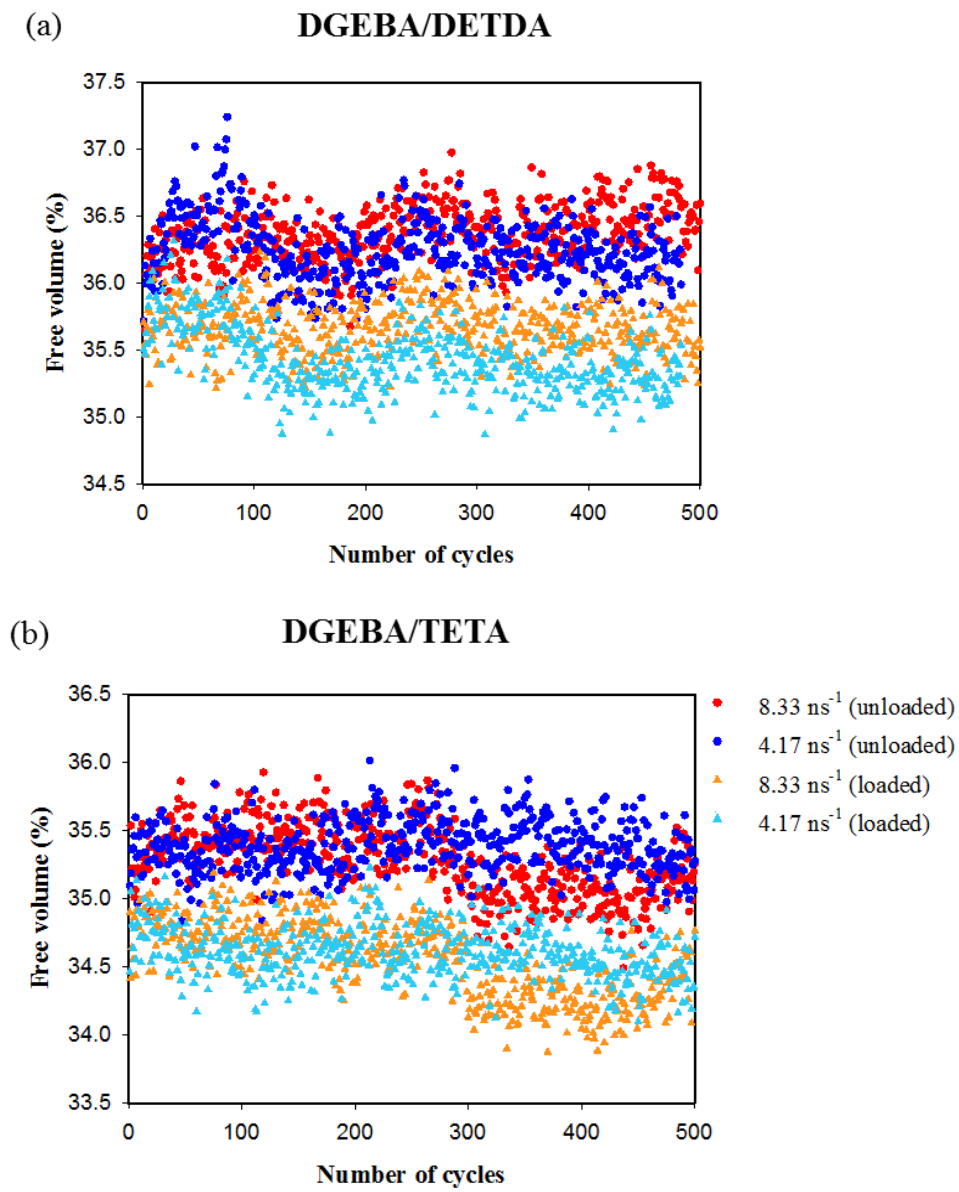

Fig. 3.15. Free volume evolutions of (a) DGEBA/DETDA and (b) DGEBA/TETA at different frequency conditions (8.33 ns^{-1}, 4.17 ns^{-1}). The free volumes measured by fully loaded and unloaded states are simultaneously represented at the evolutions of both epoxies.

4. Methods to overcome timescale limitations of classical molecular dynamics

In this chapter, timescale extension of the classical MD simulations was considered via two approaches; the master plot for the yield stress was predicted by using the equivalence between time and temperature in deformation behaviors of polymers in **Chapter 4.1**; the Argon theory and Cooperative model were adopted to estimate quasi–static yield stress and construct the master plot for the yields in **Chapter 4.2**.

4.1. Prediction of quasi–static constitutive laws by temperature–accelerated method

4.1.1. Theoretical background

To account for the quasi-static mechanical behavior, which is not available in classical MD simulations, we also utilize the concept of temperature-accelerated dynamics (TAD). According to Eyring's model and extended models[47,49], it is revealed that negative temperature dependency and positive strain rate dependency are directly associated with the yielding of glassy polymers. Therefore, if a proper quantitative characterization is enabled between the strain rate and yield strength, and between the temperature and yield strength, the limitation in enlarging the time scale required to consider the slow strain rate within the available Eyring plot can be overcome. The TAD model enables the acceleration

of the transition from one state to other states by incorporating thermal activation energy to promote the transition. In combination with transition state theory and the concept of TAD, the inherent time scale limitation of MD simulations can be overcome by elevating the simulation temperature.

As a representative model for describing the polymer yield on the basis of transition state theory, the Ree-Eyring model[47] (modified from the Eyring equation for yield stress) was suggested as follows:

$$\frac{\sigma_y}{T} = A_\alpha \cdot \left(\ln(2C_\alpha \dot{\varepsilon}) + \frac{Q_\alpha}{kT} \right) + A_\beta \cdot \sinh^{-1}\left(C_\beta \dot{\varepsilon} \exp\left\{ \frac{Q_\beta}{kT} \right\} \right), \tag{4.1}$$

where σ_y, T, k, and $\dot{\varepsilon}$ are the yield stress, temperature, Boltzmann constant, and strain rate, respectively. $Q_i (\mathrm{i} = \alpha, \beta)$ is the activation energy corresponding to the two rate processes of α and β, and A_i and C_i are activation constants. In this model, the strain rate and temperature dependencies on the yield stress are described quantitatively by the activation parameters. While Eyring's initial equation (which fails to describe the yield behavior across a broad range of temperatures and strain rates) considered one rate process to predict the yield stress, the Ree-Eyring model can accurately predict the nonlinear relationship between $\frac{\sigma_y}{T}$ and $\log \dot{\varepsilon}$. To accomplish this within a broad temperature range, the yield stress is defined in Eq. (4.1) by introducing the additional nonlinear strain rate-dependent process β via an arc-hyperbolic sine function.

In addition, Bauwens-Crowet et al.[18] introduced shifting factors (S_x and S_y) on the Ree-Eyring model following the linearized Arrhenius equation:

$$\left\{\begin{array}{l}\Delta \log \dot{\varepsilon} = S_x\left(\dfrac{1}{T}-\dfrac{1}{T_{ref}}\right)\\ \Delta \dfrac{\sigma_y}{T} = S_y\left(\dfrac{1}{T}-\dfrac{1}{T_{ref}}\right)\end{array}\right\}, \tag{4.2}$$

where T_{ref} is the reference temperature used to determine the shifting factor, which in turn is used to determine the variation in strain rate and yield strength at temperature *T*. To utilize Eq. (4.2) in predicting the strain rate-yield strength relationship of glassy polymers at various temperatures, one master curve is obtained from experimental tension or compression tests at the reference temperature. By measuring the activation energy from the constructed curve, the shifting factors can be readily determined[18,19]. Then, according to the values of the two shifting factors and their ratio, the curve of the reduced yield stress $\frac{\sigma_y}{T}$ versus $\log \dot{\varepsilon}$ is extrapolated from the master curve[14], as shown in Fig. 4.1. In our simulation study, instead of measuring the activation energy, we propose a novel approach, which uses the slope of a reduced yield profile to determine the shift factor.

4.1.2. Investigation on deformation characteristics and physical properties

- **Glass transition temperature**

The main idea of **Chapter 4.1** is to accelerate the transition event by elevating the temperature conditions in deriving the desired quasi-static yield stresses. However, it

should be noted that the change in material properties caused by the phase transition should not occur within the elevated temperature range. Thus, in this chapter, the glass transition temperature (T_g) of the epoxy system is estimated from the density-temperature relationship by employing the same cooling-down method used in our previous study[11,37]. In particular, after the structural relaxation at 300 K and 1 atm, the unit cell is equilibrated at 600 K to reach the rubbery state under *NVT* and *NPT* ensemble simulations for 2 ns and 4 ns, respectively. Then, with a constant cooling down rate of 0.04 K/ps, the temperature of the unit cell is decreased to 100 K while monitoring the change of specific volume with respect to the variation of temperature. The glass transition temperature is predicted from the intersection point of the two linearly fitted lines of the specific volume-temperature profile, as shown in Fig. 4.2. By extending the two linear fitted lines for the glassy and rubbery states, the glass transition region can be determined from the intersection point located in the temperature range between 480 K and 500 K, which is in a good agreement with the experimental results[86]. Considering the transition region, the available temperature for the glassy state is set to 450 K in this chapter.

- **Stress-strain responses for glassy state under different strain rates and temperatures**

Stress-strain profiles under different strain rates (10^{10}/s, 10^9/s, and 10^8/s) and temperatures (300 K, 350 K, 400 K, and 450 K) were derived from MD simulations, as shown in Figs. 4.3(a–c). All the stress-strain curves show a similar material response in

which stress increases linearly in the elastic range with increasing strain, and the increasing rate of stress is noticeably decreased. The studied material exhibits the elasto-plastic behavior without distinct strain softening, which differs from that of non-crosslinked thermoplastic polymers. In general, in the stress-strain response of the thermoplastic sample, distinct softening and hardening regions have been observed in other MD studies[26]. This difference can be attributed to the constrained chain mobility of the thermoset polymer generated by the crosslinked network, which hinders the softening of the polymer chain after the yield point.

As expected, the temperature and strain rate dependencies on the overall stress-strain profiles are well showcased in all profiles. As shown in Figs. 4.3(a–c), the overall stress decreases with increasing temperature and decreasing strain rate, which agrees with previous studies[13–15,17–19,21,22,39–41]. This result implies an important physical insight in MD simulations; namely, that both temperature and strain rate have an equivalent effect on the mechanical response of an amorphous polymer (from the viscoelastic point of view). In other words, the MD results certify that as a result of the equivalence of these two physical variables, the time scale (which is difficult to increase up to the quasi-static level in simulations) can be adjusted by changing the temperature; this agrees well with the experimental literature.

The exchange of these two physical variables can be understood from the perspective of the molecular movement of polymer chains. The elevated kinetic energy (which results from the increase of temperature) induces more vigorous molecular

movement, which leads to the rapid structural rearrangement of polymer segments during the deformation. Similarly, as the strain rate decreases, polymer chains have more sufficient relaxation time to transform their internal structure from one state to another equilibrium state in the potential energy surface, leading to the same rearrangement. This crucially implies a pathway to overcome the limitation of MD simulations regarding their relatively short time scale (compared to the experimental counterpart). In other words, MD simulations with an elevated temperature generate a higher thermal activation energy that can compensate for the insufficient relaxation time of polymer chains caused by the inherently high strain rates.

- **Yield criterion**

The distinct criterion for determining the yield point must be established to obtain the clear tendency of yield stress change from MD simulations. The yield of an amorphous polymer occurs when the polymer chain segments start to plastically flow to overcome the energy barrier for the local chains. Once the yield point is reached, various internal parameters such as dihedral angle, free volume, and angle are changed irreversibly as reported by previous studies[26,27]. Moreover, the deformation behavior of post-yield range of epoxy polymer can be dominated by the microcracking due to brittleness of epoxy networks. Due to the complex contribution of internal parameters, amorphous thermoset polymers are generally characterized by an unclear yield point (in contrast to crystalline materials)[22].

Thus, in order to determine the yield stress from the stress-strain curves of glassy polymers, we fitted the stress-strain data with a polynomial curve using a least-squares fit. Raw stress-strain data obtained from MD simulations (solid squares) are presented in Fig. 4.4 along with the fitted polynomial curve (purple solid line). Then, the fitted polynomial curve was fitted again by employing the linear elasto-plastic model where the stress behavior is described as two bilinear lines (elastic and linear plastic region). From the fitted linear elasto-plastic model, the Young's modulus, yield stress, and hardening parameters were determined as shown in Fig. 4.4. In the evaluation stage, we defined the residue of the stress as follows:

$$r(\sigma_Y, \varepsilon_Y, K) = \sigma - f^{E-P}(\sigma_Y, \varepsilon_Y, K), \qquad \text{Minimize } |r| \quad , \tag{4.3}$$

where f^{E-P} and σ are the linear elasto-plastic function and the stress of the epoxy in the polynomial fitted curve, respectively, and K is the hardening parameter. The yield stresses for each temperature and strain rate are provided in Table 4.1.

4.1.3. Scheme for prediction of quasi–static solutions

- **Nonlinear characteristics of yield and their utilization with the MD result**

Similar to the stress-strain responses, the derived yield stress values given in Fig. 4.5(a) demonstrate the temperature and strain rate-dependent characteristics; the yield stress linearly decreases with decreasing logarithmic strain rate and increasing temperature for the conditions considered in this work. This linearly decaying trend of yield stress in

the computational environment corresponding to the variation of temperature was previously observed by Vu-Bac et al.[23] using MD simulations. More specifically, they obtained the yield stress of epoxy for the theoretical value of strain rate of 5×10^{9}/s via MD simulations by employing the Argon theory, which was based on the assumption that the linearly decreasing trend of the yield stress with respect to temperature at high strain rates can be equally observed at the quasi-static conditions.

However, it should be noted that such linearity in the temperature-yield strength relationship cannot be guaranteed experimentally at extremely low temperatures where the molecular movements are severely frozen. This fact leads to the nonlinear variation of the yield stress with respect to the broad range of temperatures and strain rates. Bauwens-Crowet et al.[19] focused on this phenomenon and developed an experimental model for the yield of amorphous polymers by extending Eyring's model. In order to illustrate the yielding behavior at extremely low temperatures (from −150 ºC to 50 ºC in work of Bauwens-Crowet et al.[19]), it was assumed that the yield at this condition involves two independent rate processes, which have already been introduced in Eq. (4.2). In line with this approach, a cooperative model modified from Eyring`s equation was also used to describe the yield stress-temperature relation of glassy polymers at a wide range of temperatures by Fortherigham and Cherry[49]. In their results, the same tendency was observed in which the yield stress nonlinearly varies over the broad range of strain rates and temperatures. This provides an important physical insight: namely, that the yield stress should vary nonlinearly over the broad range of strain rates; likewise, the yield stress varies

nonlinearly with the variation of temperature. Therefore, nonlinearly varying yield stress according to the change of strain rate and temperature is obvious in the deformation kinetics of amorphous polymers, and also provides the logical basis for the TAD using a changeable shifting factor, which is proposed in this study for the first time.

To take into account the nonlinear characteristics of yield stress according to the temperature and strain rate on the environment of MD simulations, the profile for the reduced yield stress $\frac{\sigma_y}{T}$ versus $\log \dot{\varepsilon}$ is plotted in Fig. 4.5(b) from the same data of Fig. 4.5(a). The slope of the reduced yield stress is also derived over the considered temperature conditions of this study in Table 4.1. The slope decreases with the increasing temperature from 0.128 at 300 K to 0.064 at 450 K. This decreasing slope of Fig. 4.5(b) is natural considering the abovementioned linear trend depicted in Fig. 4.5(a), since each slope is determined by the inverse of the given temperature.

Considering the abovementioned nonlinear varying trend of yield stress with strain rate, which is represented in the Eyring plot (Fig. 4.1), the slope of the reduced yield stress will steadily decrease as the strain rate decreases to the quasi-static level. Under the quasi-static rate conditions, the change of slope with respect to temperature is smaller than that of the high-rate conditions[18,19], since the sufficient structural relaxation time for inducing the viscous flow of polymer segments is guaranteed to initiate the yield, thereby resulting in low stress. Thus, the slope of reduced yield under quasi-static conditions must be lower than that under computational rate conditions. Furthermore, this trend can be

confirmed by comparing the experimental results[18,19] with Fig. 4.5(b).

The obtained data imply that the slope of the reduced yield measured at the quasi-static conditions can be reached at high simulated strain rates, if the temperature is sufficiently elevated using the variation trend of the reduced yield with respect to temperature. In other words, the slope of the reduced yield (which is decreased by elevating temperature in MD simulations) is comparable with that obtained under the quasi-static conditions. In this chapter, owing to the equivalence between temperature and strain rate, changeable shift factors are obtained from the MD simulations by taking into account the nonlinear characteristics of yield stress. Subsequently, quasi-static yield can be estimated from the calculated shift factors.

- **Convergence of yield stress in lower strain rate range**

To robustly predict quasi-static yield stress by constructing Eyring plot, the convergence of the reduced yield stress – strain rate plot should be guaranteed when the yield points at the high temperature range shift toward the lower strain rate. Accordingly, the slope of yield points at 300 K and higher strain rate range (higher than 10^8/s) should be sufficiently decreased to the level at the experimentally lower strain rate range that is possibly determined from the yield points of 450 K. To confirm the convergence at 450 K, therefore, yield stresses were further examined with the various ranges of strain rates as given in Fig. 4.6. As mentioned in the previous section, the nonlinear relation between the yield stress and logarithmic strain rate is observed. Moreover, as far as the slope of yield

stress with logarithmic strain rate is concerned, the data points can be separated into three groups (blue, green, and red points in Fig. 4.6). Unlike with lower temperature conditions, in a higher temperature range, the yield stresses of 450 K clearly show a relatively faster convergence with decreasing strain rate due to the contribution of temperature on the relaxation of polymer chains.

Thus, if the blue points in Fig. 4.6 (with a strain rate of computational scale at a higher temperature) are properly shifted toward the lower strain rate region that corresponds to an experimental strain rate range at the room temperature, the quasi-static yield stress can be reasonably obtained.

- **Shifting method and quasi-static (low strain rate) solution**

In this section, a specific methodology for predicting quasi-static yield stress from high strain rate conditions is proposed for the first time by carefully considering the viscoelastic nature of amorphous polymers. The limitation of MD simulations regarding the time scale can be overcome by elevating the temperature based on the similarity of the slope of reduced yield between the quasi-static conditions and high-rate, elevated-temperature conditions. To take into account the nonlinear varying of yield stress with temperature and strain rate, the shifting method based on the ratio of changeable shifting factors are introduced in this chapter. This method is based on the sequential shifting processes using the data sets in the elevated temperature conditions with the iterative algorithm to achieve the appropriate shifted positions of the given data sets.

The proposed method considers the involvement of multiple rate processes in the yield behavior of amorphous polymers, which means that the slope of the profile for the reduced yield stress versus logarithmic strain rate is constantly decreased with the decreasing strain rate in the MD simulations. Other researcher also observed the multiple rate processes regarding the polymer relaxation using the MD simulations[40]; Capaldi F. M. et al. carried out compressive tests using united atom model and observed nonlinear yield behavior with different temperatures. They indicated that the nonlinear feature observed in MD simulations is a clear evidence of multiple rate processes in polymer yield behavior. Based on the assumption that the yield behavior of amorphous polymers under the wide range of strain rate is significantly involved with the multiple rate processes, the changeable shifting factor concept are introduced in the present work. Herein, to take into account the multiple rate processes in polymer yielding behavior, the correlation among yield stress, strain rate, and temperature is described as an exponentially decaying function:

$$\frac{\sigma_y}{T} = a \cdot \exp(b \cdot \log \dot{\varepsilon}) + c \cdot \log \dot{\varepsilon} + d \,, \tag{4.4}$$

where, *a*, *b*, *c*, and *d* are fitting coefficients. Compared to the Ree-Eyring model in Eq . (4.1), the present model is composed of exponential terms instead of using arc hyperbolic sine function to consider the nonlinear nature of multiple rate processes. The linear term in Eq. (4.4) is to illustrate the extinction of nonlinearity in yield stress for the extremely low strain rate condition, which is similar to the Ree-Eyring model.

Detailed description to predict quasi-static yield using the iterative regime is shown in Fig. 4.7. The present acceleration method is based on the sequential shifting concept; the data points at a higher temperature can be shifted sequentially to a lower strain rate range using the shifting factor ratio calculated from the existing fitted curve (shifting factors are derived by Eq. (4.2)). In the shifting procedure, the selection of data points require a profound consideration; the proper data points showing the linearly decaying trend need to be determined which represent the same rate processes.

Herein, once the data points set is shifted to the existing fitting curve, the constant slope trend should be maintained to represent the same rate processes. The data points in the shifted condition were derived by minimizing the deviation between the shifted point at the highest strain rate and existing fitting curve using the least square method.

However, the accuracy would not be guaranteed in the first shifted points since the existing fitting curve may not be able to properly predict the yield stress of the lower strain rate range. Thus, the shifting of data sets should be performed iteratively with an appropriate modification of the prediction curve. In the present study, the existing fitting curve was iteratively updated using the shifted data sets to describe the nature of rate process of considered temperature condition. Among the revised candidates of fitting curve, the most appropriate curve was determined to show a minimum deviation between the shifted points and candidate curve. This iterative modification of fitting curve was conducted for at least 30 times at each elevated temperature condition. Finally, the quasi-static yield stress was properly predicted through the sequential shifting of yield in higher

temperature conditions based on the iterative modification of prediction curve.

When it comes to applying the present method, the following features need to be considered for the robust and accurate estimation. First, when selecting the data set, the linearity should be guaranteed to demonstrate the same nature of rate process. Plus, the prediction region should be magnified sequentially from the initial region where the deviation of nature in the rate process is minimal. Moreover, the more proper estimation of yield stress will be possible with the more yield stress points, especially for the region showing larger deviation in the nature of rate process. In this regard, the validation of proposed method is conducted at the end of section by the comparison between the full and limited data sets.

Yield points at 300 K were derived from 10^{8}/s to 10^{11}/s at the interval of $10^{0.5}$/s and fitted with Eq. (4.4) as shown with grey dash line in Fig. 4.7(a). Based on the previous shifting factor method of two rate processes[18,19], each shifting factor ratio for the data points of 350 K is derived and represented by the grey solid lines in Fig. 4.7(a). Taking these solid lines as a guideline, the data set was shifted while maintaining its original slope. As can be seen in Fig. 4.7(a), the first shifted points (grey square points) are deviated from the initial prediction curve (grey dash line). It means that in fact, the initial prediction curve is not enough to predict the yield of lower strain rate range. Thus, the initial prediction curve is modified with the shifted points as shown with blue dash line in Fig. 4.7(a). Following the iterative update process with the data set of 350 K, the most appropriate curve is determined with the final shifted points (red circle points) and shown with blue solid line in Fig. 4.7(a).

Comparing with the previous prediction curve shown with grey dash line in Fig. 4.7(a), the updated curve displays quite different quasi-static yield stress in a lower strain rate range. With the same manner, the data points in 400 K and 450 K were shifted and the fitting curve was iteratively updated.

One thing to be noted is that the data points for 450 K was divided into two groups depending on their slope as represented in Fig. 4.6. Since the change in yield stresses with the strain rate is nonlinear in this case, we separated the obtained raw data into two groups having different slope respectively and then applied the shifting process for each group. From the present shifting method, the profile for the shifted yield stress along the logarithmic strain rate is constructed at the target temperature (300 K) in Fig. 4.8(a). With the shifted strain rate condition, the ultimate tensile strength is also plotted in Fig. 4.8(b). Interestingly, the ultimate tensile stress decreases more rapidly than the yield stress. This behavior is likely to be attributed to the more relaxed state of the post-yield region. Lastly, as shown in Fig. 4.8, the two predicted values show a good agreement with the experimental results, which are represented by the dotted line. From the present model, we expect that the effect of physical parameters influencing the yielding of amorphous polymers as reported in the previous literature can be further considered, such as crosslinking ratio[6,9], crosslinking method[6], and system size[9].

To confirm the robustness of proposed method, we compared the predicted results from the full data sets (identical data sets with the Fig. 4.8(a)) and limited data sets. The following data sets for yield stresses are considered for the case of using limited data sets:

10^{10}/s, 10^{8}/s (350 K), 10^{10}/s, 10^{8}/s (400 K), and 10^{10}/s, 10^{9}/s, 10^{8}/s, $10^{7.5}$/s, $10^{6.5}$/s (450 K). In total, four points are omitted for the limited data set to compare with the result of using the full data sets. Although the data points are omitted, the slope of each data set at reduced yield versus logarithmic strain rate profile is maintained without showing a significant deviation. The predicted yield stresses with the strain rate for the cases of full data sets and limited data sets are given in Fig. 4.9, showing almost identical trend. Only minor difference (about 2 MPa) is observed under the quasi-static strain rate range. The application of many intermediate data points to the shifting procedure can possibly improve the accuracy of yield stress evolution. As far as the overall trend in yield stresses is concerned, the omission of intermediate points in the data set does not hinder the prediction of quasi-static yield and overall yield evolution with varying strain rate when the linearity is ensured in the limited data set. Above all, the most important point in predicting of quasi-static yield is that the overall accuracy can be substantially enhanced by deriving more yield stress points which can be shifted to the quasi-static strain rate region.

- **Quasi-static (low rate) stress-strain equation via established yield model**

The quasi-static mechanical response can be estimated via the suggested yield model by considering the quasi-static elastic and hardening law. Since the elastic modulus generally varies with the strain rate, as reported in previous studies[13,87], the quasi-static elastic modulus must be determined in an MD environment in order to establish the stress-strain profile. Therefore, the modulus under the reference state (300 K) without any rate

effect was obtained from the Parrinello-Rahman fluctuation strain method in **Chapter 2.1**. To describe the plastic response of the epoxy polymer, Ludwick's hardening model is adopted according to the following form:

$$\sigma_e = \sigma_Y + h(\varepsilon^p)^n, \tag{4.5}$$

where σ_e, h, ε^p, and n are the von Mises's effective stress, strength coefficient, effective plastic strain, and hardening exponent, respectively. As well as the elastic modulus, the hardening of glassy polymers under 10^{10}/s, 10^9/s, and 10^8/s conditions (at 300 K) also indicates the rate-dependent characteristics, as reported by previous studies[88–90]. The values of h and n rapidly decrease as the strain rate decreases to 10^8/s, indicating that the slope of the plastic strain range in the stress-strain response significantly decreases. When considering the monotonically hardened plastic behavior of thermoset polymers, this trend also can be explained in terms of the yield model by noting that the distinction between the ultimate tensile strength and yielding quickly becomes constant as the rate decreases as shown in Fig. 4.8(b). In this manner, quasi-static h and n values were determined via exponential fitting by reflecting the rapid convergence.

Finally, the uniaxial tensile behavior of the epoxy polymer was derived, as shown in Fig. 4.10. The quasi-static yield stress, yield strain, Young's modulus, and hardening parameters (h, n) were determined to be 48.12 MPa, 1.52%, 3.17 GPa, 40.81, and 0.44, respectively. The proposed model shows good agreement with the experimental stress-strain profiles[91,92]. As indicated by Fig. 4.10, the quasi-static yield strain is found to be about 1.52%, which represents a drop by about 4–5% (as compared to the computational

rate conditions) and is attributed to the strain rate dependency on the yield strain as reported in previous study[93]. In addition, the suggested quasi-static model can describe the rate effect by considering the rate-dependent elastic and hardening law, which can be derived from the exponential form.

4.2. Prediction of quasi–static constitutive laws by classical yielding theory

In this chapter, considering the drawbacks of the existing methods that overcome the timescale limitations, the method using 0 K solution of Argon's theory to derive quasi–static yield stress has been further developed to represent the nonlinear characteristics of the polymer plasticity by additionally taking into account the influence of the hydrostatic pressure and crosslinking density. The cooperative model is intensively adopted to represent the nonlinear characteristics of the yield stress with varying strain rate and predict quasi–static solution under different temperature using a glass transition temperature as a criterion for the extinction of the internal yield stress.

4.2.1. Prediction of quasi–static yields and construction of master curve

- **Glass transition temperature**

Similarly to **Chapter 4.1**, the glass transition temperature (T_g) of epoxy polymers was estimated from density–temperature relations for the prediction of quasi–static yields, since T_g displays an substantial correlation with the characteristic stress such as yield stress as also described in classical yielding theory[43]. In order to derive the density–temperature profile, the fully relaxed unit cell was annealed up to the temperature of 450 K by *NPT* ensemble simulations for 5 ns where the epoxy belongs to rubbery state. Then, the unit cell

was cooled down with the rate of 0.01 K/ps by monitoring the density and temperature. The simulations were conducted considering three different crosslinking ratio, 75%, 80%, and 85%, which are the crosslinking conditions of the models in Table 4.2. The derived density–temperature profiles are shown in Fig. 4.11. The T_g is determined as a temperature where the slope of the profile is abruptly changed. Note that the linear lines of Fig. 4.11 is fitting lines based on the determined temperature. Although the extent of the cure influences the determination of T_g[5,94,95], the predicted density–temperature profiles under the considered range of crosslinking density do not show clear variation of T_g according to the crosslinking density. It might result from the inherent variation of density with the temperature fluctuation, prohibiting the exact prediction on subtle change of T_g corresponding to the 10 % change of the crosslinking density. Thus, in this study, the T_g of 80 % crosslinked model 375 K is used as representative temperature for the prediction of the quasi–static yield solutions.

- **Derivation of quasi–static solutions for yield stress**

For the construction of quasi–static constitutive laws of epoxy polymer, the quasi–static yield stress needs to be identified from the MD simulations considering various temperature, pressure, and crosslinking densities. In this **Chapter 4.2**, the quasi–static solutions are derived using the 0 K yield stress of Argon theory following the details of previous research[21]. The strain rate is expressed by Arrhenius form with a critical free enthalpy, which is required to occur the yielding event, as follows:

$$\dot{\gamma} = \dot{\gamma}_0 \exp\left(-\frac{\Delta G^*}{k_b T}\right), \tag{4.6}$$

where $\dot{\gamma}_0, \Delta G^*, k_b$ denote pre–exponential factor (10^{13} s^{-1}), critical free enthalpy, and Boltzmann constant. The change in free enthalpy of the polymer chain due to the double wedge disclination is written as follows:

$$\Delta G = \frac{3\pi\mu\omega^2 r^3}{16(1-\nu)} - \frac{9\pi\omega^2 r^3}{8(1-\nu)}\left(\frac{r}{z}\right)^5 - \pi\mu\omega^2 r^3 \frac{\tau}{\mu}\frac{z}{r}, \tag{4.7}$$

where $\mu, \omega, r, \nu, \tau$ represent shear modulus, kinking angle, molecular radius, Poisson's ratio, and critical stress respectively. The free enthalpy denotes the sum of self–energy of the kinks, their interaction energy, and work done by external stresses during the creation of the kinks. Then, the differentiation of the Eq. (4.7) with respect to z is obtained in order to find a moment when the free enthalpy is maximized. The maximum free enthalpy is obtained when satisfying:

$$\frac{z}{r} = \left(\frac{45}{8(1-\nu)}\frac{\mu}{\tau}\right)^{1/6}. \tag{4.8}$$

The critical free enthalpy of Argon theory is obtained with substitution of Eq. (4.8) into Eq. (4.7) as follows:

$$\Delta G^* = \frac{3\pi\mu\omega^2 r^3}{16(1-\nu)}\left[1 - 8.5(1-\nu)^{5/6}\left(\frac{\tau}{\mu}\right)^{5/6}\right]. \tag{4.9}$$

Then, the critical stress can be expressed with substitution into Eq. (4.6) as:

$$\tau = \frac{0.077}{(1-\nu)}\mu\left[1 - \frac{16(1-\nu)kT}{3\pi\mu\omega^2 r^3}\ln(\dot{\gamma}_0 / \dot{\gamma})\right]^{6/5}. \tag{4.10}$$

The main advantage of the Argon theory compared to the other classical yielding theories is that the critical stress is expressed by the several mechanical properties that can be directly derived by the MD simulations. When focusing on the 0 K solution of Eq. (4.10), the quasi–static yield stress can be expressed as:

$$\left(\frac{\sigma_y}{\mu}\right)_{T=0} = C\frac{0.077}{(1-\nu_{T=0})}, \tag{4.11}$$

where C is the ratio factor between shear yield stress and 1–d yield stress that is assumed as $\sqrt{3}$. The 0 K solution can be extended toward the high temperature range with the construction of the correlation between the mechanical properties and temperature.

Concerning the yield stress–temperature relationship, the previous researchers assumed that the yield stress–temperature relationship under the MD strain rate is consistently maintained up to the quasi–static conditions[21,23]. Accordingly, the quasi–static yield stresses under different temperature are predicted by the linear yield stress–temperature law obtained from the MD strain rates. It means that the constant amount of the yield stress is dropped with the steady temperature increase regardless of the strain rate condition. However, the assumption might be inappropriate for broad range of polymer materials; the yield stress also nonlinearly varies with the change of temperature especially under extremely low temperature and yield theories have been developed to consider such physics[14,15,19]. Moreover, the linear dependence of the yield stress on temperature also violates the nonlinear dependence on strain rate that has been previously observed by many experiments and theories[13–19]. In order to avoid the discrepancy in this chapter, the

cooperative model for the polymer plasticity is adopted by making use of the feature of the yield stress defined in the model[14–16]. The cooperative model considers multiple relaxation nature of polymers to represent the nonlinear characteristics of the yield stress with respect to the temperature and strain rate. The cooperative model restricts the stress that is involved in the activated rate process by subtracting internal stress from the yield stress, which is called effective stress:

$$\sigma^* = \sigma_y - \sigma_i, \tag{4.12}$$

where σ^*, σ_i denote the effective stress and internal stress respectively. The resulting strain rate is determined by the effective stress and effective strain rate as follows:

$$\dot{\varepsilon} = \dot{\varepsilon}^* \sinh^n\left(\frac{\sigma^* V}{2kT}\right), \tag{4.13}$$

where $\dot{\varepsilon}^*, V$ represent the effective strain rate and activation volume respectively. It means that not all portion of the yield stress is influenced by the strain rate variation. The effective stress only determines the dependence of the yield stress with respect to the strain rate. Considering these aspects, the cooperative model for the yield stress below T_g is represented as follows[15]:

$$\sigma_y = \sigma_i(T) + \frac{2kT}{V}\sinh^{-1}\left(\frac{\dot{\varepsilon}}{\dot{\varepsilon}^*}\right)^{1/n}, \tag{4.14}$$

where $\sigma_i(T)$ is given as:

$$\sigma_i(T) = \sigma_i(0) - \frac{\sigma_i(0)}{T_g}T. \tag{4.15}$$

These relations mean that while the yield stress resulting from the strain rate effect

nonlinearly varies under extremely low temperature due to the influence of the effective stress, the internal stress which does not participate in rate process can be predicted with T_g by linear dependence law on the temperature. Concerning the cooperative model Eq. (4.14), the internal stress $\sigma_i(T)$ is limit of the yield stress at given temperature as the strain rate vanishes. It implies that the prediction of quasi–static yield at different temperature is possible by establishing the relationship between the internal stress and temperature Eq. (4.15), which is composed in such a way that the internal stress disappears at T_g. The internal stress without any temperature effect $\sigma_i(0)$ is estimated by the 0 K solution of Argon theory Eq. (4.11).

The influence of the hydrostatic pressure on the yield stress can be considered by the phenomenological linear dependence[15]. The linear dependence of yield stress on arbitrary pressure can be written as follows:

$$\sigma_y(P)=\sigma_y(0)+\alpha_p P, \tag{4.16}$$

where $\sigma_y(P),\sigma_y(0),\alpha_p$ are yield stress at pressure P, yield stress at zero pressure, and pressure coefficient respectively. That is, the yield stress is linearly increased proportionally to the pressure coefficient as the given pressure is increased. Then Eq. (4.16) can be rewritten with the substitution of Eqs. (4.14) and (4.15) as follows:

$$\sigma_y=\sigma_i(0)-\frac{\sigma_i(0)}{T_g}T+\frac{2kT}{V}\sinh^{-1}\left(\frac{\dot{\varepsilon}}{\dot{\varepsilon}^*}\right)^{1/n}+\alpha_p P. \tag{4.17}$$

The quasi–static yield stresses considering the broad range of temperature and hydrostatic pressure can be predicted from both the internal stress–temperature law Eq.

(4.15) and yield stress–pressure law Eq. (4.16), which is reduced form of general version of cooperative model Eq. (4.17). In order to construct the master profile of the yield stress by Eq. (4.17), the yield data under MD strain rates was systematically investigated with the characterizations on the T_g, α_p. Then, the fitting coefficients of Eq. (4.17) which are expressed by the activation volume and effective strain rate are determined correspondingly. The pressure coefficients of the compression and tension were derived as 0.3624, 0.2908 respectively for the considered epoxy by averaging the results of $10^{9.5}$/s, 10^{9}/s, and $10^{8.5}$/s deformation tests with M4, M7, M8, and M9 models in Table 2.3.

4.2.2. Effects of temperature, pressure, and crosslinking density

- **Effect of temperature**

The yield data of the epoxy models M1, M2, M3, M4 was examined to elucidate the influence of the temperature and shown in Fig. 4.12 and Table 4.2. As expected, the yielding behaviors represent huge dependence on the strain rate and temperature; the yield stress is decreased with the extended relaxation time and elevated temperature during the deformation tests. This trend confirms the equivalent role of the time and temperature in the plastic deformation of amorphous polymers as presented by the classical yielding theories[14–19,42,47]. Based on the obtained quasi–static yield stresses, the yield data were fitted with the cooperative model Eq. (4.17) and the fitted master curves according to the temperature are shown with red solid lines in Fig. 4.12. Concerning the quasi–static yield

stresses of both compressive and tensile loadings, the 0 K solution of the Argon theory does not denote distinct deviation with the yield stresses under 0 K and $10^{7.5}$/s, 10^{7}/s. As the considered temperature increases, the strain rate where the MD yield stress is roughly converged to the quasi–static yield is correspondingly decreased. Accordingly, the master curve at 300 K is converged at the lowest strain rate compared to the other temperatures. It might be inferred that the increase of the kinetic energy on the polymer segments can sufficiently dissipate the applied stress for given relaxation time as the chain relaxation behaviors are gradually active.

The observations on the different rate of the convergence to the quasi–static solutions suggest that the yield stress–temperature relation is closely dependent on the considered strain rate condition. When considering the strain rate of about 10^{8} /s in Fig. 4.12(a), the change of the yield stress between 0 K and 100 K is about 100 MPa which is definitely larger than the change between 200 K and 300 K which is about 50 MPa. That is, the yield stress is highly increased as the temperature is decreased from 100 K to 0 K, which corresponds to the experimental observation[19]. This trend is consistently observed in the behavior of the tensile deformations Fig. 4.12(b). In contrast, the yield stress is steadily dropped with the temperature increase at quasi–static condition as denoted in Figs. 4.12(a) and 4.12(b), corresponding to the ratio of internal stress at 0 K and glass transition temperature as denoted in Eq. (4.15). It implies that the assumption of the previous works[21,23], which states that the linear dependence of the yield stress on the temperature is constantly maintained regardless of the strain rate condition, might not be suitable for the

broad range of amorphous polymers. In a methodological sense, the adoption of Eq. (4.15) allows to avoid the assumption on the yield stress–temperature law that might be physically incorrect by just constructing the relation between quasi–static yield and temperature.

- **Effect of hydrostatic pressure**

The influence of the applied hydrostatic pressure is also examined up to 5000 atm considering different strain rates from the deformation simulations by the models M4, M7, M8, and M9 in Table 2.3. The amount of the increase of quasi–static yield stress is estimated based on the pressure coefficients that were evaluated from the MD yield data. The yield data and fitted profiles under different pressure conditions are shown in Fig. 4.13 and Table 4.3. As expected, the increase of the applied pressure results in the higher estimation of the yield stress under all of strain rate range. Especially, the higher pressure coefficient is estimated under compressive loading condition since the amorphous polymers generally display severe dependence on the hydrostatic pressure[15,52]. All of the master profiles at different pressures are nonlinearly converged under both loading conditions.

- **Effect of crosslinking density**

The influence of the crosslinking density on the yield stress evaluation is also examined under different strain rates from the deformation simulations by the models M4, M5, and M6 in Table 2.3. The estimated yield stresses and fitted profiles by the cooperative

model are shown in Fig. 4.14 and Table 4.4. As shown in Fig. 4.14, the yield stress is increased with the increasing crosslinking density under both loading conditions as the previous studies reported[96–98], revealing that the finely crosslinked network of the epoxy results in the reinforcement of the strength. However, since the considered range of the crosslinking density is quite narrow, the yield stress just shows minor change compared to the influence of the temperature and hydrostatic pressure of Figs. 4.12 and 4.13. The structural change of the epoxy also causes the modulus change as shown in Table. 4.4; the 10 % change of the crosslink density increases the modulus about 500 MPa. Correspondingly, the quasi–static solution of the Argon's theory Eq. (4.11) also varies according to the modulus variation. That is, the reinforcing effect coming from the network characteristics of epoxy is reflected in the determination of quasi–static yield stress. It can be confirmed under both loading conditions by the fitted master profiles in Figs. 4.14(a) and 4.14(b). When focusing on the quantitative evaluations of mechanical behaviors, the estimation of the effect of crosslinking density on the yield stress enables the detailed comparison with experimental results. The experimental yield stresses[74,75] are comparable to those of the 80 % and 85 % crosslinked models which are fully crosslinked state, while denoting higher stresses than that of 75% crosslinked model.

4.2.3. Construction of quasi–static constitutive laws

- **Construction of 1–d constitutive law at arbitrary strain rate**

Using the obtained quasi-static yield data, 1–dimensional quasi-static constitutive laws can be established by considering the strain rate dependence on the post-yielding behavior of epoxy polymers. The deformation properties of amorphous polymers indicate that the strain rate dependence is observed not only on stress, but also on the strain evolution during elasto-plastic deformation; the yield strain generally varies with the strain rate leading to the change in the tangent stiffness at different strains[78,79]. Thus, it is of primary importance to consider the difference between the yield strains under the MD and quasi-static conditions. In order to determine the strain rate effects on the entire stress-strain profiles, the following scaling law for the rate dependence, in which both the stress and strain are normalized and reconstructed in accordance with the yield point (which was defined by 2.5 % offset rule) and proportional limit, is proposed:

$$\sigma_{nonl}\,|_{\dot{\varepsilon}} = \sigma_{nonl}\,|_{\dot{\varepsilon}_0}\left(\frac{(\varepsilon_y-\varepsilon_{prop})}{(\varepsilon_{y0}-\varepsilon_{prop0})}\varepsilon\right)\cdot\frac{\sigma_y-\sigma_{prop}}{\sigma_{y0}-\sigma_{prop0}}, \tag{4.17}$$

where σ_{nonl} is the stress evolution after the proportional limit; σ_{y0}, ε_{y0}, ε_{prop0} represent the yield stress, yield strain, and proportional limit strain at the initial (MD) strain rate, and σ_y, ε_y, ε_{prop} are the yield stress, yield strain, and proportional limit strain at the final (quasi-static) strain rate. It shows that the nonlinear stress-strain profile at the quasi–static rate is obtained by mapping the profile constructed at the initial strain rate with a ratio determined by the yield point and proportional limit. In this study, it was assumed that the latter parameter remained constant under different strain rate conditions to account for the rate dependence of the strain itself as follows:

$$\varepsilon_{prop} = \varepsilon_{prop0} \cdot \frac{\varepsilon_y}{\varepsilon_{y0}}. \tag{4.18}$$

This relationship characterizes the proportional limit stress and strain at quasi–static condition from the obtained yield stress and strain at the quasi-static conditions. A detailed illustration of the applicability of Eqs. (4.17) and (4.18) is shown in Fig. 4.15, where the data set was obtained from the deformation tests conducted at 300 K and 1 atm by the 80% crosslinked model. As shown in Figs. 4.15(b) and 4.15(c), since ε_y is directly derived from the quasi–static yield stress and stiffness by 2.5 % offset rule, the proportional limits denoted by the blue dotted circles were calculated by Eq. (4.18) using the yield points determined at the MD and quasi-static rates (red symbols) and proportional limits at the MD rate (blue circles). Then, the post-yielding behavior of the MD strain rate (dark green line) was mapped under the quasi-static conditions (green line) using Eq. (4.17). The derived quasi-static constitutive laws of compression and tension show a good agreement with the experimental constitutive responses depicted in Figs. 4.15(b) and 4.15(c).

4.3. Summary

Concerning **Chapter 4.1**, an accelerated method to predict the quasi-static (experimental low strain rate) rate yield from the full-atomic MD simulation has been established by employing the concept of Eyring theory for the yield of amorphous polymer systems. Using the stress-strain responses of amorphous epoxy polymers under different

temperatures and strain rates, the yield stress of each strain rate and temperature can be obtained with the linear elasto-plastic yield criterion. In order to take the nonlinear characteristics of the yield stress into consideration, shifting factor ratios were calculated and applied to shift the yield at the elevated temperature toward the lower strain rate conditions at the target temperature based on the derived trend for the slope of the reduced yield.

The quasi-static yield stress (in accordance with the derived shifting factor ratios) was estimated through the MD simulations and validated with previous experiments, showing good nonlinear rate-dependent behavior. The suggested yield model opens an avenue for establishing a quasi-static stress-strain response with the rate-dependent elasto-plastic law in an MD environment.

With respect to **Chapter 4.2**, the method to predict quasi–static yields has been elaborated based on 0 K solution of Argon theory. In order to consider inefficiency of the proposed method in **Chapter 4.1**, theoretical model has been directly utilized to predict quasi–static yield stress under different temperatures. In particular, the nonlinear dependence of the yield stress on the strain rate and temperature, which was not considered in previous works, is well–described by the adoption of cooperative model and internal stress law under broad range of strain rate. For the construction of quasi–static constitutive laws, the mapping method of hardening law into the arbitrary strain rate condition including quasi–static rate has been proposed simultaneously. The predicted quasi–static constitutive equations are successfully validated with the experiments.

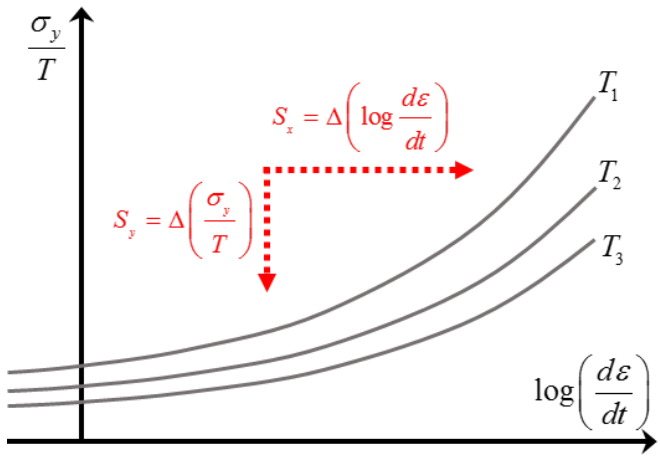

Fig. 4.1. Eyring plots constructed at three different temperatures ($T_1 < T_2 < T_3$) and effects of the shift factors (reproduced from ref. [14]).

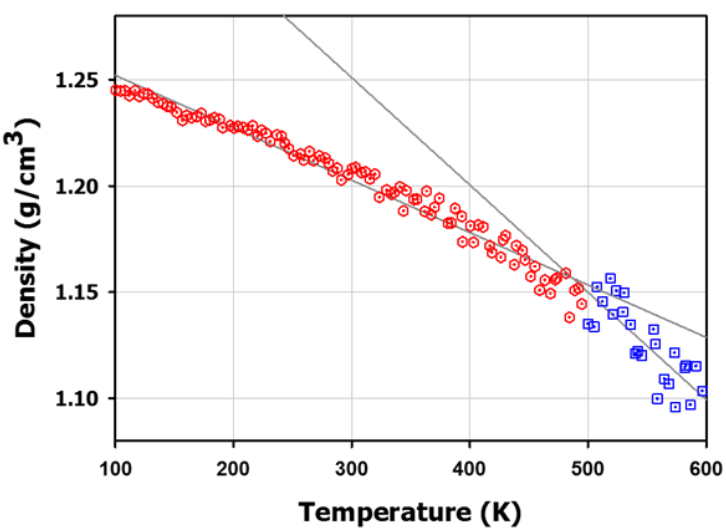

Fig. 4.2. Density-temperature relationship for the target epoxy system, which is used to obtain the glass transition temperature (intersection point).

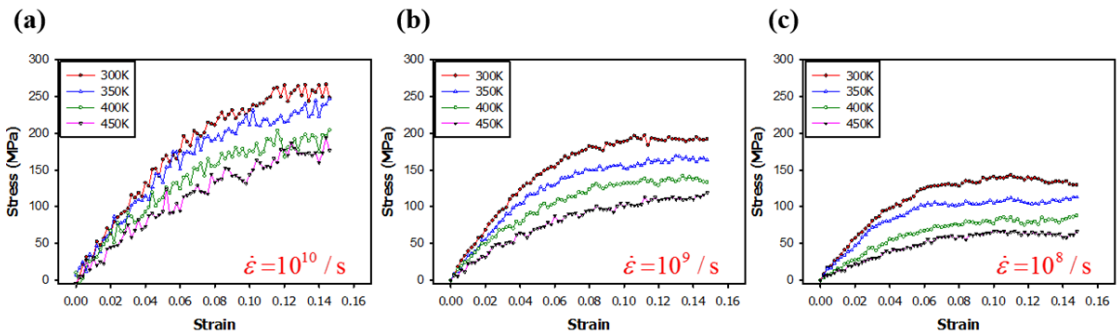

Fig. 4.3. Stress-strain responses obtained at various temperatures (below the glass transition temperature) and strain rates. The temperature/strain rate relationship is observed.

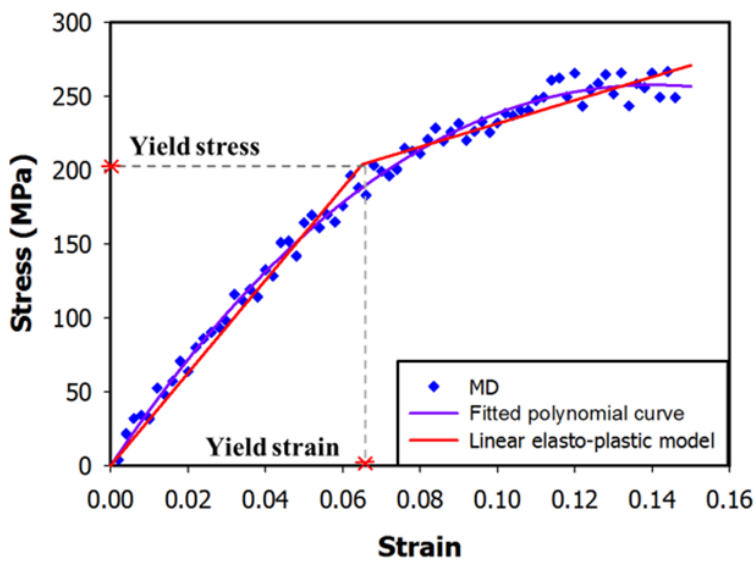

Fig. 4.4. A criterion for the yield point obtained from the stress-strain response. The yield point is determined by fitting the scattered MD data. The linear elastoplastic model is composed of four degrees of freedom: Young's modulus, yield stress, yield strain and hardening exponent.

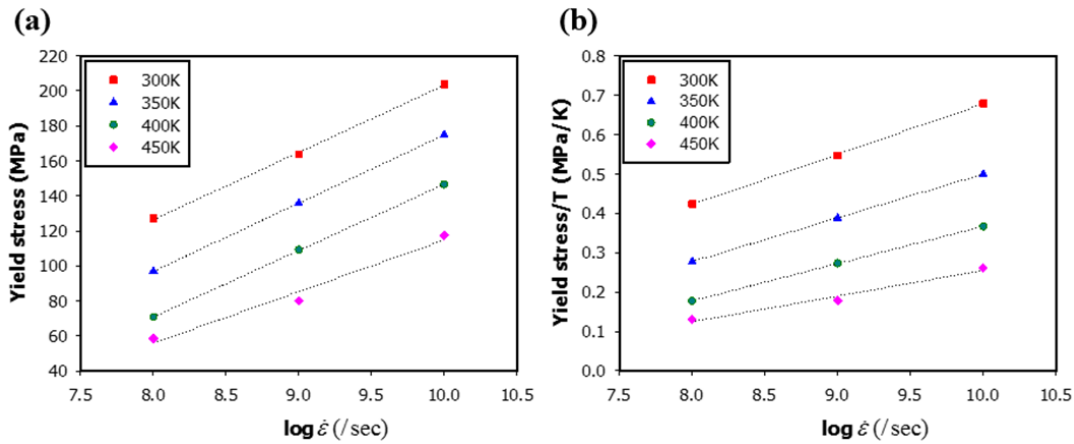

Fig. 4.5. Predicted (a) yield stress and (b) reduced yield stress at various strain rates and temperatures. The slopes of three points set in (b) are determined as 0.128 (300 K), 0.111 (350 K), 0.095 (400 K), and 0.064 (450 K).

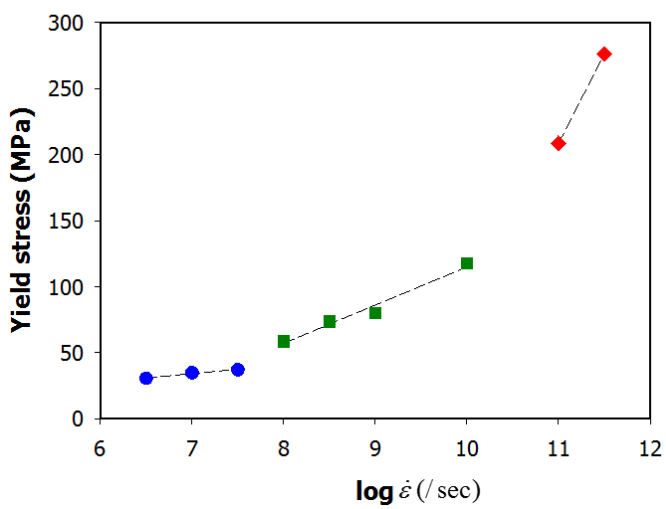

Fig. 4.6. Variation of yield stress depending on the strain rate under 450 K. The yield stresses can be divided into three groups according to the slope change.

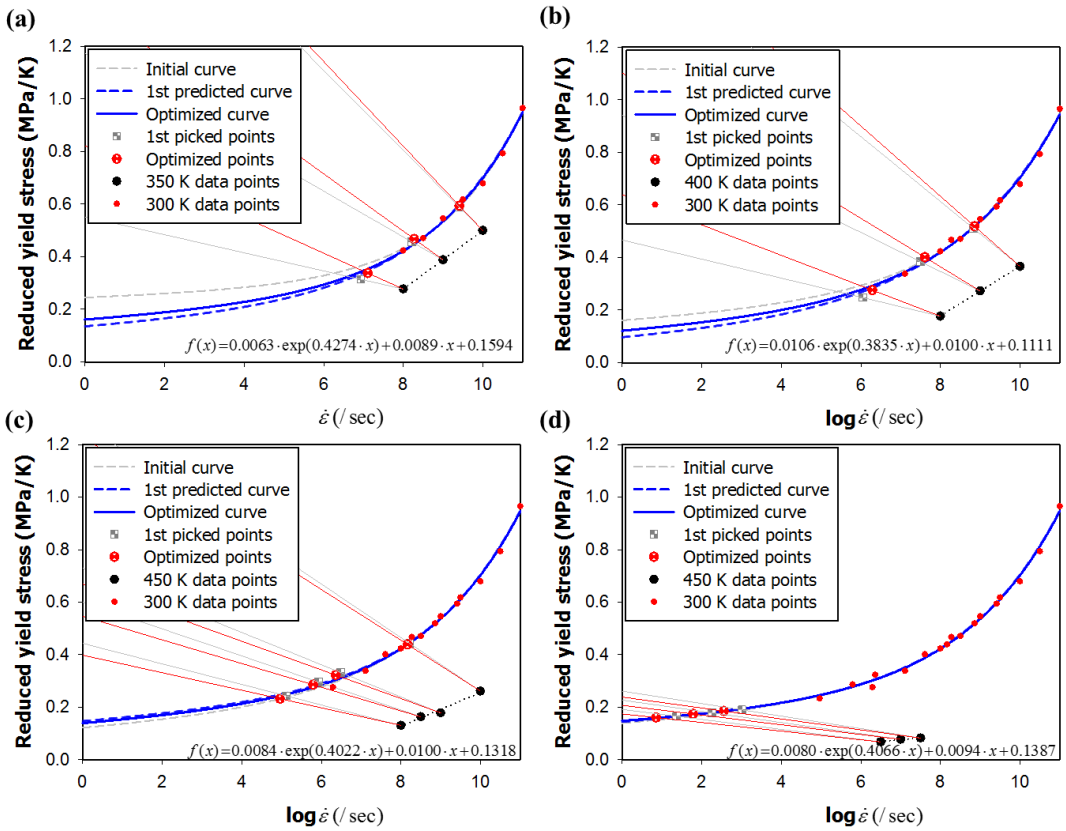

Fig. 4.7. Illustration of construction process of Eyring plot for the reference temperature (300 K). Reduced yield stresses under elevated temperatures ((a) 350 K, (b) 400 K, and (c), (d) 450 K) are shifted to a lower strain rate range based on the derived shifting factor ratio. At each shifting step, the prediction profile is updated iteratively to achieve the appropriate modification of prediction curve. The fitted equation for the final updated curve for each step are given in the figures.

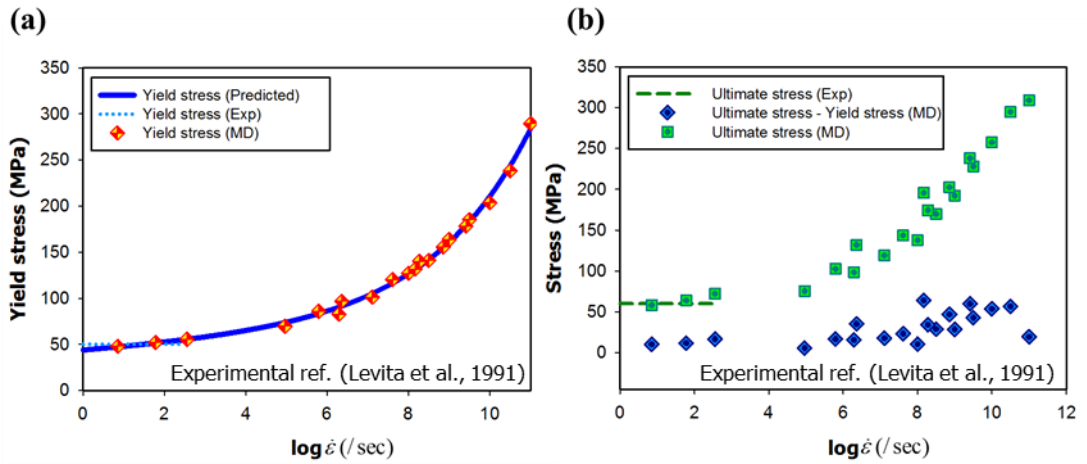

Fig. 4.8. Predicted yield stress (a) and corresponding ultimate stress (b) changes with variation of the strain rate. The obtained curves show good agreements with the magnitudes of the experimental yield stress (50.19 MPa) and ultimate stress (60 MPa), which are obtained from the quasi-static response (experimental test) of epoxy by applying the suggested yield criterion.

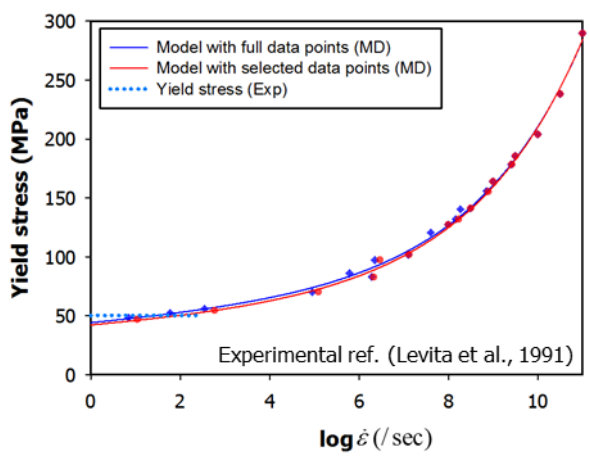

Fig. 4.9. Comparison of prediction profiles between models of using full data points (identical curve in Fig. 4.8(a)) and limited data points.

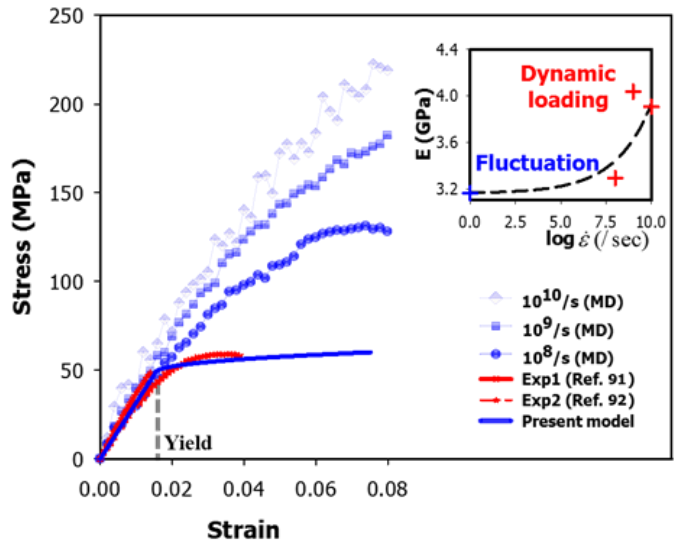

Fig. 4.10. A comparison of the predicted quasi-static (experimental low strain rate) stress-strain solution (blue solid line) with the experimental results. The inset depicts the exponentially fitted Young's modulus as a function of strain rate.

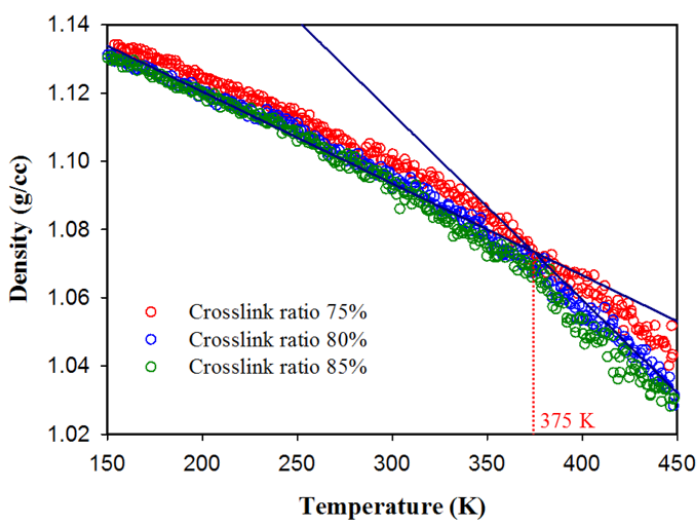

Fig. 4.11. Determination of glass transition temperatures by the density–temperature profiles under three different crosslinking densities (75%, 80%, and 85%).

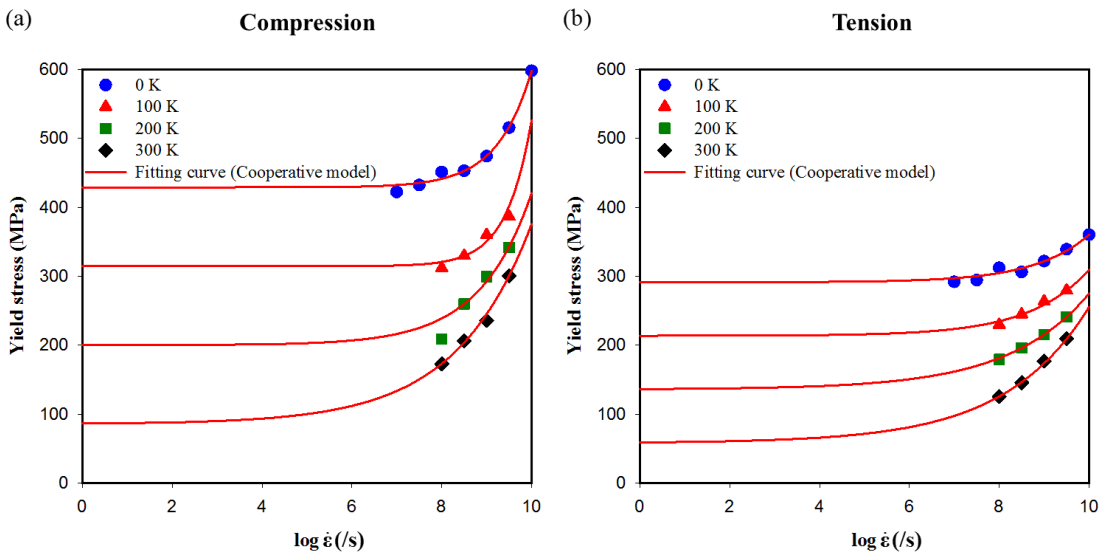

Fig. 4.12. Derived yield stress versus logarithm of the strain rate profiles under (a) compression and (b) tension considering different temperature (0 K, 100 K, 200 K, and 300 K). The yield data at each temperature is fitted by the cooperative model considering the quasi–static yield stress.

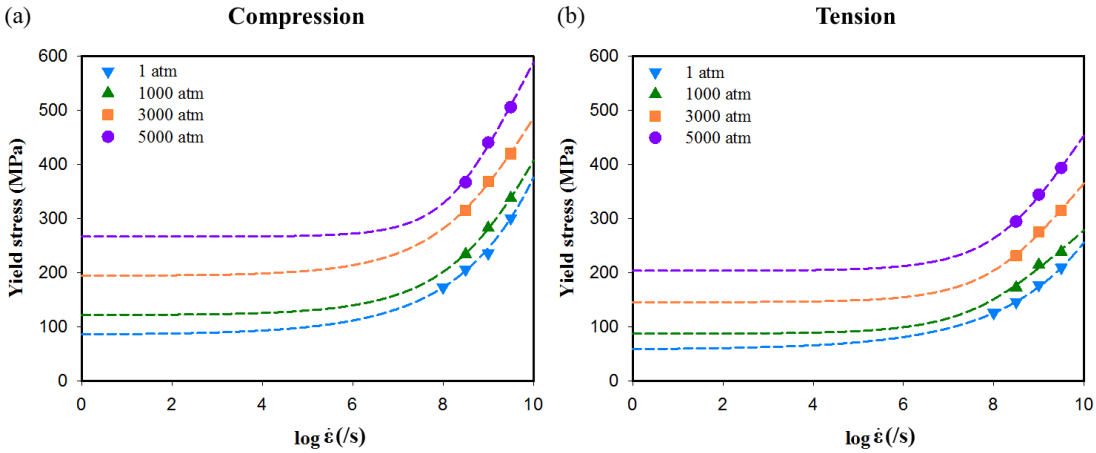

Fig. 4.13. Derived yield stress versus logarithm of the strain rate profiles under (a) compression and (b) tension considering different hydrostatic pressures (1 atm, 1000 atm, 3000 atm, and 5000 atm). The yield data under each pressure is fitted with the quasi–static yield stresses which were predicted by the internal stresses depending on the pressure coefficients.

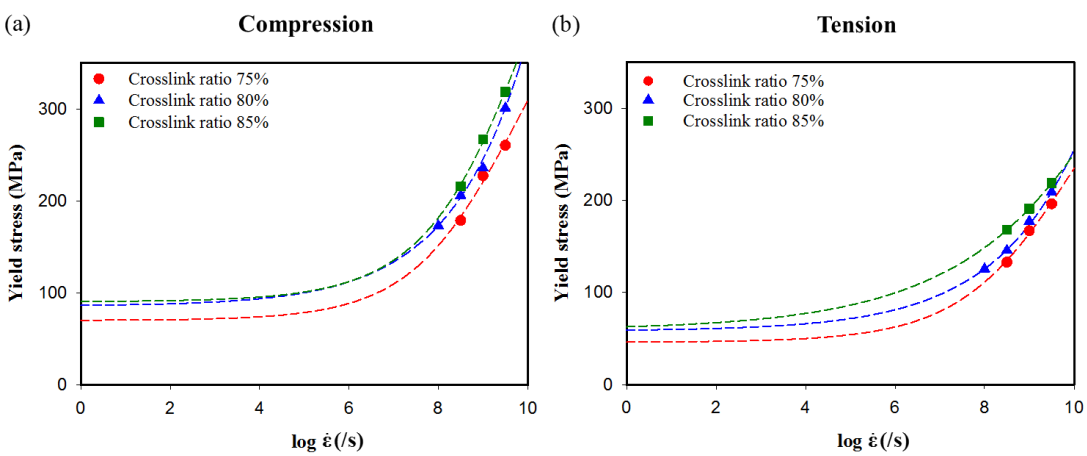

Fig. 4.14. Derived yield stress versus logarithm of the strain rate profiles under (a) compression and (b) tension considering different crosslinking densities (75%, 80%, and 85%). The quasi–static yields were predicted respectively by the Argon theory and used for the constructions of the master curves (dashed lines).

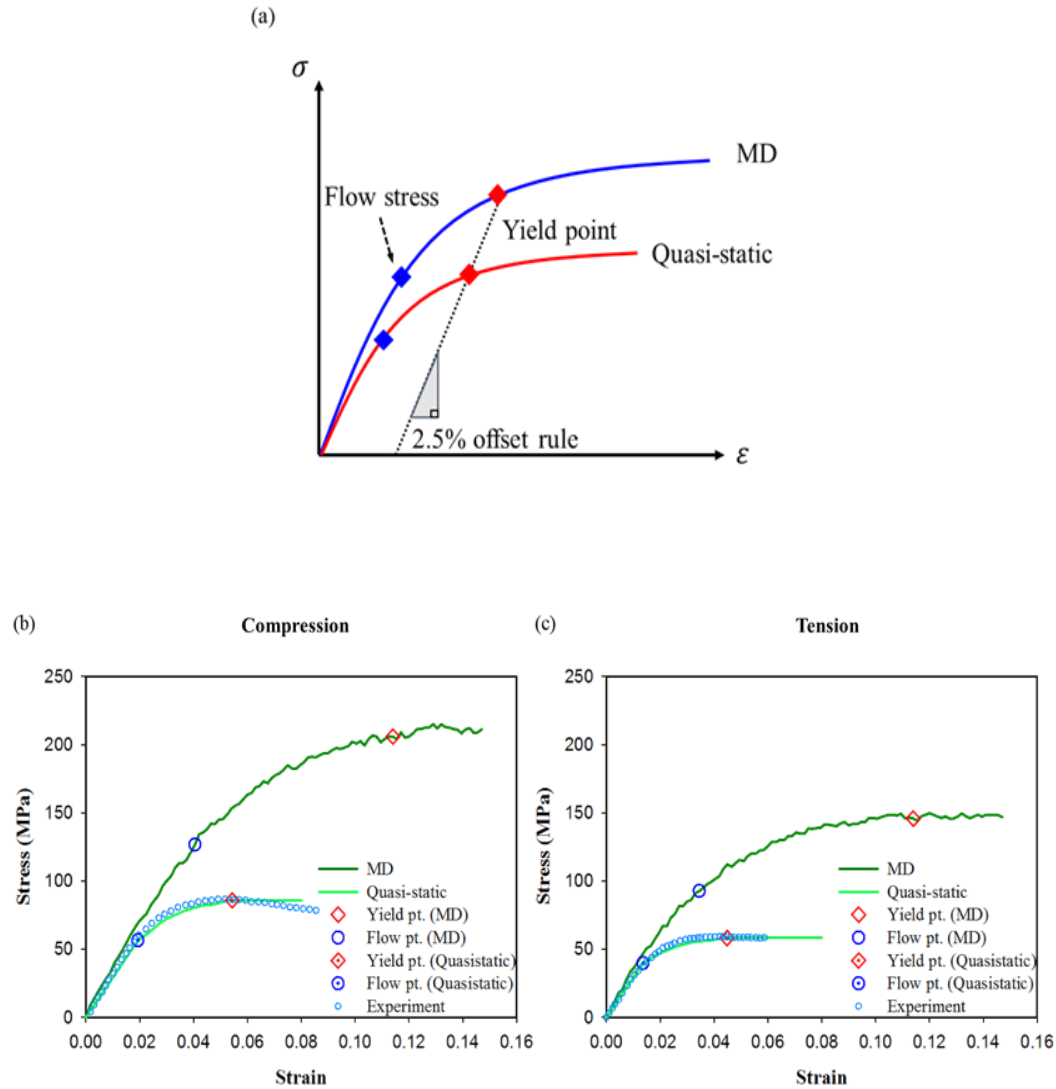

Fig. 4.15. Illustration for (a) the scheme for the construction of the quasi−static post−yielding responses and applications to the (b) compression and (c) tension at 300 K, 1 atm. The MD data was obtained from the 1−dimensional deformation tests of 80% crosslinked model and validated with experimental results[74,75].

Table 4.1

Yield data under different temperature and strain rate conditions for deriving quasi-static yield stress. For the accurate prediction of quasi-static yield, more detailed strain rate conditions of 300 K and 450 K are examined.

Temperature (K)	Strain rate (/ sec)	σ_y (MPa)	ε_y	σ_y / T (MPa/ K)	Slope
300	10^{11}	289.63	0.138	0.9654	
	$10^{10.5}$	238.10	0.077	0.7937	
	10^{10}	203.82	0.065	0.6794	
	$10^{9.5}$	185.36	0.066	0.6179	
	10^{9}	163.78	0.054	0.5459	
	$10^{8.5}$	141.16	0.063	0.4705	
	10^{8}	127.10	0.053	0.4237	
350	10^{10}	174.89	0.059	0.4997	0.1112
	10^{9}	135.82	0.050	0.3881	
	10^{8}	97.05	0.043	0.2730	
400	10^{10}	146.55	0.061	0.3664	0.0946
	10^{9}	109.20	0.057	0.2730	
	10^{8}	70.85	0.050	0.1771	
450	$10^{11.5}$	275.09	0.114	0.6113	
	10^{11}	204.12	0.130	0.4536	
	10^{10}	117.47	0.061	0.2610	0.0643
	10^{9}	80.06	0.053	0.1779	
	$10^{8.5}$	73.51	0.073	0.1634	
	10^{8}	58.61	0.066	0.1302	
	$10^{7.5}$	37.07	0.034	0.0823	0.0146
	10^{7}	34.78	0.035	0.0773	
	$10^{6.5}$	30.49	0.041	0.0678	

Table 4.2.

Derived yield data and quasi–static yield for the construction of the master yield profile considering the influence of temperature. Note that the Young's modulus is derived by the linear regression up to the strain of 1 %.

Crosslink density	Temperature (K)	Pressure (atm)	Deformation	Strain rate (/s)	Yield strain	Yield stress (MPa)	E (MPa)
80%	0K	1atm	Compression	10^{10}/s	0.141	597.93	5809
				$10^{9.5}$/s	0.137	515.57	5647
				10^{9}/s	0.129	474.12	5632
				$10^{8.5}$/s	0.131	452.92	5402
				10^{8}/s	0.132	451.13	5360
				$10^{7.5}$/s	0.129	432.36	5081
				10^{7}/s	0.131	422.21	5082
				Quasi-static	-	429.03	5564
			Tension	10^{10}/s	0.127	360.38	5546
				$10^{9.5}$/s	0.126	339.00	5425
				10^{9}/s	0.123	321.77	5375
				$10^{8.5}$/s	0.122	306.21	5160
				10^{8}/s	0.124	312.15	5035
				$10^{7.5}$/s	0.123	294.20	4792
				10^{7}/s	0.123	291.89	4782
				Quasi-static	-	291.37	5564
	100K	1atm	Compression	$10^{9.5}$/s	0.116	386.66	5163
				10^{9}/s	0.117	359.99	5425
				$10^{8.5}$/s	0.119	329.81	4979
				10^{8}/s	0.120	311.86	4918
				Quasi-static	0.090	314.62	4696
			Tension	$10^{9.5}$/s	0.116	279.43	4569
				10^{9}/s	0.117	263.47	4950
				$10^{8.5}$/s	0.119	244.57	4769
				10^{8}/s	0.118	229.73	4696
				Quasi-static	0.070	213.67	4696
	200K	1atm	Compression	$10^{9.5}$/s	0.111	341.97	4776
				10^{9}/s	0.108	299.48	5202
				$10^{8.5}$/s	0.110	259.96	4421
				10^{8}/s	0.108	209.14	3883
				Quasi-	0.073	200.22	4144

				static			
			Tension	$10^{9.5}$/s	0.113	241.15	4923
				10^{9}/s	0.114	215.51	4786
				$10^{8.5}$/s	0.117	196.35	4497
				10^{8}/s	0.124	179.44	4144
				Quasi-static	0.058	135.97	4144
	300K	1atm	Compression	$10^{9.5}$/s	0.114	300.88	3966
				10^{9}/s	0.107	235.84	4075
				$10^{8.5}$/s	0.114	205.94	3698
				10^{8}/s	0.116	173.04	3091
				Quasi-static	0.054	85.80	2930
			Tension	$10^{9.5}$/s	0.116	209.26	4406
				10^{9}/s	0.111	177.41	3765
				$10^{8.5}$/s	0.114	145.86	3735
				10^{8}/s	0.118	125.71	2930
				Quasi-static	0.045	58.27	2930

Table 4.3.

Derived yield data and quasi–static yield for the construction of the master yield profile considering the influence of hydrostatic pressure. Note that the Young's modulus is derived by the linear regression up to the strain of 1 %.

Crosslink density	Temperature (K)	Pressure (atm)	Deformation	Strain rate (/s)	Yield strain	Yield stress (MPa)	E (MPa)
80%	300K	1000atm	Compression	$10^{9.5}$/s	0.110	337.84	5527
				10^{9}/s	0.105	283.06	4934
				$10^{8.5}$/s	0.108	234.44	4760
				Quasi-static	0.055	122.05	4063
			Tension	$10^{9.5}$/s	0.108	238.60	4595
				10^{9}/s	0.111	214.79	4585
				$10^{8.5}$/s	0.108	172.67	4063
				Quasi-static	0.046	87.35	4063
		3000atm	Compression	$10^{9.5}$/s	0.111	419.89	5025
				10^{9}/s	0.111	368.43	6069
				$10^{8.5}$/s	0.111	315.53	5286
				Quasi-static	0.062	194.53	5256
			Tension	$10^{9.5}$/s	0.111	314.94	6024
				10^{9}/s	0.109	275.72	5655
				$10^{8.5}$/s	0.113	231.22	5256
				Quasi-static	0.053	145.51	5256
		5000atm	Compression	$10^{9.5}$/s	0.111	505.56	7091
				10^{9}/s	0.108	440.32	7013
				$10^{8.5}$/s	0.107	367.14	6347
				Quasi-static	0.071	267.01	5762
			Tension	$10^{9.5}$/s	0.113	393.30	7141
				10^{9}/s	0.109	343.82	6244
				$10^{8.5}$/s	0.107	294.37	5762
				Quasi-static	0.060	203.67	5762

Table 4.4.

Derived yield data and quasi–static yields for the construction of the master yield profile considering different crosslinking densities. Note that the Young's modulus is derived by the linear regression up to the strain of 1 %.

Crosslink density	Temperature (K)	Pressure (atm)	Loading	Strain rate (/s)	Yield strain	Yield stress (MPa)	E (MPa)
75%	300K	1atm	Compression	$10^{9.5}$/s	0.109	260.31	3229
				10^{9}/s	0.113	227.16	4172
				$10^{8.5}$/s	0.108	178.76	3281
				Quasi-static	0.051	70.16	2657
			Tension	$10^{9.5}$/s	0.113	196.39	3620
				10^{9}/s	0.112	167.14	3450
				$10^{8.5}$/s	0.113	132.97	3275
				Quasi-static	0.042	45.90	2657
80%	300K	1atm	Compression	$10^{9.5}$/s	0.114	300.88	3966
				10^{9}/s	0.107	235.84	4075
				$10^{8.5}$/s	0.114	205.94	3698
				10^{8}/s	0.116	173.04	3091
				Quasi-static	0.054	85.80	2930
			Tension	$10^{9.5}$/s	0.116	209.26	4406
				10^{9}/s	0.111	177.41	3765
				$10^{8.5}$/s	0.114	145.86	3735
				10^{8}/s	0.118	125.71	2930
				Quasi-static	0.045	58.27	2930
85%	300K	1atm	Compression	$10^{9.5}$/s	0.116	318.17	4893
				10^{9}/s	0.111	266.84	3807
				$10^{8.5}$/s	0.110	215.83	3551
				Quasi-static	0.053	90.52	3203
			Tension	$10^{9.5}$/s	0113	218.72	3631
				10^{9}/s	0.112	191.21	3686
				$10^{8.5}$/s	0.113	168.24	3536
				Quasi-static	0.043	59.23	3203

5. Classical yield function based constitutive modeling for multi-axial plastic deformations

In this chapter, the derived quasi–static constitutive laws in **Chapter 4.2** were used for the construction of the FE plasticity numerical model based on the paraboloidal yield surface[52] to evaluate multi–axial loading behaviors of epoxy polymers. The FE analysis was carried out by validating the constitutive model by one–element mesh first and evaluating the multi–axial deformation behaviors of open–hall specimen under different crosslinking densities. The constitutive model that was adopted in present chapter is based on the work of Melro et al.[56].

5.1. Constitutive modeling based on paraboloidal yield function

The elastic deformation of the considered epoxy follows the isotropic linear elasticity as follows:

$$\boldsymbol{\sigma} = \boldsymbol{D}^{\boldsymbol{e}} : \boldsymbol{\varepsilon}^{\boldsymbol{e}}, \tag{5.1}$$

where $\boldsymbol{D}^{\boldsymbol{e}}$ is fourth order isotropic elasticity tensor. The stress evaluation can be split into the deviatoric stress tensor and hydrostatic stress as:

$$\boldsymbol{S} = 2G\boldsymbol{\varepsilon}_{\boldsymbol{d}}^{\boldsymbol{e}}, \qquad p = K\varepsilon_v^e, \tag{5.2}$$

where $\boldsymbol{\varepsilon}_{\boldsymbol{d}}^{\boldsymbol{e}}, \varepsilon_v^e, G, K$ are elastic deviatoric strain tensor, volumetric strain, shear modulus,

and bulk modulus of the considered material. The yield criterion for the plastic deformation is described by the paraboloidal yield surface proposed by Tschoegl[52] as:

$$\Phi(\boldsymbol{\sigma},\sigma_c,\sigma_t)=6J_2+2I_1(\sigma_c-\sigma_t)-2\sigma_c\sigma_t, \tag{5.3}$$

where J_2, I_1 are second invariant of the deviatoric stress tensor $J_2=1/2\boldsymbol{S:S}$ and first invariant of the stress tensor $I_1=tr(\boldsymbol{\sigma})$, and σ_c,σ_t are compressive and tensile yield stresses. Concerning the evolution of the plastic strain, non–associative flow rule is used for a correct definition of the volumetric deformation as follows:

$$g=\sigma_{vm}^2+\alpha p^2, \qquad \dot{\boldsymbol{\varepsilon}}^p=\dot{\gamma}\frac{\partial g}{\partial \boldsymbol{\sigma}}, \tag{5.4}$$

where $\sigma_{vm}=\sqrt{3J_2}$ is von–Mises equivalent stress, $p=1/3I_1$ is hydrostatic stress, α is material parameter which determines the contribution of the hydrostatic pressure on the flow direction, and $\dot{\gamma}$ is increment of the plastic multiplier. The considered α is represented by the plastic Poisson's ratio ν_p as follows:

$$\alpha=\frac{9}{2}\frac{1-2\nu_p}{1+\nu_p}. \tag{5.5}$$

Then, flow rule of Eq. (5.4) is rewritten with considered plastic Poisson's ratio by:

$$\Delta\varepsilon^p=\Delta\gamma\left(3\boldsymbol{S}+\frac{2}{9}\alpha\boldsymbol{I}_1\right). \tag{5.6}$$

The evolution of the yield surface is expressed by the uniaxial hardening laws in Eq. (5.3) that are determined by equivalent plastic strain. The equivalent plastic strain is defined as follows:

$$\Delta\varepsilon_e^p = \sqrt{k\Delta\boldsymbol{\varepsilon}^p : \Delta\boldsymbol{\varepsilon}^p}, \qquad k = \frac{1}{1+2\nu_p{}^2}. \tag{5.7}$$

The stress evaluation of the constructed plasticity model is based on the numerical integration scheme using elastic predictor/return mapping algorithm. The main procedure of the algorithm is to update the elastic predictor tensor by solving the nonlinear equation which is function of the plastic multiplier in an efforts to derive plastic strain increment by Eq. (5.6). This procedure is iteratively performed with Newton–Raphson algorithm to derive proper plastic multiplier at each iteration that satisfies $\Phi(\boldsymbol{\sigma}, \sigma_c, \sigma_t) = 0$. During the time interval $[t_{n,}\, t_{n+1}]$, the deviatoric stress tensor and volumetric stress at t_{n+1} are expressed with the trial stress and computed plastic multiplier by:

$$\boldsymbol{S}_{n+1} = \frac{\boldsymbol{S}_{n+1}^{tr}}{1+6G\Delta\gamma} = \frac{\boldsymbol{S}_{n+1}^{tr}}{\zeta_s}, \; p_{n+1} = \frac{p_{n+1}^{tr}}{1+2K\alpha\Delta\gamma} = \frac{p_{n+1}^{tr}}{\zeta_p}, \tag{5.8}$$

where $\boldsymbol{S}_{n+1}^{tr}, p_{n+1}^{tr}$ are trial deviatoric stress tensor and trial hydrostatic stress at t_{n+1}. Then, the consistency condition of yield surface Eq. (5.3) is represented by the trial stresses Eq. (5.8) as follows:

$$\frac{6J_2^{tr}}{\zeta_s^2} + \frac{2I_1^{tr}(\sigma_c - \sigma_t)}{\zeta_p} - 2\sigma_c\sigma_t = 0. \tag{5.9}$$

In order to apply the Newton–Raphson algorithm to find the plastic multiplier that satisfies Eq. (5.9), the derivative of the consistency condition is expressed as:

$$\frac{\partial\Phi}{\partial\Delta\gamma} = -\frac{72GJ_2^{tr}}{\zeta_s^3} - \frac{4K\alpha I_1^{tr}(\sigma_c - \sigma_t)}{\zeta_p^2} + \frac{\partial\Phi}{\partial\Delta\varepsilon_e^p}\frac{\partial\Delta\varepsilon_e^p}{\partial\Delta\gamma}. \tag{5.10}$$

The derivatives $\frac{\partial \Phi}{\partial \Delta \varepsilon_e^p}, \frac{\partial \Delta \varepsilon_e^p}{\partial \Delta \gamma}$ in Eq. (5.10) are given by:

$$\frac{\partial \Phi}{\partial \Delta \gamma} = 2\left(\frac{\partial \sigma_c}{\partial \Delta \varepsilon_e^p} - \frac{\partial \sigma_t}{\partial \Delta \varepsilon_e^p} \right) \frac{I_1^{tr}}{\zeta_p} - 2\left(\sigma_c \frac{\partial \sigma_t}{\partial \Delta \varepsilon_e^p} + \sigma_t \frac{\partial \sigma_c}{\partial \Delta \varepsilon_e^p} \right) \equiv \hat{H}, \tag{5.11}$$

$$\frac{\partial \varepsilon_e^p}{\partial \Delta \gamma} = \sqrt{\frac{1}{1+2\nu_p^{\,2}}} \left(\sqrt{A} - \frac{\Delta \gamma}{2\sqrt{A}} \left(\frac{216 G J_2^{tr}}{\zeta_s^3} + \frac{16 \alpha^3 K (I_1^{tr})^2}{27 \zeta_p^{\,3}} \right) \right), \tag{5.12}$$

where A is defined as:

$$A = \frac{18 J_2^{tr}}{\zeta_s^{\,2}} + \frac{4}{27} \left(\frac{\alpha I_1^{tr}}{\zeta_p} \right)^2 . \tag{5.13}$$

The consistent tangent operator in plastic deformation regime is derived from the derivative of the stress which can be represented by Eq. (5.8). The detailed procedure is presented in the work of van der Meer et al.[96]. The consistent tangent operator is given by:

$$\frac{\partial \boldsymbol{\sigma}}{\partial \boldsymbol{\varepsilon}} = \beta \boldsymbol{I}_4^s + (\phi - \frac{\beta}{3}) \boldsymbol{I}\boldsymbol{I} - \rho \boldsymbol{S}^{tr} \boldsymbol{I} - \chi \boldsymbol{S}^{tr} \boldsymbol{S}^{tr} - \psi \boldsymbol{I}\boldsymbol{S}^{tr} - \omega \boldsymbol{S}^{tr} \boldsymbol{E} - \xi \boldsymbol{I}\boldsymbol{E}, \tag{5.14}$$

where $\beta, \phi, \rho, \chi, \psi, \omega, \xi$ are coefficients for each term, and $\boldsymbol{I}_4^s, \boldsymbol{E}$ are deviatoric fourth order identity tensor and derivative of the equivalent plastic strain with respect to strain $\frac{\partial \varepsilon_e^p}{\partial \boldsymbol{\varepsilon}}$. The coefficients are represented by:

$$\begin{aligned} &\beta = \frac{2G}{\zeta_s}, \quad \phi = \frac{K}{\zeta_p} - \frac{4K^2 \alpha I_1^{tr} (\sigma_c - \sigma_t)}{\eta \zeta_p^3}, \quad \rho = \frac{36 K G (\sigma_c - \sigma_t)}{\eta \zeta_s^2 \zeta_p}, \quad \chi = \frac{72 G^2}{\eta \zeta_s^4}, \\ &\psi = \frac{8 K G \alpha I_1^{tr}}{\eta \zeta_s^2 \zeta_p^2}, \quad \omega = \frac{6 G \hat{H}}{\eta \zeta_p^2}, \quad \xi = \frac{2 K \alpha I_1^{tr} \hat{H}}{3 \eta \zeta_p^2}, \end{aligned} \tag{5.15}$$

with

$$\eta = -\frac{\partial \Phi}{\partial \Delta \gamma}. \tag{5.16}$$

5.2. Finite element analysis: one–element mesh validations

- **Quasi–static constitutive laws and 1–element deformation tests**

The systematic predictions of quasi–static constitutive equations of tension and compression were conducted based on the proposed methodology at **Chapter 4.2** and corresponding profiles are presented in Fig. 5.1 as solid lines considering the influence of the temperature (Figs. 5.1(a) and 5.1 (b)), pressure (Figs. 5.1(c) and 5.1 (d)), and crosslinking density (Figs. 5.1(e) and 5.1(f)) respectively. Since the intrinsic deformation characteristics of the considered epoxy is ductile, all of the profiles denotes plateau as the plastic deformation proceeds. The constructed constitutive laws represent the influence of the considered physical conditions and network characteristics well based on the predicted quasi–static yield stresses. The stress under elasto–plastic deformation regimes increases as the hydrostatic pressure and crosslinking density increase and the temperature decreases. The considered conditions also contribute to the initiation of the plastic flow of the epoxy polymers; the decrease of temperature and increase of pressure and crosslinking ratio delay the plastic events of polymer segments under both tension and compression loadings. In particular, the quasi–static constitutive equations obtained from the 80 % and 85 % crosslinked models represent a good agreement with the experimental stress–strains under

both loadings.

The constitutive model was implemented by a UMAT user subroutine of the finite element commercial software package ABAQUS and validated with the quasi–static constitutive laws of which the hardening profiles are used for inputs of FE simulations. In order to validate the constitutive model, the stress–strain profiles of quasi–static MD and FE simulations are intensively compared under tensile and compressive deformations by 1–element mesh. All of the elasto–plastic properties required for the FE analysis were obtained from the quasi–static constitutive equations including modulus and Poisson's ratio. Especially, the plastic Poisson's ratio was calculated from the MD simulations by averaging the results of considered rate conditions.

The results of the 1–element deformation simulations are shown in Fig. 5.1. The solid lines denote established quasi–static constitutive laws and circular symbols represent the constitutive responses of FE analysis. Concerning the influence of the temperature, the 1–element tests were performed under different temperatures (100 K, 200 K, 300 K) based on the quasi–static constitutive equations obtained from the atomistic models (M2–M4 in Table 2.3). Under three different temperatures, the derived stress–strain profiles of 1–element tests perfectly follow the quasi–static MD profiles in both loading conditions as shown in Figs. 5.1(a) and 5.1(b). The influence of the hydrostatic pressure was similarly estimated considering three different hydrostatic pressures (1000 atm, 3000 atm, 5000 atm) based on the quasi–static constitutive equations from the atomistic models (M4, M7–M9 in Table 2.3). The results of both loading conditions also denote perfect coincidence with the considered quasi–static MD profiles. Likewise, the influence of the crosslinking ratio

was also estimated considering three different crosslinking ratios (M4–M6) at 300 K and 1 atm. The results of FE analysis also show perfect agreement with the considered constitutive laws as well as experimental results.

To investigate the multi–axial plastic deformations corresponding to the 1–dimensional hardening laws in Fig. 5.1, the evolution of yield surfaces is observed by depicting the $\sigma_3 = 0$ planes at flow state and severely hardened state simultaneously in Fig. 5.2. Since the considered yield criterion is isotropic and not dependent on the rotation about hydrostatic axis, all of the envelopes evolve elliptically. The effect of the temperature is shown in Fig. 5.2(a) revealing that the temperature drop results in the huge expansion in both flow and hardened states. Likewise, the increase of the pressure also expands the envelopes as presented in Fig. 5.2(b), but extent of the expansion is highly dependent on the loading path. Especially, the initial yield surfaces are not self–similarly evolved with increasing pressure; when focusing on the bi–compressive deformations, the envelope does not show large expansion between 1000 atm and 3000 atm but expanded rapidly from 3000 atm to 5000 atm. This irregular evolution behaviors stem from the functional structure of the yield criterion in which the mathematical terms consisting of compressive and tensile stresses are closely involved. Concerning the effect of the crosslinking ratio in Fig. 5.2(c), the highly crosslinked model also displays more expanded yield surface corresponding to the hardening behaviors of each crosslinking condition. But, it is worth to note that the extent of the expansion is also dependent on the loading directions as observed in Fig. 5.2(b). Since the constitutive laws of 80 % and 85% crosslinked models in Figs. 5.2(e) and 5.2(f) are closely comparable, those two yield surfaces in Fig. 5.2(c) only denotes slight

deviation especially for 1–dimensional tensile and bi–tensile loadings. Although the close match is observed in tensile loading directions, the largest deviation between the yield surfaces of 80 % and 85 % crosslinked models is presented near the bi–compression loading.

5.3. Finite element analysis: open–hole deformation tests

Based on the validated constitutive model, the multi–axial plastic deformation behaviors of the open–hole structure were investigated by monitoring the evolution of the equivalent plastic strain near the hole. In particular, we have focused on the influence of the network topology that is featured by the crosslinking density, observing the influence according to the delay of plastic deformation characterized by the high extent of cure. Concerning the loading path, the bi–axial compression is applied by displacement on the edge plane constraining the deformation on the normal direction to the loading directions, since the deviation between yield surfaces is dominant under bi–compression as can be seen in Fig. 5.2(c). The influence of about 10% variation of the crosslinking density, which is microscopic feature of network topology of epoxy polymer, on macroscopic plastic strain could be quantitatively demonstrated by the open–hole deformation tests.

The results of the open–hole deformation tests are shown in Fig. 5.3 with snapshots of the displacement field and equivalent plastic strain field. The Fig. 5.3(a) denotes the applied displacement field when the 85 % crosslinked structure starts to deform plastically and Fig. 5.3(b) represents the equivalent plastic strain field of three different

crosslinked model at that moment. As can be seen in Fig. 5.3(b), the 75 % crosslinked structure shows prominent plastic deformation compared to those of the 80 % crosslinked structures nearby the hole; the maximum equivalent plastic strain of 75 % crosslinked structure is $5.26e^{-3}$ while the plastic deformation of 80 % and 85 % structures is just initiated. It is natural due to, as confirmed in Figs. 5.1(e) and 5.1(f), the delay of the plastic deformation attributed to the increase of the crosslinks, prohibiting local plastic deformation. This trend is consistently observed as the deformation proceeds. The Fig. 5.3(c) denotes the applied displacement that the 75% crosslinked structure reaches the plateau state. Correspondingly, the maximum equivalent plastic strain is about $2.13e^{-2}$ nearby the hole while the 80 % and 85 % crosslinked structures only denote maximum values about $1.0e^{-2}$. It implies that the 10 % drop of the extent of cure results in about twice of the maximum equivalent plastic strain near the hole.

5.4. Summary

The finite element analysis for elasto–plastic deformations of the epoxy polymer has been conducted by considering the influence of the temperature, strain rate, hydrostatic pressure, and crosslinking density. In order to construct the multiscale framework without any experimental supports, the method to predict quasi–static yields represented in **Chapter 4.2** has been used to derive quasi–static constitutive laws under considered physical environment. The predicted quasi–static constitutive equations are successfully

validated with the experiments with respect to the tension and compression.

Based on the fully characterized constitutive laws, the constitutive model that originally proposed by Melro et al.[56] has been implemented in finite element analysis and validated in tensile and compressive loadings by 1–element mesh tests. The stress–strain responses of FE and quasi–static MD denote close agreement each other, leading to the universal validity of the constructed model. After the 1–element validation, the multi–axial plastic deformations of open–hole structures have been examined by considering the effect of crosslinking density on the local plastic deformations. The deformation simulations confirm the plastic deformation behaviors hugely depending on the microscopic structural change of epoxy. The proposed multiscale framework for the prediction of elasto–plastic deformation of epoxy polymers will be broadly utilized to envisage deformation behaviors where the experimental approach is inefficient or limited. In particular, the proposed framework enables the establishment of correlation between various microscopic structures and plasticity, demonstrating the microscopic structure–plasticity relationships.

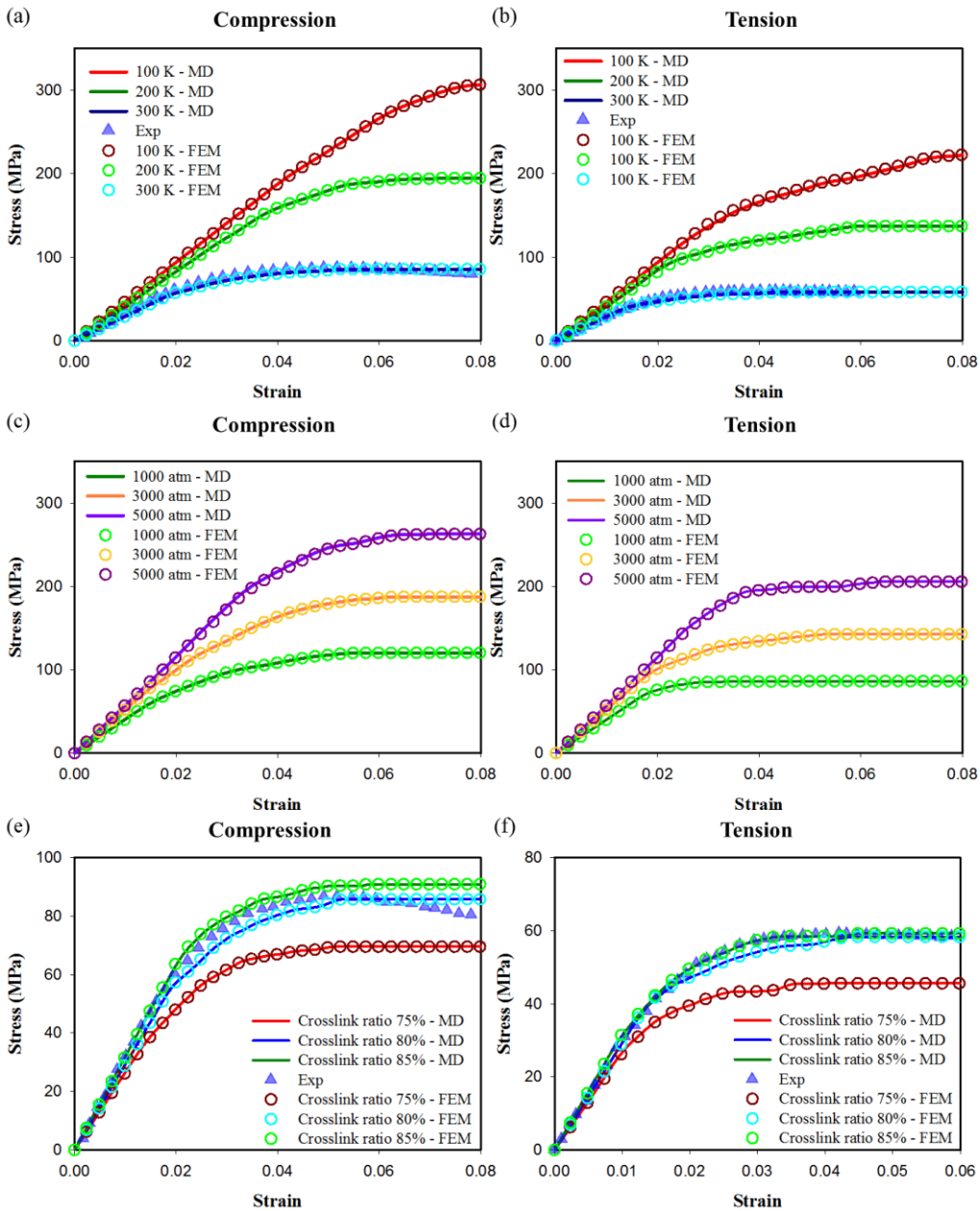

Fig. 5.1. Comparison of the quasi–static constitutive equations and stress–strain profiles obtained from the 1–element simulations considering different temperature ((a) compression, (b) tension), hydrostatic pressure ((c) compression, (d) tension), and crosslinking density ((e) compression, (f) tension). The experimental results in (e) and (f) are taken from the works of Guest et al.[74] and Tsai et al.[75].

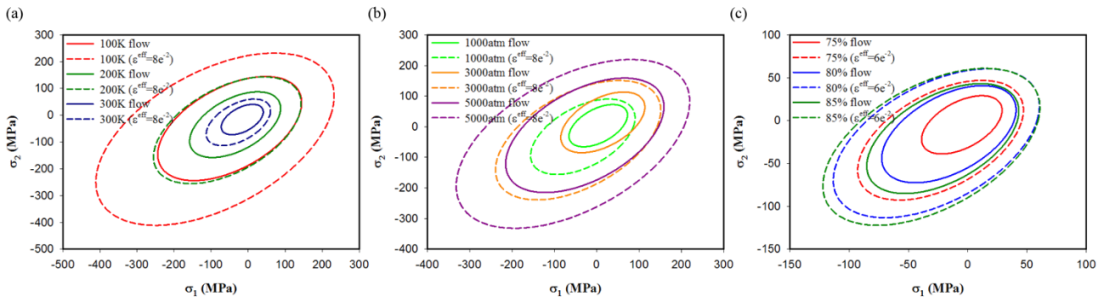

Fig. 5.2. Evolution of the yield surface in $\sigma_3 = 0$ plane which corresponds to the uniaxial hardening laws considering the influence of (a) temperature, (b) hydrostatic pressure, and (c) crosslinking ratio. The definition of the effective strain in work of Rottler et al.[67] is used for specification.

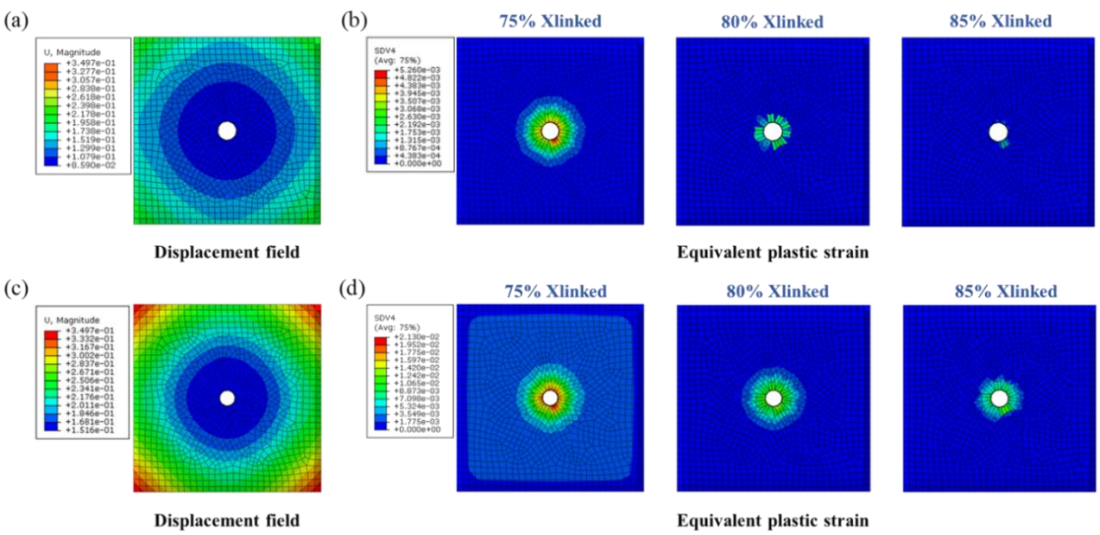

Fig. 5.3. Applied displacement fields and corresponding equivalent plastic strain fields depending on the crosslinking ratios. (a) displacement field when the 85 % crosslinked model starts to deform plastically; (b) the equivalent plastic strain field (corresponding to the displacement field (a)); (c) displacement field when the 75 % crosslinked model reaches plateau state; (d) the equivalent plastic strain field (corresponding to the displacement field (c)).

6. Machine learning based data–driven constitutive modeling for multi-axial plastic deformations

In this chapter, a multiscale framework was proposed to develop a 3–dimensional constitutive model of the epoxy polymer from the data–driven yield function which is formulated by the multi–axial yield data using a machine learning technique. The main focus of this chapter is to confirm that the customized yield functions of various materials can be established only from the given yield data which represents the unique multi–axial hardening behavior without any prior knowledge on the primary stress invariants and functional structures. In order to examine the possibility of yield function mining, the development of the classical yield functions such as von–Mises, Drucker–Prager, Tresca, Mohr–Coulomb, and paraboloidal yield functions was reproduced from the proposed approach simultaneously characterizing the influence of the dispersion of yield data set.

6.1. Reproduction of classical yield functions by symbolic regression

6.1.1. Symbolic regression

Symbolic regression builds a free-form mathematical equation that can correlate nonlinear input and output relationships using evolutionary algorithms. The structure of the function and the coefficients are automatically determined based on the fitness criteria that

the user specifies. Although the symbolic regression automatically gives mathematical expressions regarding the given problem, the user can carefully select the model, based on the characteristics of the problems and the complexity of models, to avoid the overfitting issue[70]. Therefore, investigator knowledge and insight regarding the given problem is significantly important in solving problems.

The symbolic regression starts by randomly generating solution candidates, which is called the "population" at the first iteration. These candidates might not be able to represent appropriately the nonlinear relationships between input and output. These candidates are updated with an evolutionary algorithm using crossover, mutation, and selection as the iteration is continued. At every iteration, the performance of the model is evaluated by the fitness function, usually represented by the mean squared error (MSE). This iterative process is performed until the user-defined criteria are satisfied. Note that the functional form of the fitness function has significant effects on the finding of a solution. The users are responsible for selecting proper fitness functions for the symbolic regression procedure to succeed.

It is often necessary to consider constraint conditions during the application of evolutionary algorithms that depend on the characteristics that a solution of given problem should display. The most basic way to handle constraints in evolutionary algorithms is to use a penalty function originally proposed by Courant.[97] The penalty function affects the fitness evaluation during the evolution progress, inducing the final solution to satisfy the user-defined constraints. There are many advanced ways to set penalty functions,

depending on the types of the given problems.[98] In the present study, the penalty function is defined to satisfy the condition that the yield function should be coincident with the stress states specified by uniaxial yield stresses. It means that if the arbitrary compressive and tensile stresses are given, the mined yield function should be able to represent the corresponding stress states in principal stress space.

6.1.2. Symbolic data mining of classical yield functions

It is demonstrated in this section that the symbolic data mining can reproduce well-known classical yield functions from the yield data without any prior knowledge of the functions. The exact mathematical formulas of various classical yield functions are produced from limited yield data sets generated by the exact classical function in the $\sigma_3 = 0$ plane. The symbolic data mining was able to consider candidates of stress invariants and find the proper relationship by evaluating the fitness, as calculated from the function's deviation versus the given data set. In particular, the symbolic regression simultaneously screens important stress invariants and finds exact functional structures for some circumstances. In these cases, inappropriate stress invariants for the given problem are eliminated, based on genetic algorithms, while the proper mathematical expression composed of meaningful stress invariants is automatically formulated. All procedures of symbolic data mining reported here were conducted on the basis of the symbolic regression algorithm of Searson.[99]

In addition, it is necessary to verify that symbolic regression also can produce the yield functions under the circumstance where the yield data set is arbitrarily dispersed in stress space due to the noise of raw data. If yield function mining is possible, it is also worthwhile to identify the threshold error under which the expected yield function can be still reproduced. In this work, the arbitrary error was uniformly applied on the principal stress coordinates in stress space by regulating the lower and upper bound of the coordinates. For example, when each component of the stress coordinates arbitrarily varies within 10 % of the lower and upper range of its original value, it is called herein "10 % dispersion," for convenience. For all these cases, the arbitrary error was applied up to a maximum of 40 % to provide for the influence of the dispersion of raw data on the results of symbolic data mining.

As a first example for classical yield function mining, the data set of von–Mises yield function was generated by exact von–Mises yield function of Eq. (1.1), under the two different yield stresses, 50MPa and 100MPa. The symbolic regression considered the stress invariant set, $\{I_1, I_2, I_3, J_2, J_3\}$ at which a meaningful set of the stress invariants is extracted, and yield stress, σ_y as a fixed node. The fitness function is composed as a MSE calculated by comparing the deviation between training data and prediction model in principal stress space as follows:

$$MSE = \frac{\sum (\bar{\sigma}^{train} - \bar{\sigma}^{pred})^2}{\sum (\bar{\sigma}^{train} - \bar{\sigma}^{mean})^2}, \tag{6.1}$$

where $\bar{\sigma}^{train}$ and $\bar{\sigma}^{pred}$ denotes the general stress state of training data (MD data set) and

the predicted yield function in principal stress space respectively.

The performed symbolic data mining successfully reproduced the formula for von–Mises function under the 0%, 5%, and 10% dispersions and failed after the 20% dispersion condition. The mathematical expressions of mined yield function of 0% and 10% error conditions are shown in Table. 6.1 and the comparison of mined and exact yield functions is shown in Figs. 6.1(a) and 6.1(b). As denoted by models a1 and b1 of Table 6.1, the mined functional structures are completely identical to the von–Mises function. Especially, it should be noted that the symbolic data mining successfully identified the role of the second invariant of the deviatoric stress J_2 in majority of models in Table 6.1, while the contributions of other stress invariants were eliminated during the regressions. It reveals that the symbolic data mining is able to identify the primary stress invariants within the all considered variables simultaneously optimizing the functional structure and the coefficients.

However, the prediction of the exact coefficient of $\sqrt{J_2}$ seems to be a lot harder under severe error. While both of the functional structure and the coefficient of $\sqrt{J_2}$ is accurately determined under 0% dispersion condition as denoted by model a1, it is observed that the determined coefficient of $\sqrt{J_2}$ is getting far away from the exact value $\sqrt{3}$ as the applied error is increased as shown by model b1. The applied error eventually leads to the failure of the prediction of the von–Mises function under 20% dispersion condition.

The second example problem of the function mining is conical yield surface denoted in Eq. (1.3). The symbolic data mining was performed by considering four

arbitrary data sets that are shown in Figs. 6.1(c) and 6.1(d). Unlike to the von–Mises example, the set of stress invariants and yield stresses, $\{I_1, I_2, I_3, J_3, \sigma_c, \sigma_t\}$, is considered as function nodes to be evaluated while J_2 is considered as fixed node but without any preliminary assumption on its functional form. Due to the complex functional form of the conical yield function and lots of input nodes involved, it is nearly impossible to mine exact solution with the fitness implemented in von–Mises case. Accordingly, the constraint condition is applied to the fitness function in order to reduce the range of functional structure to be probed. The applied constraint condition is that the predicted yield function should pass through the stress states in principal stress space corresponding to the arbitrary compressive and tensile yielding. The constraint condition is implemented to the fitness function by multiplication of MSE as follows:

$$fitness = MSE_1 \cdot MSE_2, \tag{6.2}$$

where MSE_1 is calculated by considered input data set and MSE_2 denotes how much the prediction model deviates from the stress states defined by given 1–dimensional yield stresses σ_c and σ_t.

The performed symbolic data mining successfully reproduced the Drucker–Prager yield function under up to the 20% of dispersion condition. The mathematical expressions of mined yield function under 0% and 20% dispersion conditions are shown in Table. 6.1 and the comparison of mined and exact yield functions is shown in Figs. 6.1(c) and 6.1(d). The most important point of this example is that the symbolic regression is able to represent the pressure–dependency of the considered data set by introducing I_1 into the yield

function, which is screened among the stress invariants, $\{I_1, I_2, I_3, J_3, \sigma_c, \sigma_t\}$ based on the fitness function. It implies that the introduction of I_1 into the yield function, which was outcome solely by physical intuition and experience of researchers, was reproduced just by the considered data set even under severe error.

As far as the accuracy of the mined yield function is concerned, it should be noted that the constrained symbolic regression robustly produce the correct form of the conical yield function regardless of the applied error. Unlike to the von–Mises example, all of the mined conical models in Table 6.1 includes the exact conical function even if the applied error is increased up to 20%. The increased error just leads to the complex redundant term that provide extremely small contribution to the overall function as can be seen by models d2 and d3 of Table 6.1. It is because the narrowed exploration range of functional structure of yield function leads to find out the exact yield function although the severe noise on the data set is concerned.

The symbolic data mining for the Tresca, Mohr–Coulomb, and paraboloidal yield functions was performed by applying the constraint condition as in the case of the Drucker–Prager yield function. For the cases of the Mohr–Coulomb and paraboloidal yield functions, the primary stress invariants were screened as $\{I_1, J_2\}$ in advance to focus on the derivation of exact yield function. Since the data set of Tresca and Mohr–Coulomb function is dependent on θ of Haigh–Westergaard coordinates, $\cos\theta$ and $\sin\theta$ are additionally considered as inputs of symbolic data mining. As far as the fitness function is concerned, the total fitness is composed identically to Eq. (6.2) except the Mohr–Coulomb yield

function of which the fitness function is composed of the addition of MSEs. The symbolic regressions successfully reproduce the Tresca and Mohr–Coulomb yield functions up to 3% dispersion, and paraboloidal yield function up to 30% dispersion. The involvement of the artificial error in the case of Tresca and Mohr–Coulomb results in the difficulty of accurate symbolic data mining compared to the other cases. It might be attributed to the non–smooth characteristics of yield functions since the surfaces display sharp corners depending on θ. The mined functions are represented in Table 6.1 and compared with exact solutions in Figs. 6.1(e)–6.1(j).

It is of worth to identify the mined functions under the error where the symbolic data mining fail to reproduce the considered classical yield functions. The mined functions for the Drucker–Prager, Mohr–Coulomb, and paraboloidal yield functions under arbitrary dispersions of 30%, 20%, and 40% are represented in Fig. 6.2 and Table 6.1. The applied error leads to the minor change of the surface based on the considered yield function or even dramatic change of shape of surface. These observation suggests a possibility of mining better yield function than existing functions based on the considered data set.

6.2. Development of data–driven yield function

6.2.1. MD characterizations on evolution of yield surface

In this section, the evolution of yield surface of the epoxy polymer is investigated by MD simulations considering their extremely high strain rate, which has been a limitation in that the constitutive responses directly derived from the simulations cannot be compared with the experimental results[20,23]. Thus, a mapping method of yield surface from MD strain rate to quasi–static condition is proposed in this section to calibrate the influence of the strain rate discrepancy.

As a first step to construct the quasi–static yield surface, the yield surface evolution of epoxy polymer was evaluated from the multiaxial deformation simulations. Fig. 2.9 exhibits the typical deformation simulations with an atomistic unit cell and the representative constitutive response of multiaxial deformations. The stress states of total 450 stress–strain profiles under the strain rate of $10^{8.5}$/s were examined under various loading paths for establishment of the yield surface. Initial and subsequent yield surfaces were build based on the yield points derived from the effective stress–effective strain profiles and shown in Fig. 6.3(a). Obtained yield surfaces of considered epoxy are isotropically evolved with increasing equivalent plastic strain. The evolution of yield surface shows minor change after the equivalent plastic strain of about 0.01, since the considered epoxy system is relatively ductile than other typical epoxies[74,75,100]. One thing to be noted is that the extent of hardening is especially strong under the biaxial compressive

deformations compared to the other loading paths. Moreover, the variation of principal stresses is also evident within the biaxial compression deformations.

The basic concept of the calibration method is based on the normalized yield surface. The yield surface is normalized by the given yield stress to focus on the general shape of the surface, which has been widely considered for the comparison of the yield surfaces of the materials that display different strengths[101–103]. The normalization requires the characterization of the yield function which consists of the compressive and tensile stresses as:

$$\Phi\left(\boldsymbol{\sigma}, \sigma_c(\dot{\varepsilon}), \sigma_t(\dot{\varepsilon})\right)=0. \tag{6.3}$$

That is, the characterized nonlinear relationship between yield stress and strain rate even up to the MD strain rate condition is required, which can be investigated by several ways using the classical yielding theory[23] and temperature acceleration approach[20].

The overall scheme to establish the quasi–static yield surface is shown in Fig. 6.3(b). Once the compressive and tensile yield stresses of MD and quasi−static conditions are characterized, each stress state of the yield surface under MD strain rate is mapped into the quasi–static condition by the yield stress ratio between MD and quasi–static conditions. The yield stress ratio are determined by four different combinations of compressive and tensile yield stresses depending on their quadrant since the yield function is severely dependent on both yield stresses. This approach assumes that the yield surfaces under the different strain rate conditions are self–similar each other at equal equivalent plastic strain. As far as the variation of the stress states is concerned, the distribution of the stress states

is proportionally decreased as the strain rate is decreased corresponding to the considered nonlinear relation between yield stress and strain rate.

Considering the data set in Fig. 6.3(a), the normalized yield surfaces are obtained with different equivalent plastic strains in Fig. 6.3(c). Since the yield points are isotropically evolved the normalized yield surfaces exhibit similar shape one another. It is worth to note that the distribution of data points within biaxial compressions is fairly large in case of the equivalent plastic strain of 0.01 (blue circles), owing to the influence of the inherent initial variation of the yield stresses in Fig. 6.3(a). This observation confirms that the characteristics of yield surface of MD condition are generally reflected into the quasi–static yield surface by considered mapping method. Considering the quasi–static hardening profiles that derived by previous study[104], the evolution of yield surface under quasi–static condition is finally established in Fig. 6.3(d).

The proposed mapping method was verified in Figs. 6.3(e) and 6.3(f) by investigating the suggested assumption that self–similarity of the yield surfaces is observed under the different strain rate conditions. It was observed whether there is difference between quasi–static solutions derived from different effective strain rates of $10^{9.5}$/s and $10^{8.5}$/s. As expected, the difference of strain rates results in the different size of envelope of the yield surface. However, the size difference of the yield surface does not lead to the different quasi–static surfaces. It was observed in Fig. 6.3(f) that the quasi–static yield surfaces constructed by the identical quasi–static constitutive law exhibit similar shape and size each other, revealing that the considered self–similarity is reasonable.

6.2.2. Construction of data–driven yield function

Based on the evolution of quasi–static yield surface, the constrained symbolic regression was performed to derive an optimized yield function for the epoxy. In order to properly consider the evolution behavior of yield surfaces, the fitness function is composed of multiplication of each sub–fitness function which is defined by MSE function. The overall fitness function consists of a sub-fitness function for the constraint condition and yield surfaces, according to the evolution of equivalent plastic strain, as shown in Fig. 6.3(d) as:

$$fitness = fitness_1 \cdot fitness_2, \tag{6.4}$$

where $fitness_1$ is sub–fitness function to impose constraint function and $fitness_2$ is sub–fitness function defined by the error between prediction function and MD data set. $fitness_1$ is defined to impose penalty under the range of constraint violation which is judged by MSE function as:

$$fitness_1 = \begin{cases} MSE_1, & MSE_1 < C_1 \\ C_2 \cdot (MSE_1)^2, & \text{else} \end{cases}, \tag{6.5}$$

where C_1 is a criterion coefficient for constraint condition and C_2 is a coefficient that controls a degree of penalty depending on the MSE. $fitness_2$ is also defined to consider the all of errors between the MD data and prediction function under different equivalent plastic strains by:

$$fitness_2 = fitness_2|_{\varepsilon_{eq}^p=0} \times fitness_2|_{\varepsilon_{eq}^p=0.005} \times \cdots \times fitness_2|_{\varepsilon_{eq}^p=0.03}, \tag{6.6}$$

where $fitness_2|_{\varepsilon_{eq}^p}$ denotes the sub–fitness measured by the MSE under arbitrary equivalent plastic strain. It is defined by the identical penalty function of Eq. (6.5) as follows:

$$fitness_2|_{\varepsilon_{eq}^p} = \begin{cases} MSE_2, & MSE_2 < C_3 \\ C_4 \cdot (MSE_2)^2, & \text{else} \end{cases}, \tag{6.7}$$

where, similar to the coefficients of $fitness_1$, C_3 is a criterion coefficient for the application of penalty and C_4 is a coefficient that controls a degree of penalty depending on the MSE. The contribution of each sub–fitness function can be controlled by adjusting the coefficients. In the present study, C_1, C_2, C_3, and C_4 were set to $2.5 \cdot 10^{-2}$, 10^6, $2.5 \cdot 10^{-1}$, and 10^6 respectively.

The constraint condition that is applied by the sub–fitness function $fitness_1$ is defined to consider that the mined yield function should be able to pass through the stress states corresponding to the considered 1–dimensional yields as is the symbolic data mining of classical yield functions. The sub–fitness function $fitness_2$ is defined to represent the fitness with the input MD data set corresponding to the evolution of yield surface in Fig. 6.3(d). In this work, the five snapshots of subsequent yield surfaces under different equivalent plastic strains are considered. These snapshots play a role like extracted interpolation points from the whole post–yielding response for the development of the yield function. Therefore, the sub–fitness, $fitness_2|_{\varepsilon_{eq}^p}$, calculated based on each snapshot is treated independently by adding penalty when the predicted function is not able to properly describe the considered yield surface. Accordingly the sub–fitness function $fitness_2$

defined by multiplication of $fitness_2|_{\varepsilon_{eq}^p}$ induces that the any violation of the considered criterion among five data sets leads to the huge disadvantage on the total fitness function.

The symbolic regression was performed based on the total fitness function of Eq. (6.4). All candidate functions derived by symbolic data mining are presented by complexity–fitness profiles in Fig. 6.4. Note that the R–squared value (R^2) of Fig. 6.4 is MSE that calculated from the deviation between candidate function and all of considered MD data set. The fitness of the candidates of the yield function is decreased as the expressional complexity increases up to the complexity of about 40 and, after that, maintained although the expressional complexity increases. In order to find out appropriate yield function for the considered multi–axial hardening behavior, the candidates were filtered based on the constraint condition, fitness (sub–fitness function $fitness_2$), and expressional complexity. Among the candidates, the models satisfying the conditions that $fitness_1 < 0.025$; $fitness_2 < 0.25^5$; and $Complexity < 80$ were selected and represented by red symbols in Fig. 6.4(a). The filtered candidates were again validated whether the candidate function always could have real solutions for $(\sigma_1, \sigma_2, \sigma_3)$ under the considered range of 1–dimensional yield stresses. Accordingly, 24 candidates for the data–driven yield function were selected and presented by the yellow–green symbols in Fig. 6.4(b). Among these candidates, the yield function that exhibited the best performance and concise functional form was finally chosen as the data-driven yield function to be implemented in finite-element analysis. The expressions for the data-driven yield function, including the 2nd highest R^2-valued function and most concise function (the lowest complexity), are

shown and compared with the classical functions in Table 6.2

6.2.3. Validation of the mined yield function

The data–driven yield function was validated with input data set and compared with the Drucker–Prager and paraboloidal yield functions in Fig. 6.5. When comparing the yield surfaces of three yield functions, all of the surfaces nearly overlap at the stress states corresponding to the uniaxial yielding due to the applied constraint condition. It is attributed to the conservative coefficient criterion C_1 set to only 2.5 % during the symbolic regression, which results in the almost identical estimation of the yield surface in the second and fourth quadrants. This constraint mainly allows the change of prediction of data–driven yield function in the vicinity of biaxial deformations. When focusing on the biaxial deformations, the estimation of yielding under biaxial compression exhibits quite different surfaces in all of equivalent plastic strains; the present data–driven yield surface displays much larger envelope compared to the conical and paraboloidal yield surfaces. In particular, the paraboloidal yield surface fairly underestimates the stress states of biaxial deformations compared to the present data–driven model. The shape change of data–driven model leads to the improved fitness with the data set; the R^2 values of the data–driven, Drucker–Prager, and paraboloidal functions are 0.8354, 0.8167, and 0.5969 respectively.

The data–driven yield surface was also validated with the experimental result of plain strain compression tests which was previously performed by Haba et al.[100]. In order

to estimate stress states of biaxial compression, the experimental yield points corresponding to about 0% and 1% of equivalent plastic strain are plotted together in Fig. 6.5. It is observed that the experimental yield points are better described by the present data–driven model, being out of conical and paraboloidal yield surfaces.

6.3. Constitutive modeling based on data–driven yield function

The constitutive model of epoxy was developed by the present data–driven yield function following the overall scheme for numerical time integration based on the previous works of Melro et al. and van der Meer[56,96]. Stress evaluation of considered epoxy is carried out by the general return mapping scheme[105,106]. The stress state is estimated by assuming elastic trial stress as:

$$\boldsymbol{\sigma}_{n+1}^{tr} = \boldsymbol{\sigma}_n + \boldsymbol{D}^e : \Delta\boldsymbol{\varepsilon}, \tag{6.8}$$

where σ_{n+1}^{tr} and σ_n are trial stress at time $n+1$ and stress at time n respectively, $\boldsymbol{D}^e$ is the fourth order isotropic elasticity tensor, and $\Delta\boldsymbol{\varepsilon}$ is strain increment corresponding to the time interval. At the end of the return mapping procedure, the stress at time $n+1$ is evaluated by:

$$\boldsymbol{\sigma}_{n+1} = \boldsymbol{\sigma}_{n+1}^{tr} - \boldsymbol{D}^e : \Delta\boldsymbol{\varepsilon}^p, \tag{6.9}$$

where $\Delta\boldsymbol{\varepsilon}^p$ is plastic strain increment characterized by the flow rule. Elasto–plastic behavior of considered epoxy polymer is modelled using the present data–driven yield function. The consistency condition from the present yield function can be written as

follows:

$$\Phi(\boldsymbol{\sigma},\sigma_c,\sigma_t)=\sqrt{\frac{J_2}{\zeta_s^2}}\left(1.855\sigma_c+1.732\sigma_t-30.4\right)+0.0149{\sigma_t}^2-2.087\sigma_c\sigma_t+1.998\sigma_c+ \\ 15.9\sigma_t+\frac{I_1}{\zeta_p}(\sigma_c-\sigma_t)=0. \tag{6.10}$$

A non–associative flow rule is used to correctly consider the volumetric deformation in constitutive modeling with the flow potential as follows:

$$g=\sigma_{vm}^2+\alpha p^2, \tag{6.11}$$

where $\sigma_{vm}=\sqrt{3J_2}$ is the von Mises equivalent stress and α is a material parameter for the contribution of volumetric deformation on the plastic flow. The flow rule is represented with the flow potential, g as follows:

$$\dot{\boldsymbol{\varepsilon}}^p=\dot{\gamma}\frac{\partial g}{\partial \boldsymbol{\sigma}}, \tag{6.12}$$

where $\dot{\gamma}$ denotes the time derivative of the plastic multiplier. By substituting Eq. (6.11) into Eq. (6.12), the increment of plastic strain is written as:

$$\Delta\varepsilon^p=\Delta\gamma\left(3\boldsymbol{S}+\frac{2}{9}\alpha\boldsymbol{I}_1\right). \tag{6.13}$$

The parameter α related to the plastic Poisson's ratio ν^p is written as follows:

$$\alpha=\frac{9}{2}\frac{1-2\nu_p}{1+\nu_p}. \tag{6.14}$$

The increment in equivalent plastic strain is defined by the plastic strain as follows:

$$\Delta\varepsilon_{eq}^p=\sqrt{k\Delta\boldsymbol{\varepsilon}^p:\Delta\boldsymbol{\varepsilon}^p}=\Delta\gamma\sqrt{k\boldsymbol{M}:\boldsymbol{M}}, \tag{6.15}$$

where k is $1/(1+2\nu_p^2)$ and $\boldsymbol{M}$ is the direction of plastic flow shown in Eq. (6.13) as:

$$M = \frac{3\boldsymbol{S}^{tr}}{\zeta_s} + \frac{\frac{2}{9}\alpha I_1^{tr}\boldsymbol{I}}{\zeta_p}. \tag{6.16}$$

The stress is evaluated at the end of the return mapping procedure with characterized increment of plastic multiplier as:

$$\boldsymbol{\sigma} = \frac{\boldsymbol{S}^{tr}}{1+6G\Delta\gamma} + \frac{\frac{1}{3}I_1^{tr}\boldsymbol{I}}{1+2K\Delta\gamma} = \frac{\boldsymbol{S}^{tr}}{\zeta_s} + \frac{\frac{1}{3}I_1^{tr}\boldsymbol{I}}{\zeta_p}, \tag{6.17}$$

where G is shear modulus and K is bulk modulus of the considered material. Then, the consistency condition of Eq. (6.10) is reduced to nonlinear function of single variable $\Delta\gamma$ from Eqs. (6.15) and (6.16). This nonlinear equation is solved by Newton–Raphson iteration scheme at every time step. This iteration scheme only allows for thermodynamically admissible solution $\Delta\gamma > 0$. The details of implementation of Newton–Raphson scheme is shown in Table 6.3.

The consistent tangent operator is derived by taking derivative of stress from Eq. (6.16) as follows:

$$\frac{\partial\boldsymbol{\sigma}}{\partial\boldsymbol{\varepsilon}} = \frac{1}{\zeta_s}\frac{\partial\boldsymbol{S}^{tr}}{\partial\boldsymbol{\varepsilon}} + \frac{\boldsymbol{I}}{3\zeta_p}\frac{\partial I_1^{tr}}{\partial\boldsymbol{\varepsilon}} - \frac{\boldsymbol{S}^{tr}}{\zeta_s^2}6G\frac{\partial\Delta\gamma}{\partial\boldsymbol{\varepsilon}} - \frac{I_1^{tr}\boldsymbol{I}}{3\zeta_p^2}2K\alpha\frac{\partial\Delta\gamma}{\partial\boldsymbol{\varepsilon}}, \tag{6.18}$$

In order to obtain fully characterized consistent tangent operator, the derivative of increment of plastic multiplier with respect to the strain is needed. Since there is no explicit expression, this relationship should be obtained by the derivative of consistency condition. The final expression for the consistent tangent operator is shown as follows:

$$\frac{\partial\boldsymbol{\sigma}}{\partial\boldsymbol{\varepsilon}} = \beta\boldsymbol{I}_4^s + (\phi - \frac{\beta}{3})\boldsymbol{I}\boldsymbol{I} - \rho\boldsymbol{S}^{tr}\boldsymbol{I} - \chi\boldsymbol{S}^{tr}\boldsymbol{S}^{tr} - \psi\boldsymbol{I}\boldsymbol{S}^{tr} - \omega\boldsymbol{S}^{tr}\boldsymbol{E} - \xi\boldsymbol{I}\boldsymbol{E}, \tag{6.19}$$

where $\boldsymbol{I}_4^s$ is the deviatoric fourth–order identity tensor, $\boldsymbol{E}$ is the derivative of equivalent plastic strain with respect to strain tensor, $\boldsymbol{E} \equiv \frac{\partial \varepsilon_{eq}^p}{\partial \boldsymbol{\varepsilon}}$. The constants of Eq. (6.19) are given as:

$$\beta = \frac{2G}{\zeta_s}, \quad \phi = \frac{K}{\zeta_p} - \frac{2K^2 \alpha I_1^{tr}(\sigma_c - \sigma_t)}{\eta \zeta_p^3}, \quad \rho = \frac{18KG(\sigma_c - \sigma_t)}{\eta \zeta_s^2 \zeta_p},$$
$$\chi = \frac{6G^2}{\eta \zeta_s^3 \sqrt{J_2^{tr}}}\left(1.855\sigma_c + 1.732\sigma_t - 30.4\right), \tag{6.20}$$
$$\psi = \frac{2KG\alpha I_1^{tr}}{3\eta \zeta_s \zeta_p^2 \sqrt{J_2^{tr}}}\left(1.855\sigma_c + 1.732\sigma_t - 30.4\right), \quad \omega = \frac{6G\hat{H}}{\eta \zeta_p^2}, \quad \xi = \frac{2K\alpha I_1^{tr} \hat{H}}{3\eta \zeta_p^2},$$

where $\hat{H}$ is the derivative of yield function with respect to equivalent plastic strain $\hat{H} \equiv \frac{\partial \Phi}{\partial \varepsilon_{eq}^p}$.

6.4. Finite element analysis: one–element mesh validations

The deformation simulations under tension, compression, shear, and bi–compression were performed with UMAT user subroutine of commercial finite element analysis software, ABAQUS. In order to validate the constitutive model based on the data–driven yield function, the constitutive model based on the paraboloidal yield function[56] was also examined under equal conditions. For the implementation of the constitutive model, the compressive and tensile hardening profiles including modulus and Poisson's ratios that extracted from the work of Park et al. were used as inputs of the simulations[104]. Since the

paraboloidal and data–driven yield functions exhibit only different behaviors under the biaxial deformations, the numerical prediction of compression, tension, and shear tests should denote nearly identical responses, and conversely the prediction of bi–compression test should denote the different responses between the two yield function.

The comparison of one–element deformation tests between the data–driven and paraboloidal yield functions is shown in Fig. 6.6. The numerical prediction of compression, tension, and shear is shown in Fig. 6.6(a) and bi–compression is shown in Fig. 6.6(b) respectively. Note that the bi–compressive stress denotes axial stress component only. The prediction profiles from both yield functions are almost identical under the tension, compression, and shear, which results from the closely similar hardening behavior under these loading paths of yield surfaces as seen in Fig. 6.6. It is because both yield surfaces consistently follow the 1–dimensional post–yielding behavior by the imposed constraint condition of Eq. (6.5). As far as the prediction of bi–compressive loading is concerned, the stress of the present data–driven function is more optimized for the yield data set by the application of Eq. (6.6), displaying higher value than that of paraboloidal yield function as can be seen in Fig. 6.6.

6.5. Characteristics of data–driven yield function

The data–driven yield function was formulated by the symbolic data mining considering the multi–axial yield behavior of epoxy polymer. The function mining was

performed based on the ability of constrained symbolic regression on the screening of primary stress invariants under severe error involved and optimization of functional structure. It was confirmed by the mining examples of the classical yield functions that it is possible to develop the data–driven yield functions just by the yield data set simultaneously reflecting the yielding nature of the materials. The examples also suggest an importance of application of constraint condition which enables the robust prediction of yield function even with severely dispersed data set.

It is necessary to specifically focus on the functional expressions of the data–driven yield function of epoxy. Considering the mined yield functions in Table 6.2, all of functions consist of linear combination between terms for $\sqrt{J_2}$ and I_1 denoting conically–shaped surface. The derivation of stress invariant set consisting of $\sqrt{J_2}$ and I_1 instead of J_2 and I_1 suggests that the considered MD data set is better described by the conically–shaped yield function than paraboloidally–shaped yield function. It can be inferred that the paraboloidally–shaped candidate functions might have difficulty in describing the bi–compressive hardening behavior of epoxy, being eliminated during the symbolic data mining.

When focusing on the present data–driven model (model 1 in Table 6.2), it can be found out that the functional structure of the mined yield function is quite similar to the classical functions. The terms consisting of the stress invariants $\sqrt{J_2}(1.855\sigma_c + 1.732\sigma_t)$ and $I_1(\sigma_c - \sigma_t)$ are similar to the Drucker–Prager and paraboloidal functions (see Eqs. (1.3) and (1.5)). The term to define an elastic deformation

range $-2.087\sigma_c\sigma_t$ also denotes identical functional structure with the Drucker–Prager and paraboloidal functions. There is also close correlation for the determined coefficients with the classical functions; the coefficients for $\sqrt{J_2}\sigma_c$ and $\sqrt{J_2}\sigma_t$ are 1.855 and 1.732 respectively being close to the coefficient of the Drucker–Prager yield function, $\sqrt{3}$, while the coefficient of $I_1(\sigma_c-\sigma_t)$ is unity. The determination of the coefficients of $\sqrt{J_2}$ and I_1 is of primary importance since the ratio between them represents the pressure sensitivity of the yielding of materials. When considering Haigh–Westergaard stress space, the magnitude of hydrostatic stress and deviatoric stress vectors is described by:

$$\rho=|\boldsymbol{\rho}|=\sqrt{3}\sigma_m=I_1/\sqrt{3}, \qquad S=|\mathbf{S}|=\sqrt{2J_2}. \tag{6.21}$$

Then, the ratio between S and ρ denotes how much the deviatoric stress varies with a change of hydrostatic pressure. The ratio of both functions is represented respectively by:

$$\left[\frac{d\rho}{dS}\right]_{\text{mined}}=\frac{-\sqrt{6}(\sigma_c-\sigma_t)}{(1.855\sigma_c+1.732\sigma_t-30.4)}, \tag{6.22}$$

$$\left[\frac{d\rho}{dS}\right]_{\text{Drucker-Prager}}=\frac{-\sqrt{6}(\sigma_c-\sigma_t)}{\sqrt{3}(\sigma_c+\sigma_t)}. \tag{6.23}$$

Although additional terms in the denominator of the mined model are involved, the term $1.855\sigma_c+1.732\sigma_t$, which closely correlated to the $\sqrt{3}$, mainly contribute to a pressure–sensitivity of epoxy as in the case of the Drucker–Prager function. Furthermore, the coefficients for the term, $-2.087\sigma_c\sigma_t$ representing the contribution of 1–dimensional yield stresses on the finite elastic range is also optimized similarly to the Drucker–Prager yield function. These similar functional forms and coefficients imply that the symbolic regression formulated the yield function closely following the feature of the classical yield

function despite of absence of preliminary knowledge on the classical function.

On the basis of these similarities, the modifications were performed to optimize the data–driven function corresponding to the yielding nature of the considered epoxy by the terms such as $-30.4\sqrt{J_2}$, $0.0149\sigma_t^2$, $1.998\sigma_c+15.9\sigma_t$, and $1.998\sigma_c+15.9\sigma_t$. These terms might contribute to the proper description of distinctive multi–axial hardening behavior of considered epoxy especially for the bi–compression loading.

When it comes to the new formulation of yield function, it is necessary to evaluate the candidate function based on the desirable features of the yield function[53]. Especially for amorphous polymers, these are:

1. *Description of finite extent of elastic range;*
2. *Pressure–dependency;*
3. *Deviation between compressive and tensile yield stresses;*
4. *Smoothness of the yield surface;*
5. *Convexity;*
6. *Simple expression.*

The present data–driven yield function can be evaluated by above features; (1) the model can represent the finite extent of elastic range by the terms $-2.087\sigma_c\sigma_t$, $0.0149\sigma_t^2$, and $1.998\sigma_c+15.9\sigma_t$; (2) the pressure–dependency is described by the first stress invariant with a sensitivity of Eq. (6.22); (3) the mined yield function consists of both compressive and tensile yield stresses to describe the uniaxial yielding separately in stress space; (4) since the model is conically–shaped surface the smoothness is guaranteed except

the apex; (5) convexity is guaranteed on the conically–shaped surface; (6) expressional complexity is considered during the symbolic data mining.

The present data–driven yield function that properly denotes the yield behavior of the considered epoxy has been successfully implemented in the constitutive model. The two questions in the introduction are successfully answered by the symbolic mining for classical yield functions and the development of the constitutive model by the data–driven yield function. Accordingly, it was confirmed that the failure behaviors of the materials can be simulated by concentrating on their own nature of plasticity using the data–driven yield function overcoming a disagreement with the existing yield functions.

6.6. Summary

The main contribution of this chapter is to propose data–driven multiscale framework for the elasto–plastic constitutive modeling that can reflect the unique multiaxial yielding and post–yielding behaviors of various materials even for unknown plastic deformation characteristics. The constitutive model is developed based on the data–driven yield function of the target material instead of classical yield function which is naturally formulated from the yield data set by constrained symbolic regression, one of the machine learning technique. In this procedure, the application of the constraint equation can play an important role in the reliable prediction of mathematical expression of the mined model. In particular, the data–driven yield function developed by the present approach can adequately consider the intrinsic multi–axial hardening of yield surface, which is probably impossible with the classical yield functions. The developed yield function properly predict the bi–compressive yielding behaviors which exhibit much larger envelope compared to the classical yield functions. The present framework can be extended to various future works by applying to various materials for the accumulation of database, validation of the existing yield functions, or characterizing unrevealed nature of plasticity.

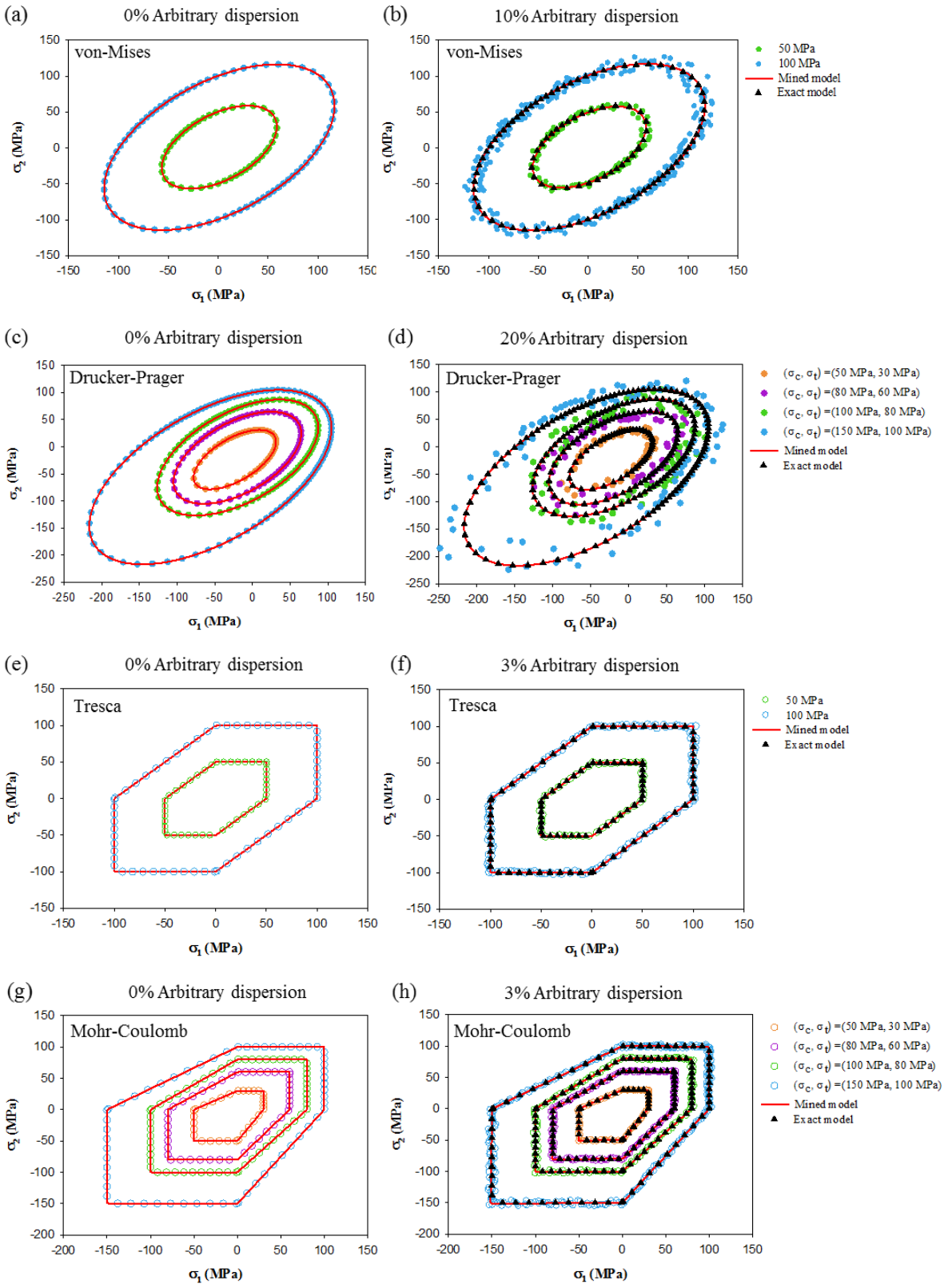
(a)
0% Arbitrary dispersion
von-Mises
(b)
10% Arbitrary dispersion
von-Mises
50 MPa
100 MPa
Mined model
Exact model
(c)
0% Arbitrary dispersion
Drucker-Prager
(d)
20% Arbitrary dispersion
Drucker-Prager
(σc, σt) =(50 MPa, 30 MPa)
(σc, σt) =(80 MPa, 60 MPa)
(σc, σt) =(100 MPa, 80 MPa)
(σc, σt) =(150 MPa, 100 MPa)
Mined model
Exact model
(e)
0% Arbitrary dispersion
Tresca
(f)
3% Arbitrary dispersion
Tresca
50 MPa
100 MPa
Mined model
Exact model
(g)
0% Arbitrary dispersion
Mohr-Coulomb
(h)
3% Arbitrary dispersion
Mohr-Coulomb
(σc, σt) =(50 MPa, 30 MPa)
(σc, σt) =(80 MPa, 60 MPa)
(σc, σt) =(100 MPa, 80 MPa)
(σc, σt) =(150 MPa, 100 MPa)
Mined model
Exact model
σ1 (MPa)
σ2 (MPa)

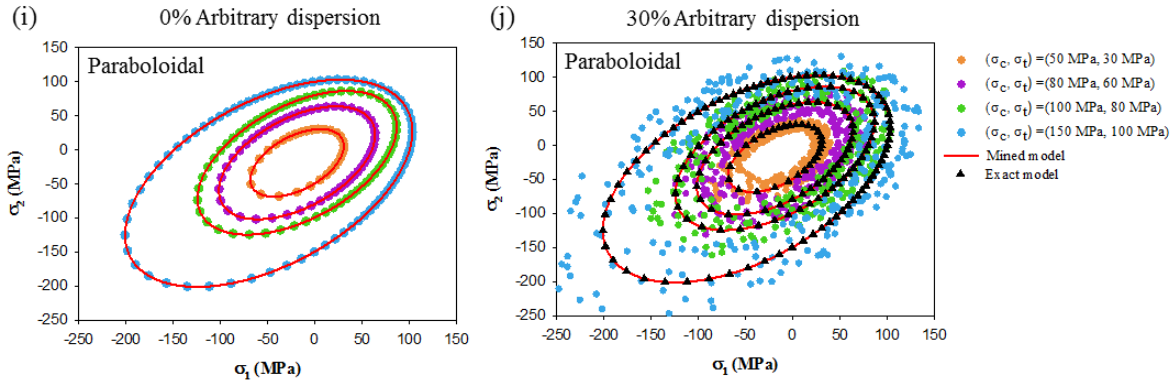

Fig. 6.1. Reproduced classical yield functions by symbolic data mining under various artificial errors: (a) 0% arbitrary dispersion, von–Mises function, (b) 10% arbitrary dispersion, von–Mises function, (c) 0% arbitrary dispersion, Drucker–Prager function, (d) 20% arbitrary dispersion, Drucker–Prager function, (e) 0% arbitrary dispersion, Tresca function, (f) 3% arbitrary dispersion, Tresca function, (g) 0% arbitrary dispersion, Mohr–Coulomb function, (h) 3% arbitrary dispersion, Mohr–Coulomb function, (i) 0% arbitrary dispersion, paraboloidal function, and (j) 30% arbitrary dispersion, paraboloidal function. The hollow data points in each figure denote the subject training data set and the black dots denote the response of the exact yield functions. The red solid line exhibits the responses of the mined models.

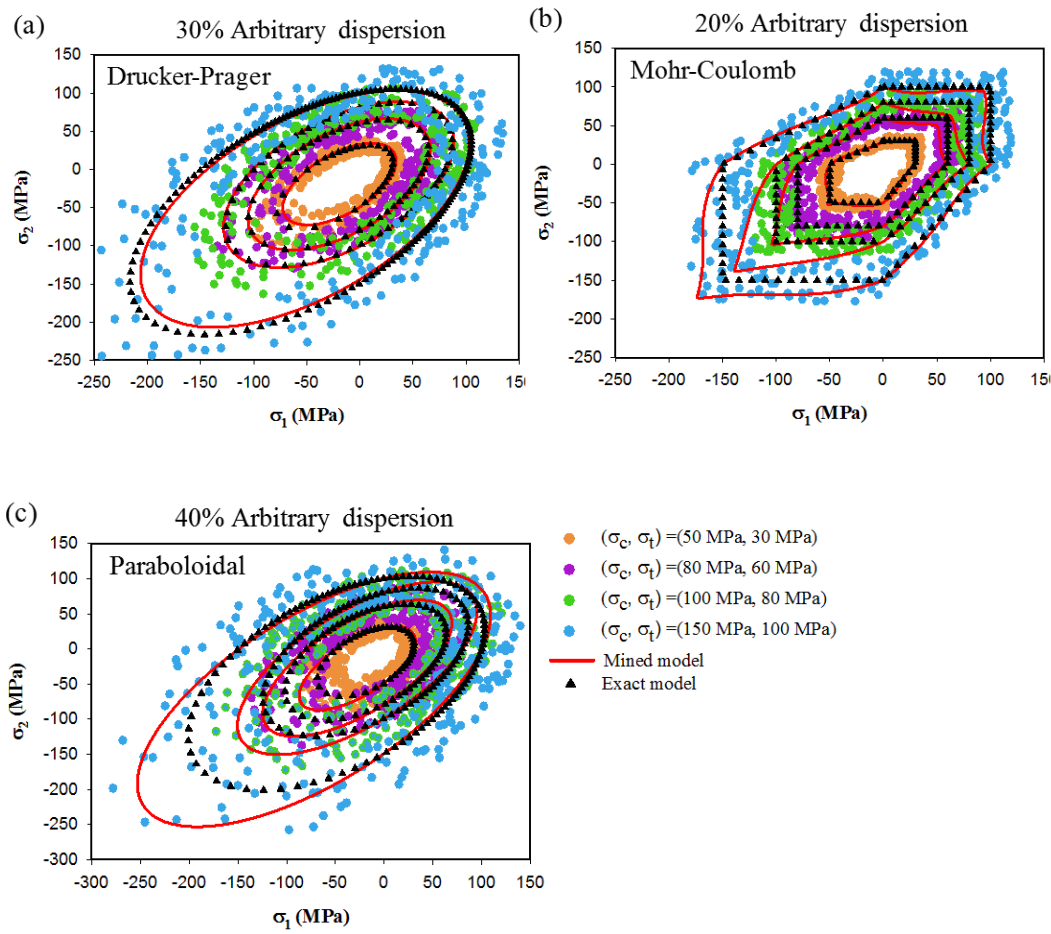

Fig. 6.2. Mined yield surfaces under severe error: (a) Drucker–Prager, 30% arbitrary dispersion, (b) Mohr–Coulomb, 20% arbitrary dispersion, and (c) paraboloidal, 40% arbitrary dispersion.

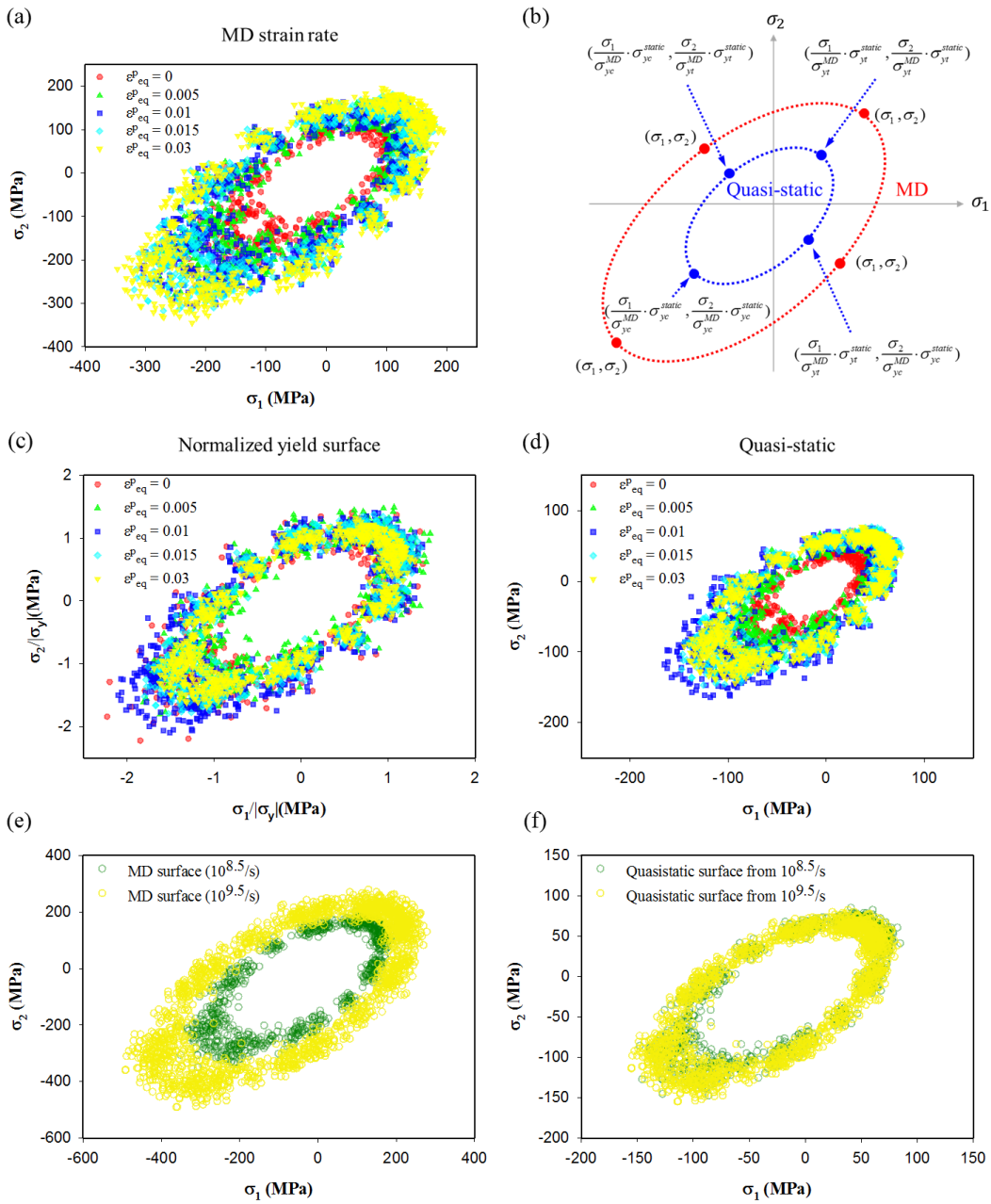

Fig. 6.3. Illustration for the construction of quasi-static yield surface from the MD yield surface: (a) yield surface evolution with increment of equivalent plastic strain under MD strain rate condition ($10^{8.5}$/s); (b) proposed scheme to construct a quasi-static yield surface from MD simulations; (c) normalized yield surfaces' evolution with different equivalent plastic strains; and (d) constructed quasi-static yield surfaces with increasing equivalent

plastic strains. Note that the quasi-static stress–strain profiles of a previous study (Park et al.[104]) were used to reconstruct the surfaces. Comparison of (e) the yield surfaces under different strain rates ($10^{9.5}$/s and $10^{8.5}$/s), and (f) quasi-static yield surfaces obtained by proposed mapping method.

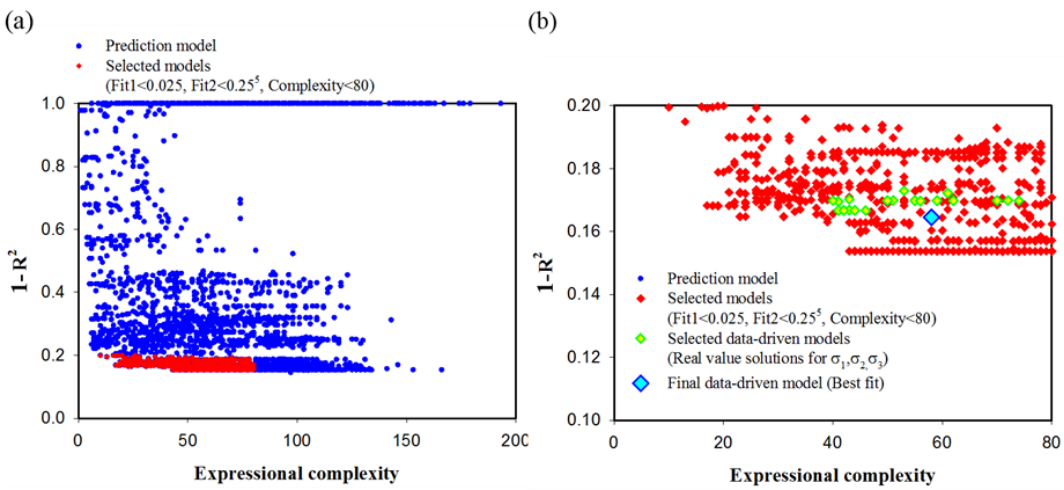

Fig. 6.4. Resulting candidate functions from symbolic regression. Each candidate yield function is shown in the complexity-fitness profile: (a) total and (b) filtered populations. For symbolic data mining, a total of 12,000 populations were randomly produced with multiple runs for model diversity. The mathematical nodes considered in the present study are basic arithmetic symbols, including power.

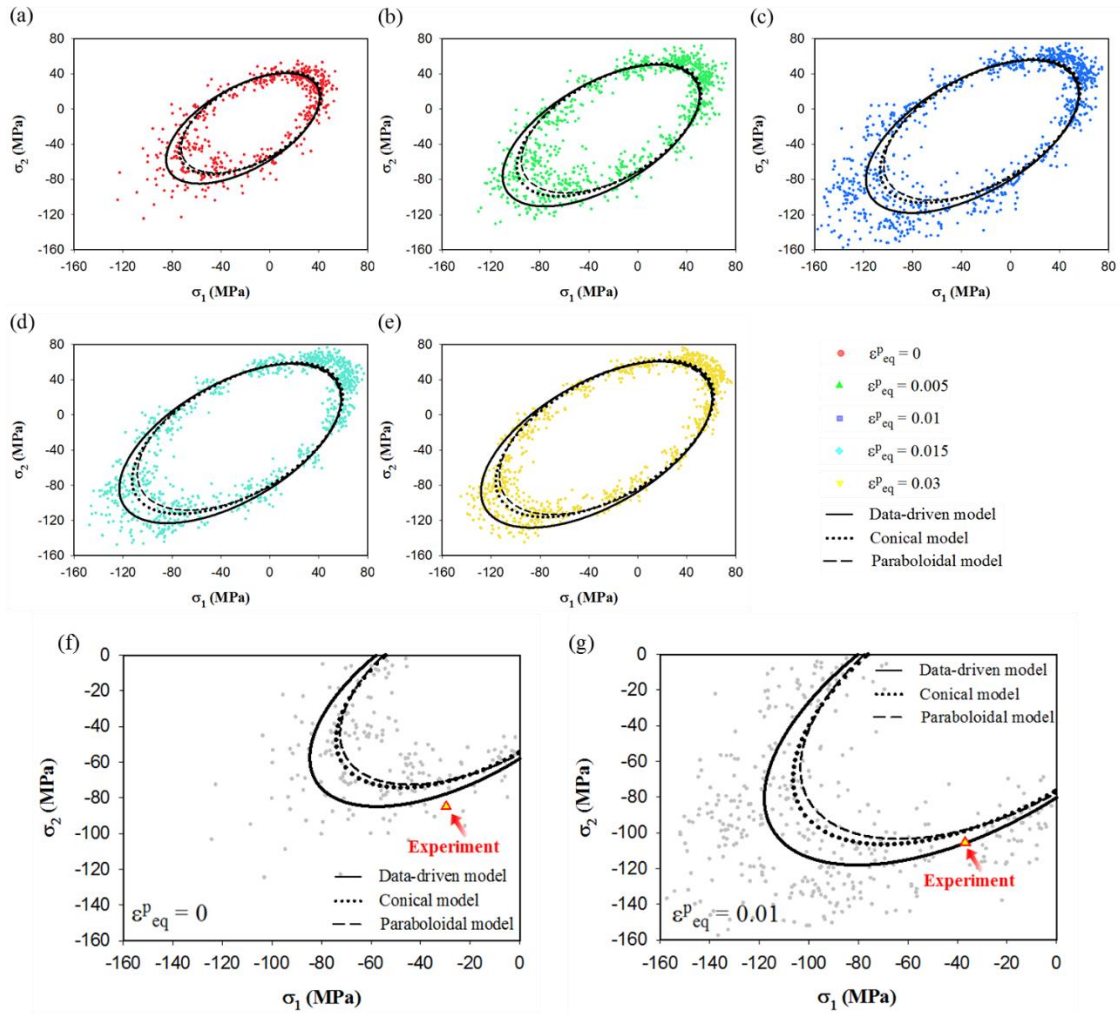

Fig. 6.5. Comparison of the data-driven yield function with the classical yield functions (Drucker–Prager and paraboloidal yield functions) and experimental result. The evaluated equivalent plastic strains are (a) 0, (b) 0.005, (c) 0.01, (d) 0.015, and (e) 0.03. The data-driven, Drucker–Prager, and paraboloidal yield functions are represented by solid, dotted, and dashed lines, respectively (a–g). Validation of the data-driven yield surface with experimental result of Haba et al.[100] with correlated equivalent plastic strain condition: (f) 0, (g) 0.01.

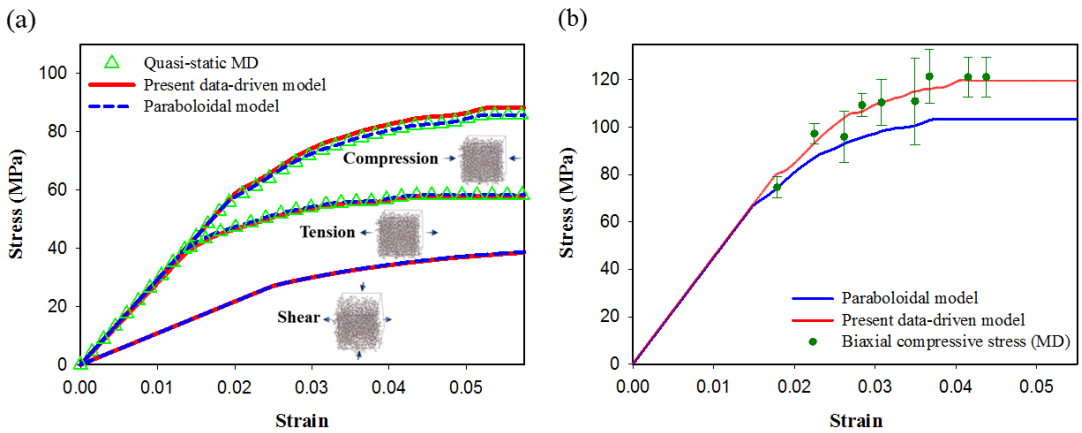

Fig. 6.6. Results of one-element deformation tests under various loading paths: (a) compression, tension, and shear, and (b) bi-compression. The one-dimensional hardening profiles extracted by Park et al.[104] were used for inputs including all other physical properties. The studied Young's modulus, Poisson's ratio, and plastic Poisson's ratio were 2930 MPa, 0.35, and 0.35, respectively.

Table 6.1.

Details of the symbolic data mining for the classical yield functions and the data-driven yield function.

Mined functions	**Input nodes**	**Fixed node**	**Mathematical nodes**	**Population (number of runs)**
von-Mises	$\{I_1, I_2, I_3, J_2, J_3\}$	$\{\sigma_y\}$	$\{+, -, \times, /, \sqrt{\ }, (\ )^2\}$	3,000 (10)
Drucker-Prager (conical)	$\{I_1, I_2, I_3, J_3, \sigma_c, \sigma_t\}$	$\{J_2\}$	$\{+, -, \times, /\}$	3,000 (10)
Tresca	$\{I_1, I_2, I_3, J_2, J_3, \cos\theta, \sin\theta\}$	$\{\sigma_y\}$	$\{+, -, \times, /, \sqrt{\ }\}$	30,000 (100)
Mohr-Coulomb	$\{\sqrt{J_2}, \cos\theta, \sin\theta, \sigma_c, \sigma_t\}$	$\{I_1\}$	$\{+, -, \times, /\}$	200,000 (100)
Paraboloidal	$\{I_1, \sigma_c, \sigma_t\}$	$\{J_2\}$	$\{+, -, \times, /, \sqrt{\ }\}$	3,000 (10)
Data-driven	$\{J_2, \sigma_c, \sigma_t\}$	$\{I_1\}$	$\{+, -, \times, /, \sqrt{\ }\}$	12,000 (5)

Table 6.2

Mined models for von–Mises, Drucker–Prager, Tresca, Mohr–Coulomb, and paraboloidal yield functions by the symbolic regressions.

Yield function	Dispersion	Model	Mined models
von–Mises	0%	a1	$1.732\sqrt{J_2}+5.46\mathrm{e}^{-12}=\sigma_y$
		a2	$0.02J_2+33=\sigma_y$
		a3	$0.07J_2-1.2e^{-5}J_2^2+1.0e^{-4}=\sigma_y$
	10%	b1	$1.684\sqrt{J_2}+2.29=\sigma_y$
		b2	$22J_2^{1/4}-67=\sigma_y$
		b3	$\frac{812.7J_2^{1/4}-45.76J_2+812.70J_2^{3/4}+26522}{\sqrt{J_2}+1}-3929=\sigma_y$
Drucker–Prager	0%	c1	$\sqrt{J_2}(\sigma_c+\sigma_t)+0.5774I_1(\sigma_c-\sigma_t)+1.155\sigma_c\sigma_t+(\sigma_c+\sigma_t)(-1.62e^{-16}I_1-3.64e^{-11})=0$
		c2	$\sqrt{J_2}(\sigma_c+\sigma_t)+0.5774I_1(\sigma_c-\sigma_t)+1.155\sigma_c\sigma_t+(\sigma_c+\sigma_t)(-8.3e^{-16}I_1-4.8e^{-11})=0$
		c3	$\sqrt{J_2}(\sigma_c+\sigma_t)+0.5774I_1(\sigma_c-\sigma_t)+1.155\sigma_c\sigma_t+(\sigma_c+\sigma_t)(-6.7e^{-13}I_1-4.8e^{-9})=0$
	20%	d1	$\sqrt{J_2}(\sigma_c+\sigma_t)+0.5774I_1(\sigma_c-\sigma_t)+1.155\sigma_c\sigma_t+(\sigma_c+\sigma_t)(-5.13e^{-7}I_3(\sigma_c+I_1)+3.09e^{-2})=0$
		d2	$\sqrt{J_2}(\sigma_c+\sigma_t)+0.5774I_1(\sigma_c-\sigma_t)+1.155\sigma_c\sigma_t+(\sigma_c+\sigma_t)(1.7e^{-9}I_2(\sigma_cI_1+I_3-I_1)+1.9e^{-2})=0$
		d3	$\sqrt{J_2}(\sigma_c+\sigma_t)+0.5774I_1(\sigma_c-\sigma_t)+1.155\sigma_c\sigma_t+(\sigma_c+\sigma_t)(-1.1e^{-4}I_2+2.0\mathrm{e}^{-6}I_3(I_1+\sigma_c)+2.6\mathrm{e}^{-8}I_2(I_1\sigma_c+I_3-I_1))=0$
	30%	d4	$0.5\sigma_t-0.077\left(\frac{\sigma_t}{\sigma_c}(\sigma_t-\sigma_c)-(\sigma_c+\frac{I_1}{\sigma_c})\right)+0.3007\frac{I_1}{\sigma_c}(\sigma_t-\sigma_c)+2.3\mathrm{e}^{-4}((\sigma_t-\sigma_c)(I_1-2\sigma_t+\sigma_c))+2.9-\sqrt{J_2}=0$
Tresca	0%	e1	$\sqrt{J_2}(1.732\cos\theta+\sin\theta)=\sigma_y$
	3%	e2	$\sqrt{J_2}(1.732\cos\theta+0.993\sin\theta)+0.203\sqrt{\sin\theta}+0.012=\sigma_y$
Mohr–Coulomb	0%	f1	$3\sqrt{J_2}\sin(\theta+\frac{\pi}{3})\frac{\sigma_c+\sigma_t}{\sigma_c-\sigma_t}+1.732\sqrt{J_2}\cos(\theta+\frac{\pi}{3})+I_1-\frac{3\sigma_c\sigma_t}{\sigma_c-\sigma_t}-4.6e^{-10}=0$
	3%	f2	$2.935\sqrt{J_2}\sin(\theta+\frac{\pi}{3})\frac{\sigma_c+\sigma_t}{\sigma_c-\sigma_t}+1.619\sqrt{J_2}\cos(\theta+\frac{\pi}{3})+I_1-\frac{2.927\sigma_c\sigma_t}{\sigma_c-\sigma_t}+0.28-0.00168(\sigma_c+\sigma_t)^2/((\sigma_c-\sigma_t)\sin(\theta+\frac{\pi}{3}))=0$

	20%	f3	$\sqrt{J_2}+0.1I_1-0.03\sin(\theta+\frac{\pi}{3})+0.048(\sigma_c-\sigma_t)+0.577(\sigma_c-\sigma_t)\cos(\theta+\frac{\pi}{3})$ $-0.25(\sigma_c+\sigma_t)/\sin(\theta+\frac{\pi}{3})-0.0619(\sigma_c+\sigma_t)\cos(\theta+\frac{\pi}{3})/\sin^3(\theta+\frac{\pi}{3})+0.1=0$
Paraboloidal	0%	g1	$0.333I_1\sigma_t-0.333I_1\sigma_c+0.333\sigma_c\sigma_t-J_2=0$
	30%	g2	$0.333I_1\sigma_t-0.333I_1\sigma_c+0.333\sigma_c\sigma_t-4.021e^{-7}-J_2=0$
	40%	g3	$0.301I_1\sigma_t-0.301I_1\sigma_c+0.301\sigma_c\sigma_t+0.033I_1^2-1.3-J_2=0$

Table 6.3

Mined yield functions for the subject epoxy polymer and the classical yield functions. Model 1 was finally selected as the data-driven yield function.

Model	Symbolic regression model	R2
1 (Best)	$\sqrt{J_2}(1.855\sigma_c+1.732\sigma_t-30.4)+0.0149\sigma_t^2-2.087\sigma_c\sigma_t+1.998\sigma_c+15.9\sigma_t+I_1(\sigma_c-\sigma_t)=0$	0.8354
2 (2^{nd} best)	$\sqrt{J_2}(2.002\sigma_c+1.418\sigma_t+60.3\sigma_t/\sigma_c-60.3)-(\sigma_c-\sigma_t)(0.096\sigma_c+0.018\sigma_t)-1.975\sigma_c\sigma_t+21.58(\sigma_c-\sigma_t)+I_1(\sigma_c-\sigma_t)=0$	0.8333
3 (Min. complexity)	$\sqrt{J_2}(1.728\sigma_c+1.674\sigma_t-213.2/\sigma_c)-1.963\sigma_c\sigma_t-1.339(\sigma_c-\sigma_t)+I_1(\sigma_c-\sigma_t)=0$	0.8302
4 (Conical)	$\sqrt{3J_2}(\sigma_c+\sigma_t)+I_1(\sigma_c-\sigma_t)-2\sigma_c\sigma_t=0$	0.8167
5 (Paraboloidal)	$6J_2+2(\sigma_c-\sigma_t)I_1-2\sigma_c\sigma_t=0$	0.5969

Table 6.4.

Algorithm for the implementation of the constitutive model with the data–driven yield function.

(i) Trial stress. Based on the strain increment at t_n:

$$\boldsymbol{\sigma}_{n+1}^{tr} = \boldsymbol{\sigma}_n + \boldsymbol{D}^e : \Delta\boldsymbol{\varepsilon}, \quad \Delta\varepsilon_{eq_{n+1}}^{p^{tr}} = \Delta\varepsilon_{eq_n}^{p},$$

$$\sigma_{c_{n+1}}(\Delta\varepsilon_{eq_{n+1}}^{p^{tr}}) = \sigma_{c_n}(\Delta\varepsilon_{eq_n}^{p}), \sigma_{t_{n+1}}(\Delta\varepsilon_{eq_{n+1}}^{p^{tr}}) = \sigma_{t_n}(\Delta\varepsilon_{eq_n}^{p}).$$

(ii) Check if the stress state is beyond the yield criterion:

$$IF\ \sqrt{J_2^{tr}}\left(1.855\sigma_c + 1.732\sigma_t - 30.4\right) + 0.0149\sigma_t^{\,2} - 2.087\sigma_c\sigma_t + 1.998\sigma_c + 15.9\sigma_t + I_1^{tr}(\sigma_c - \sigma_t) \le 0$$

$$THEN\ \sigma_{n+1} = \sigma_{n+1}^{tr}, \sigma_{c_{n+1}} = \sigma_{c_{n+1}}^{tr}, \sigma_{t_{n+1}} = \sigma_{t_{n+1}}^{tr}.$$

ELSE IF ***retrun mapping algorithm***

- Initial guess for the plastic multiplier, $\Delta\gamma$.

$$\Delta\varepsilon_{eq_{n+1}}^{p} = \sqrt{\frac{1}{1+2\nu_p^{\,2}}}\Delta\gamma\sqrt{\frac{18J_2^{tr}}{\zeta_s^{\,2}} + \frac{4\alpha^2}{27\zeta_p^{\,2}}(I_1^{tr})^2},$$

$$\sigma_{c_{n+1}} = \sigma_c(\Delta\varepsilon_{eq_{n+1}}^{p}), \sigma_{t_{n+1}} = \sigma_t(\Delta\varepsilon_{eq_{n+1}}^{p}),$$

$$\Phi = \sqrt{\frac{J_2^{tr}}{\zeta_s^2}}\left(1.855\sigma_{c_{n+1}} + 1.732\sigma_{t_{n+1}} - 30.4\right) + 0.0149\sigma_{t_{n+1}}^{\,2} - 2.087\sigma_{c_{n+1}}\sigma_{t_{n+1}} + 1.998\sigma_{c_{n+1}} + 15.9\sigma_{t_{n+1}} + \frac{I_1^{tr}}{\zeta_p}(\sigma_{c_{n+1}} - \sigma_{t_{n+1}}).$$

- For Newton–Raphson iteration scheme,

$$\frac{\partial \sigma_c}{\partial \Delta\gamma} = \frac{\partial \sigma_c}{\partial \Delta\varepsilon_{eq}^p}\frac{\partial \Delta\varepsilon_{eq}^p}{\partial \Delta\gamma} = H_c \frac{\partial \Delta\varepsilon_{eq}^p}{\partial \Delta\gamma}, \quad \frac{\partial \sigma_t}{\partial \Delta\gamma} = \frac{\partial \sigma_t}{\partial \Delta\varepsilon_{eq}^p}\frac{\partial \Delta\varepsilon_{eq}^p}{\partial \Delta\gamma} = H_t \frac{\partial \Delta\varepsilon_{eq}^p}{\partial \Delta\gamma},$$

$$\frac{\partial \Delta\varepsilon_{eq}^p}{\partial \Delta\gamma} = \sqrt{\frac{1}{1+2\nu_p^{\,2}}}\left[\sqrt{A} - \frac{\Delta\gamma}{2\sqrt{A}}\left(\frac{216GJ_2^{tr}}{\zeta_s^3} + \frac{16\alpha K I_1^{tr\,2}}{27\zeta_p^3}\right)\right],$$

where A is defined by:

$$A = \frac{18J_2^{tr}}{\zeta_s^{\,2}} + \frac{4\alpha^2}{27\zeta_p^{\,2}}(I_1^{tr})^2.$$

$$\frac{\partial \Phi}{\partial \Delta\gamma} = -\frac{6G\sqrt{J_2^{tr}}}{\zeta_s^{\,2}}(1.855\sigma_c + 1.732\sigma_t - 30.4) - \frac{2K\alpha I_1^{tr}}{\zeta_p^{\,2}}(\sigma_c - \sigma_t)$$
$$+ \frac{\partial \Phi}{\partial \varepsilon_{eq}^p}\frac{\partial \varepsilon_{eq}^p}{\Delta\gamma}.$$

where $\frac{\partial \Phi}{\partial \varepsilon_{eq}^p}$ can be written as:

$$\frac{\partial \Phi}{\partial \varepsilon_{eq}^p} = \frac{\sqrt{J_2^{tr}}}{\zeta_s}\left(1.855H_c + 1.732H_t\right) + 0.03\sigma_t H_t - 2.087(H_c\sigma_t + \sigma_c H_t)$$
$$+1.998H_c + 15.9H_t + \frac{I_1^{tr}}{\zeta_p}(H_c - H_t).$$

Thus, the plastic multiplier that satisfies $\Phi = 0$ is derived iteratively by:

$$\Delta\gamma = \Delta\gamma - \frac{\Phi}{\partial\Phi \big/ \partial\Delta\gamma}.$$

(iii) Update stress tensor and plastic strain tensor with characterized plastic multiplier:

$$\boldsymbol{\sigma}_{n+1} = \frac{\boldsymbol{S}_{n+1}^{tr}}{1+6G\Delta\gamma} + \frac{p_{n+1}^{tr}}{1+2K\alpha\Delta\gamma}, \quad \Delta\varepsilon^p = \Delta\gamma\left(3\boldsymbol{S} + \frac{2}{9}\alpha\boldsymbol{I}_1\right).$$

(iv) Go to next iteration.

7. Conclusion and Recommendation

In this dissertation, a multiscale framework was developed to investigate plastic behaviors of amorphous polymers without experimental support, which can reveal the microscopic deformation properties of the material. The timescale limitation of classical MD simulations, which has been considered an obstacle for the characterizations of constitutive equations by MD simulations, was overcome based on the relaxation nature of polymers. The obtained constitutive responses were used for achieving further predictions of macroscopic plastic behaviors as compared to the classical methodologies, which only utilize the classical yield criteria for multi-axial deformation behaviors of polymers. To establish 3-dimensional FE models by the derived data set, machine learning was used for the mathematical prediction of yield functions.

The microscopic mechanisms of the plastic deformations were investigated focusing on the energy, stress, and chain conformations during the deformations. In particular, the influence of structural differences that arise from different curing agents was estimated from the perspective of plastic deformations. The results revealed that irreversible folding of the dihedral angle was mainly observed at the benzene rings in the epoxy network, as the plastic deformations were initiated. The folding behaviors led to a different trend in plastic strain accumulations, when the cyclic loadings were applied. The plastic strain of epoxy cured by an aromatic curing agent was accumulated rapidly as compared to that of the epoxy cured by an aliphatic curing agent.

The methods to predict quasi-static constitutive laws were developed using classical yielding theories and polymer kinetics. To predict the scaled constitutive laws at a quasi-static level, the master profiles of yield stress were predicted by two approaches. The first method employs the time and temperature equivalence and sequentially construct the master profile by utilizing the yield slope of the higher temperatures. The second method is to use the 0 K solution of Argon theory and a cooperative model for a proper description of the nonlinear nature of polymer, which yields the corresponding rate and temperature.

The FE model for the plastic deformation behaviors of epoxy polymers was constructed by data-driven constitutive modeling. The data-driven constitutive model was established by generating data-driven yield function, which was predicted from machine learning with the MD data set. The MD data set displays its own envelope at $\sigma_3 = 0$ plane, which is featured by a significantly larger boundary in bi–compressive loading. The subsequent yield surfaces as well as the initial surface were considered in the prediction procedure; this has been not taken into account by previous constitutive modeling techniques. The predicted data-driven yield function thoroughly describes the evolution of the yield surface that is featured by a raw data set, as compared to the existing yield functions (Drucker-Prager and paraboloidal yield functions).

We expect that the machine learning based multiscale framework will be broadly used for the predictions of macroscopic plastic deformations of various polymers by revealing their deformation characteristics more effectively and efficiently than that

obtained with classical FE analysis; this can eventually lead to the formation of a library of amorphous polymer materials. Further, this framework can be extended to other classes of materials such as crystalline polymers, metals, and biomaterials with well–defined methods to identify constitutive responses of those materials.

References

[1] Sharifi, M.; Jang, C.W.; Abrams C.F.; Palmese G.R. Toughened epoxy polymers via rearrangement of network topology. J. Mater. Chem. A, 2014, 2, 16071.

[2] Wan, J.; Bu, Z.-Y.; Xu, C.-J.; Li, B.-G.; Fan, H. Preparation, curing kinetics, and properties of a novel low-volatile starlike aliphatic-polyamine curing agent for epoxy resins. Chem. Eng. J., 2011, 171(1), 357–67.

[3] Ghaemy, M.; Barghamadi, M.; Behmadi, H. Cure kinetics of epoxy resin and aromatic diamines. J. Appl. Polym. Sci., 2004, 94(3), 1049–56.

[4] Unnikrishnan, K.P.; Thachil, E. T. Toughening of epoxy resins Des Monomers Polymer, 2006, 9(2), 129–52.

[5] Bandyopadhyay, A.; Valavala, P. K.; Clancy, T. C.; Wise, K. E.; Odegard, G. M. Molecular modeling of crosslinked epoxy polymers: The effect of crosslink density on thermomechanical properties. Polymer, 2011, 52(11), 2445–52.

[6] Kim, B.; Choi, J.; Yang, S.; Yu, S.; Cho, M. Influence of crosslink density on the interfacial characteristics of epoxy nanocomposites. Polymer, 2015, 60, 186–97.

[7] Elder, R.M.; Andzelm, J.W.; Sirk T.W. A molecular simulation study of glass transition of crosslinked poly(dicyclopentadiene) networks. Chem. Phys. Lett., 2015, 636(16), 103–9.

[8] Li, C.; Strachan, A. Free volume evolution in the process of epoxy curing and its effect on mechanical properties. Polymer, 2016, 97(5), 456–64.

[9] Shenogina, N. B.; Tsige M.; Patnaik S. S.; Mukhopadhyay, S. M. Molecular modeling approach to prediction of thermo-mechanical behavior of thermoset polymer networks. Macromolecules, 2012, 45(12), 5307–15.

[10] Varshney, V.; Patnaik, S. S.; Roy, A. K.; Farmer, B. L. A molecular dynamics study of epoxy-based networks: Crosslinking procedure and prediction of molecular and material properties. Macromolecules, 2008, 41, 6837–42.

[11] Yu, S.; Yang, S.; Cho, M. Multi-scale modeling of crosslinked epoxy nanocomposites. Polymer, 2009, 50, 945–52.

[12] Kim, B.; Choi, J.; Yang, S.; Yu, S.; Cho, M. Multiscale modeling of interphase in crosslinked epoxy nanocomposites. Compos. Pt. B–Eng., 2017, 120, 128–42.

[13] Richeton, J.; Ahzi, S.; Vecchio, K. S.; Jiang, F. C.; Makradi, A. Modeling and validation of the large deformation inelastic response of amorphous polymers over a wide range of temperatures and strain rates. Int. J. Solids Struct., 2007, 44, 7938–54.

[14] Richeton, J.; Ahzi, S.; Daridon, L.; Rémond, Y. A formulation of the cooperative model for the yield stress of amorphous polymers for a wide range of strain rates and temperatures. Polymer, 2005, 46, 6035–43.

[15] Richeton, J.; Ahzi, S.; Vecchio, K. S.; Jiang, F. C.; Adharapurapu, R. R. Influence of temperature and strain rate on the mechanical behavior of three amorphous polymers: Characterization and modelling of the compressive yield stress. Int. J. Solids Struct, 2006, 43, 2318–35.

[16] Richeton, J.; Ahzi, S.; Daridon, L. Thermodynamic investigation of yield–stress models for amorphous polymers. Philos. Mag., 2007, 87(24), 3629–43.

[17] Gómez-del Río, T.; Rodríguez, J. Compression yielding of epoxy: Strain rate and temperature effect. Mater. Des., 2012, 35, 369–73.

[18] Bauwens-Crowet, C.; Bauwens, J. C.; Homès, G. Tensile yield-stress behavior of glassy polymers. J. Polym. Sci. A2, 1969, 7, 735–42.

[19] Bauwens-Crowet, C.; Bauwens, J. C.; Homès, G. The temperature dependence of yield of polycarbonate in uniaxial compression and tensile tests. J. Mater. Sci., 1972, 7, 176–83.

[20] Park, H.; Choi, J.; Kim, B.; Yang, S.; Shin, H.; Cho, M. Toward the constitutive modeling of high performance epoxy matrix: temperature-accelerated quasi-static molecular simulations consistent with the experimental test. Compos. Pt. B-Eng., 2018, 142, 131–41.

[21] Sundararaghavan, V.; Kumar, A. Molecular dynamics simulations of compressive yielding in cross-linked epoxies in the context of Argon theory. Int. J. Plast., 2013, 47, 111–25.

[22] Odegard, G. M.; Jensen, B. D.; Gowtham, S.; Wu, J.; He, J.; Zhang, Z. Predicting mechanical response of crosslinked epoxy using ReaxFF. Chem. Phys. Lett., 2014, 591, 175–8.

[23] Vu-Bac, N.; Bessa, M. A.; Rabczuk, T.; Liu, W. K. A multiscale model for the quasi-static thermo-plastic behavior of highly cross-linked glassy polymers. Macromolecules, 2015, 48(18), 6713–23.

[24] Park, H.; Kim, B.; Choi, J.; Cho, M. Influences of the molecular structures of curing agents on the inelastic-deformation mechanisms in highly-crosslinked epoxy polymers. Polymer, 2018, 136, 128–42.

[25] Jeyranpour, F.; Alahyarizadeh, Gh.; Arab, B. Comparative investigation of thermal and mechanical properties of crosslinked epoxy polymers with different curing agents by molecular dynamics simulation. J. Mol. Graph., 2015, 62, 157–64.

[26] Hossain, D.; Tschopp, M. A.; Ward, D. K.; Bouvard, J. L.; Wang, P., Horstemeyer, M. F. Molecular dynamics simulations of deformation mechanisms of amorphous polyethylene. Polymer, 2010, 51(25), 6071–83.

[27] Jatin; Sudarkodi, V.; Basu, S. Investigations into the origins of plastic flow and strain hardening in amorphous glassy polymers. Int. J. Plast., 2014, 56, 139–55.

[28] Baek, K.; Shin, H.; Yoo, T.; Cho, M. Two-step multiscale homogenization for mechanical behaviour of polymeric nanocomposites with nanoparticulate agglomerations. Compos. Sci. Technol., 2019, 179, 97–105.

[29] Shin, H.; Choi, J.; Cho, M. An efficient multiscale homogenization modeling approach to describe hyperelastic behavior of polymer nanocomposites. Compos. Sci. Technol., 2019, 175, 128–34.

[30] Masoumi, S.; Arab, B.; Valipour, H. A study of thermo-mechanical properties of the cross-linked epoxy: An atomistic simulation. Polymer, 2015, 70, 351-60.

[31] Li, C.; Strachan, A. Evolution of network topology of bifunctional epoxy thermosets during cure and its relationship to thermo-mechanical properties: A molecular dynamics study. Polymer, 2015, 75, 151-60.

[32] Shin, H.; Chang, S.; Yang, S.; Youn, B. D.; Cho, M. Statistical multiscale homogenization approach for analyzing polymer nanocomposites that include model inherent uncertainties of molecular dynamics simulations. Compos. Pt. B-Eng., 2016, 87, 120-31.

[33] Yang, S.; Yu, S.; Ryu, J.; Cho, J.-M.; Kyung, W.; Han, D.-S.; Cho, M. Nonlinear multiscale modeling approach to characterize elastoplastic behavior of CNT/polymer nanocomposites considering the interphase and interfacial imperfection. Int. J. Plast., 2013, 41, 124-46.

[34] Choi, J.; Shin, H.; Yang, S.; Cho, M. The influence of nanoparticle size on the mechanical properties of polymer nanocomposites and the associated interphase region: A multiscale approach. Compos. Struct., 2015, 119, 365-76.

[35] Yu, S.; Yang, S.; Cho, M. Analysis of thermal conductivity of polymeric nanocomposites under mechanical loading. J. Appl. Phys., 2013, 114, 213503.

[36] Ionita, M. Multiscale molecular modeling of SWCNTs/epoxy resin composites mechanical behavior. Compos. Pt. B–Eng, 2012, 43(8), 3491-6.

[37] Choi, J.; Yu, S.; Yang, S.; Cho, M. The glass transition and thermoelastic behavior of epoxy-based nanocomposites: A molecular dynamics study. Polymer, 2011, 52, 5197-203.

[38] Rahman, R.; Haque, A. Molecular modeling of crosslinked graphene–epoxy nanocomposites for characterization of elastic constants and interfacial properties. Compos. Pt. B–Eng., 2013, 54, 353-64.

[39] Krempl, E.; Khan, F. Rate(time)-dependent deformation behavior: an overview of some properties of metals and solid polymers. Int. J. Plast., 2003, 19, 1069-95.

[40] Capaldi F. M.; Boyce M. C.; Rutledge G. C. Molecular response of a glassy polymer to active deformation. Polymer, 2004, 45, 1391-9.

[41] Yagyu, H. Coarse-grained molecular dynamics simulation of the effects of strain rate on tensile stress of crosslinked rubber. Soft Mater., 2015, 13(4), 263-70.

[42] Eyring, H. Viscosity, plasticity, and diffusion as examples of absolute reaction rates. J. Chem. Phys., 1936, 4, 283–91.

[43] Robertson, R. E. Theory for the plasticity of glassy polymers. J. Chem. Phys., 1966, 44, 3950–6.

[44] Argon, A. S. A theory for the low-temperature plastic deformation of glassy polymers. Philos. Mag., 1973, 28(4), 839–65.

[45] Argon, A. S. Physical basis of distortional and dilational plastic flow in glassy polymers. J. Macromol. Sci. Part B–Phys., 1973, 8, 563–96.

[46] Williams, M. L.; Landel, R. F.; Ferry, J. D. The Temperature Dependence of Relaxation Mechanisms in Amorphous Polymers and Other Glass-forming Liquids. J. Am. Chem. Soc., 1955, 77(14), 3701–7.

[47] Ree, T.; Eyring, H. In: Eirich, F. R., editor. Rheology, vol 2. New York: Academic Press, 1958. [chapter 3].

[48] Fotheringham, D.; Cherry, B. W.; Bauwens-Crowet, C. Comment on "the compression yield behaviour of polymethyl methacrylate over a wide range of temperatures and strain-rates". J. Mater. Sci., 1976, 11, 1368–70.

[49] Fotheringham, D.; Cherry, B. W., The role of recovery forces in the deformation of linear polyethylene. J. Mater. Sci., 1978, 13, 951–64.

[50] von Mises, R. Mechanik der Festen Korper im plastisch deformablen Zustand. Nachr. Math Phys, 1913, 1, 582–92.

[51] Drucker, D. C. & Prager, W. Soil mechanics and plastic analysis for limit design Q. Appl. Math., 1952, 10, 157–65.

[52] Tschoegl, N. W. Failure surfaces in principal stress space. J. Polym. Sci. Pol. Sym., 1971, 32, 239–67.

[53] Ottosen, N. S. A failure criterion for concrete. J. Eng. Mech. Div.-ASCE, 1977, 103, 527–35.

[54] Deshpande, V. S.; Fleck, N. A. Isotropic constitutive models for metallic foams. J. Mech. Phys. Solids, 2000, 48, 1253–83.

[55] Hill, R. The essential structure of constitutive laws for metal composites and polycrystals. J. Mech. Phys. Solids, 1967, 15, 79–95.

[56] Melro, A. R.; Camanho, P. P.; Andrade Pires, F. M.; Pinho, S. T. Micromechanical analysis of polymer composites reinforced by unidirectional fibres: Part I – Constitutive modelling. Int. J. Solids Struct., 2013, 50, 1906–15.

[57] Melro, A. R.; Camanho, P. P.; Andrade Pires, F. M.; Pinho, S. T. Micromechanical analysis of polymer composites reinforced by unidirectional fibres: Part II – Micromechanical analyses. Int. J. Solids Struct., 2013, 50, 1897–905.

[58] Ghorbel, E. A viscoplastic constitutive model for polymeric materials. Int. J. Plast., 2008, 24, 2032–58.

[59] Horstemeyer, M. F.; Bammann, D. J. Historical review of internal state variable theory for inelasticity. Int. J. Plast., 2010, 26, 1310–34.

[60] De Borst, R.; Mühlhaus H. B. Gradient-dependent plasticity: Formulation and algorithmic aspects. Int. J. Numer. Methods Eng., 1992, 35, 521–39.

[61] Zepeda-Ruiz, L. A.; Stukowski, A.; Oppelstrup, T.; Bulatov, V. V. Probing the limits of metal plasticity with molecular dynamics simulations. Nature, 2017, 550, 492–5.

[62] Bulatov, V. V.; Hsiung, L. L.; Tang, M.; Arsenlis, A.; Bartelt, M. C.; Cai, W.; Florando, J. N.; Hiratani, M.; Rhee, M.; Hommes, G.; Pierce, T. G.; & de la Rubia, T. D. Dislocation multi-junctions and strain hardening. Nature, 2006, 440, 1174–8.

[63] Marian, J.; Cai, W.; & Bulatov, V. V. Dynamic transitions from smooth to rough to twinning in dislocation motion. Nat. Mater., 2004, 3, 158–63.

[64] Lund, A. C.; Schuh, C. A. Yield surface of a simulated metallic glass. Acta Mater., 2003, 51, 5399–411.

[65] Schuh, C. A.; Lund, A. C. Atomistic basis for the plastic yield criterion of metallic glass. Nat. Mater., 2003, 2, 449–52.

[66] Rodney, D.; Schuh, C. Distribution of Thermally Activated Plastic Events in a Flowing Glass. Phys. Rev. Lett., 2009, 102, 2335503.

[67] Rottler, J.; Robbins, M. O. Yield conditions for deformation of amorphous polymer glasses. Phys. Rev. E, 2001, 64, 051801.

[68] Versino, D.; Tonda, A.; Bronkhorst, C. A. Data driven modeling of plastic deformation. Comput. Meth. Appl. Mech. Eng., 2017, 318, 981–1004.

[69] Kirchdoerfer, T.; Ortiz, M. Data–driven computational mechanics. Comput. Meth. Appl. Mech. Eng., 2016, 304, 81–101.

[70] Liu, Z.; Wu, C. T.; Koishi, M. A deep material network for multiscale topology learning and accelerated nonlinear modeling of heterogeneous materials. Comput. Meth. Appl. Mech. Eng., 2019, 345, 1138–68.

[71] Yang, S.; Qu J. Computing thermomechanical properties of crosslinked epoxy by molecular dynamics simulations. Polymer, 2012, 53, 4806–17.

[72] Fan, H. B.; Yuen, M. M. F. Material properties of the crosslinked epoxy resin compound predicted by molecular dynamics simulation. Polymer, 2007, 48(7),2174–8.

[73] Heine, D. R.; Grest, G. S.; Lorenz, C. D.; Tsige, M.; Stevens, M. J. Atomistic simulations of end-linked poly(dimethylsiloxane) networks: Structure and relaxation. Macromolecules 2004, 37(10), 3857-64.

[74] Guest, N. T.; Tilbrook, D. A.; Ogin, S. L.; Smith, P. A. Characterization and modeling of diglycidyl ether of bisphenol-a epoxy cured with aliphatic liquid amines. J. Appl. Polym. Sci., 2013, 130, 3130–41.

[75] Tsai, J.–L.; Hsiao, H.; Cheng, Y.–L. Investigating Mechanical Behaviors of Silica Nanoparticle Reinforced Composites. J. Compos. Mater. 2010, 44, 505–24.

[76] Hughes, E. J.; Rutherford, J. L. Determination of mechanical properties of polymer film materials. Technical Report NASA-CR-147115 1975, NASA.

[77] Botto, P. A.; Duckett, R.A.; Ward, I. M. The yield and thermoelastic properties of oriented poly(methyl methacrylate). Polymer, 1987, 28, 257–62.

[78] Mayr, A. E.; Cook, W. D.; Edward, G. H. Yielding behaviour in model epoxy thermosets—I. Effect of strain rate and composition. Polymer, 1998, 39, 3719–24.

[79] Brooks, N. W.; Unwin, A. P.; Duckett, R. A.; Ward, I. M. Temperature and strain rate dependence of yield strain and deformation behavior in polyethylene. J. Polym. Sci. Pol. Phys., 1997, 35, 545–52.

[80] Garcia, F. G.; Soares, B. G.; Pita, V. J. R. R.; Sanchez, R.; Rieumont, J. Mechanical properties of epoxy networks based on DGEBA and aliphatic amines. J. Appl. Polym., 2007, 106(3), 2047–55.

[81] Qi, B.; Zhang, Q. X.; Bannister, M.; Mai Y.-W. Investigation of the mechanical properties of DGEBA-based epoxy resin with nanoclay additives. Compos Struct 2006, 75, 514–9.

[82] Jilani, W.; Mzabi, N.; Fourati, N.; Zerrouki, C.; Gallot-Lavallée, O.; Zerrouki, R.; Guermazi, H. Effects of curing agent on conductivity, structural and dielectric properties of an epoxy polymer. Polymer, 2015, 79, 73–81.

[83] Voter, A. F. Hyperdynamics: accelerated molecular dynamics of infrequent events. Phy. Rev. Lett., 1997, 78(20), 3908.

[84] So/rensen, M. R.; Voter, A. F. Temperature-accelerated dynamics for simulation of infrequent events. J. Chem. Phys., 2000, 112(21), 9599.

[85] Voter, A. F. Parallel replica method for dynamics of infrequent events. Phy. Rev. B, 1998, 57(22), 985–8.

[86] Pethrick, R. A.; Hollins, E. A.; McEwan, I.; MacKinnon, A. J.; Hayward, D.; Cannon, L. A. Dielectric, mechanical and structural, and water absorption properties of a thermoplastic-modified epoxy resin: Poly(ether sulfone)-amine cured epoxy resin. Macromolecules, 1996, 29, 5208–14.

[87] Nazarychev, V. M.; Lyulin, A. V.; Larin, S. V.; Gurtovenko, A. A.; Kenny, J. M.; Lyulin, S. V. Molecular dynamics simulations of uniaxial deformation of thermoplastic polyimides. Soft matter, 2016, 12, 3972–81.

[88] G`Sell, C.; Jonas, J. J. Yield and transient effects during the plastic deformation of solid polymers. J. Mater. Sci., 1981, 16, 1956-74.

[89] Wendlandt, M.; Tervoort, T. A.; Suter, U. W. Non-linear, rate-dependent strain-hardening behavior of polymer glasses. Polymer, 2005, 46(25), 11786-97.

[90] Hope, P. S.; Ward, I. M.; Gibson, A. G. The hydrostatic extrusion of polymethylmethacrylate. J. Mater. Sci. 1980, 15, 2207-20.

[91] Gonzalez-Dominguez, J. M.; Anson-Casaos, A.; Diez-Pascual, A. M.; Ashrafi, B.; Naffakh, M.; Backman, D.; Stadler, H.; Johnston, A.; Gomez, M.; Martinez, M. T. Solvent-free preparation of high-toughness epoxy-SWNT composite materials. ACS Appl. Mater. Interfaces, 2011, 3, 1441-50.

[92] Gonzalez-Dominguez, J. M.; Diez-Pascual, A. M.; Anson-Casaos, A.; Gomez-Fatou, M. A.; Martinez, M. T. Epoxy composites with covalently anchored amino-functionalized SWNTs: towards the tailoring of physical properties through targeted functionalization. J. Mater. Chem., 2011, 21, 14947-58.

[93] Stachurski, Z. H. Deformation mechanisms and yield strength in amorphous polymers. Prog. Polym. Sci., 1997, 22, 407-74.

[94] Enns, J. B.; Gillham, J. K. Effect of the extent of cure on the modulus, glass transition, water absorptio, and density of an amine-cured epoxy. J. Appl. Polym. Sci., 1983, 28, 2831–46.

[95] Pascault, J. P.; Williams, R. J. J. Glass transition temperature versus conversion relationships for thermosetting polymers. J. Polym. Sci. Pol. Phys., 1990, 28, 85–95.

[96] van der Meer, F. P. Micromechanical validation of a mesomodel for plasticity in composites. Eur. J. Mech. A-Solids, 2016, 60, 58–69.

[97] Courant, R. Variational methods for the solution of problems of equilibrium and vibrations. Bull. Am. Math. Soc., 1943, 49, 1–23.

[98] Coello Coello, C. A. Theoretical and numerical constraint-handling techniques used with evolutionary algorithms: a survey of the state of the art. Comput. Meth. Appl. Mech. Eng., 2002, 191, 1245-87.

[99] Searson, D. P. GPTIPS 2: an open-source software platform for symbolic data mining. Chapter 22 in Handbook of Genetic Programming Applications, A.H. Gandomi et al., (Eds.), Springer, New York, NY, 2015.

[100] Haba, D.; Brunner, A. J.; Barbezat, M.; Spetter, D.; Tremel, W.; Pinter, G. Correlation of epoxy material properties with the toughening effect of fullerene-like WS2 nanoparticles. Eur. Polym. J., 2016, 84, 125–36.

[101] Barlat, F.; Brem, J. C.; Yoon, J. W.; Chung, K.; Dick, R. E.; Lege, D. J.; Pourboghrat, F.; Choi, S.–H.; Chu, E. Plane stress yield function for aluminum alloy sheets—part 1: theory. Int. J. of Plast., 2003, 19, 1297–319.

[102] Yoon, J. W.; Barlat, F.; Chung, K.; Pourboghrat, F.; Yang, D. Y. Earing predictions based on asymmetric nonquadratic yield function. Int. J. of Plast., 2000, 16, 1075–104.

[103] Yao, H.; Cao, J. Prediction of forming limit curves using an anisotropic yield function with prestrain induced backstress. Int. J. of Plast., 2002, 18, 1013–38.

[104] Park, H.; Cho, M. A multiscale framework for the elasto-plastic constitutive equations of crosslinked epoxy polymers considering the effects of temperature, strain rate, hydrostatic pressure, and crosslinking density. Manuscript in preparation, 2019.

[105] Neto, E. d. S., Peric´, D., Owen, D. Computational Methods for Plasticity: Theory and Applications. John Wiley & Sons Ltd, 2008.

[106] Simo, J.; Hughes, T. Computational Inelasticity, vol. 7 of Interdisciplinary Applied Mathematics. Springer-Verlag, Berlin, 1998.

[107] Bigoni, D.; Piccolroaz, A. Yield criteria for quasibrittle and frictional materials. Int. J. Solids Struct., 2004, 41, 2855–78.

국문 요약

본 논문에서는 고분자 기반 소재의 탄성 및 소성 변형에 대한 미시적 변형 메커니즘의 정성적 규명과, 정량적 모사를 위한 머신 러닝 기반의 멀티 스케일 해석 방법론을 제시한다. 제안된 해석 방법론은 미시적 소성 변형 거동에 대한 분자 수준에서의 일반적인 메커니즘 규명과, 고분자 소재의 비선형 기계적 거동에 대해 실험의 도움 없이 정량적 예측을 가능케 하며, 도출된 다수의 데이터를 기반으로 학습된 구성 방정식 모델링을 통해 거시적 구조물의 비선형 거동을 예측한다. 특히, 제안된 멀티스케일 해석 방법론은 다양한 고분자 소재 자체의 고유한 구조–물성간의 관계를 고려한 구성방정식의 모델링을 가능케 하며, 이는 기존의 범용적 소성 거동에 대한 모델링에서 소재의 변형 특성에 일대일 맞춤화된 해석 모델로의 확장이라는 점에 그 의의가 있다.

원자 및 분자 스케일에서의 미시 구조의 동적 모사가 가능한 분자동역학 전산해석을 활용하여, 열경화성 소재의 한 종류인 에폭시 소재의 미시적 변형 메커니즘을 규명하였다. 특히, 가교제의 분자 구조 특성이 경화된 에폭시 소재의 거시적 소성 변형에 미치는 영향을 이해하기 위하여, 분자동역학 모델에 압축 변형을 가한 후 하중을 제거하는 동안 에너지, 응력, 구조적 변화를 관찰하였으며, 그 결과, 소성 변형 영역에서 방향족 가교제의 벤젠 고리 주변의 비가역적 접힘 현상의 거시적 소성 변형률에 대한 기여를 규명하였다. 이러한 벤젠고리 근처 비가역적 접힘 거동은 반복 하중 하에서 점진적으로 축적

되며, 지방족 가교제 기반 에폭시 소재의 거시적 스케일에서의 소성 변형률 진전보다 더욱 빠른 진전을 야기함을 밝혀내었다.

분자동역학 전산해석은 원자의 거동을 모사하기 위하여 매우 짧은 펨토 초 (fs) 단위의 타임 스텝을 사용하기 때문에, 실험적 시간 스케일의 분자 거동을 모사하는데 제한이 있다. 이로 인하여, 분자동역학 전산해석과 실험간의 기계적 거동 예측 측면에서 정량적 괴리가 발생하게 되는데, 이를 고려하기 위하여 본 연구에서는 분자 동역학 전산해석을 이용하여 준정적 상태의 응력–변형률 선도를 예측하는 두가지 방법론을 제시하였다. 첫번째 방법론은 고분자 소재의 항복 응력의 평가에 대한 시간과 온도의 동일성을 이용하여 항복 응력에 대한 마스터 선도를 순차적으로 구축하여 준정적 상태에서의 항복 응력을 예측한다. 두번째 방법론은 고분자 소재의 고전적 항복 이론을 이용하여 기계적 물성을 통해 준정적 상태에서의 항복 응력을 예측한다. 변형 속도와 온도에 대한 항복 응력의 비선형 특성을 반영하기 위하여 첫번째 방법론에서는 기준 온도 보다 높은 온도 하에서의 고분자 사슬의 운동 특성을 준정적 상태의 항복 거동 예측에 이용하였으며, 두번째 방법론에서는 Cooperative 모델과 내부 응력을 도입하여 준정적 항복 응력을 예측하는 마스터 선도를 구축하였다. 이후 완성된 방법론을 통하여 다양한 온도, 압력 및 재료의 미시 구조 특성을 반영하여 준정적 상태의 응력–변형률 선도를 도출하였다.

본 연구에서는 분자동역학 전산해석을 통해 예측된 준정적 상태의 기

계적 물성 및 응력–변형률 선도를 토대로, 다양한 온도, 압력 등 물리적 상황과 고분자 소재의 미시구조 특성을 반영하여 다양한 조합 하중 하의 거시적 구조물의 소성 변형을 모사하기 위한 구성방정식을 모델링을 하였다. 에폭시의 구조 특성을 반영하기 위해 다양한 가교율 하에서 도출된 준정적 상태의 물성 및 응력–변형률 선도를 도출하였고, 3차원 홀 구조물의 소성 변형을 모사하기 위한 유한요소해석을 수행하였다. 그 결과, 가교율에 따라 홀 주변부의 소성 변형률의 진전 속도가 상이함을 확인하였다.

특히, 본 연구에서는 조합 하중에 따른 거시적 소성 변형을 모사하기 위해 기존의 고전적 항복 함수의 도입 대신, 3차원 응력 공간에서의 고려된 고분자 소재의 항복 표면의 최초 형상 및 변형이 진행됨에 따라 나타나는 항복 표면의 진전을 정밀하게 모사하기 위한 항복 함수를 머신 러닝 학습을 통하여 도출하는 방법론을 개발하였다. 이를 위해, 다양한 하중 방향에서의 에폭시 소재의 항복 데이터를 분자동역학 해석을 통해 도출하였으며, 변형 속도의 영향을 고려하기 위해 준정적 상태의 항복 표면을 예측하기 위한 방법론을 개발하였다. 도출된 항복 데이터를 기반으로 항복 함수의 수학적 표현을 도출하기 위하여 머신 러닝 학습 방법의 일종인 유전 알고리즘 (Genetic algorithm) 을 도입하였으며, 항복 함수의 필수적 특성을 학습에 반영시키기 위한 제한 조건을 부과하였다. 학습을 통해 도출된 데이터 기반 항복 함수를 통해 소성 변형 모사를 위한 구성방정식을 정식화 하였으며, 이의 성능을 유한요소해석을 통해 기존의 고전적 항복 함수와 비교 검증하였다.

본 연구에서 제시된 고분자 소재의 소성 변형 전산 해석을 위한 머신 러닝 기반 멀티스케일 해석 방법론은 분자 스케일 수준의 소성 변형 메커니즘의 규명과 더불어, 소재 고유의 다축 변형 항복 특성에 기인한 구성방정식의 모델링을 통해 거시적 기계 거동을 실험 없이 정밀하게 예측할 수 있다. 이는 기존의 물리적, 수학적 고찰을 통해 고안될 수 밖에 없던 소성 모델링을 재료 자체의 고유한 변형 특성에 초점을 맞춘 모델링으로의 확장이 가능함을 의미하며, 제안된 방법론의 다양한 소재에 대한 적용을 통해 라이브러리화 할 수 있음을 의미한다. 따라서 제안된 해석 방법론은 단일 고분자 소재뿐만 아니라 고분자 소재 기반 다양한 복합재의 기계적 거동에 대한 예측 요구되는 모든 산업에서 전방위적으로 사용될 것으로 기대된다.

주요어: 데이터 기반 역학, 머신 러닝, 소성 변형, 멀티스케일 해석, 비선형 유한요소해석, 고분자 소재

학번: 2014-21563